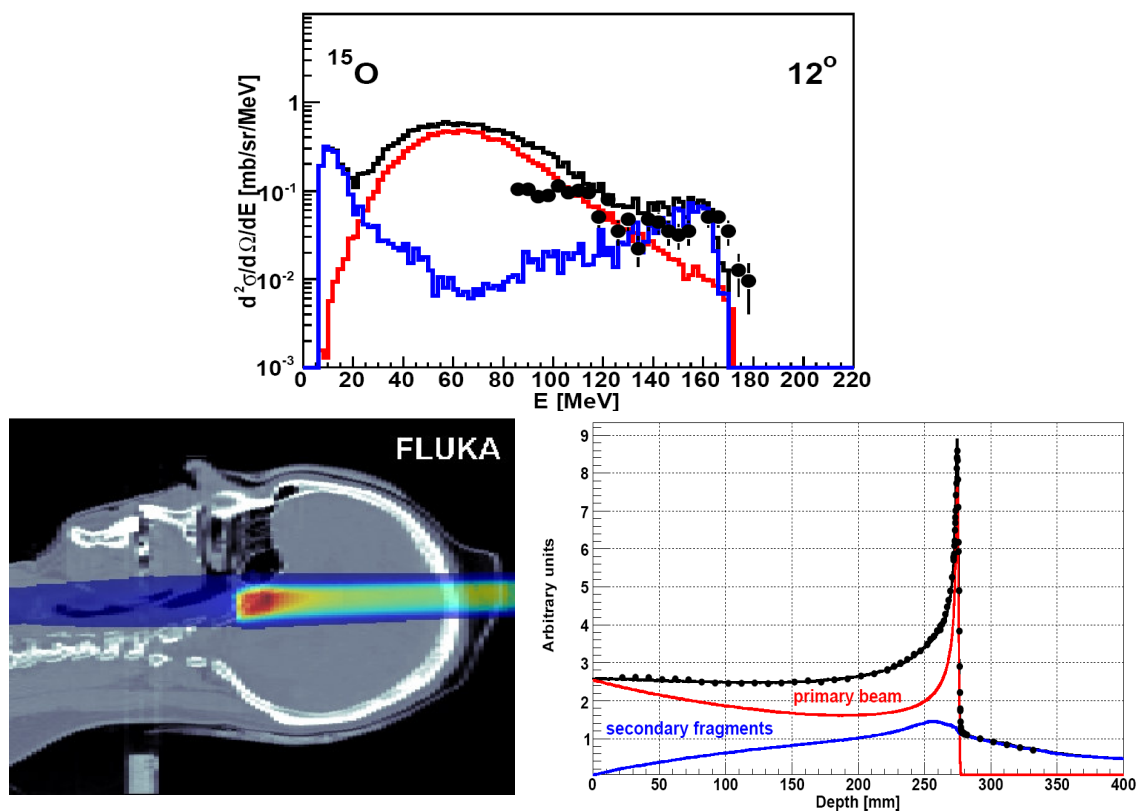


# Nucleus-Nucleus Interaction Modelling and Applications in Ion Therapy Treatment Planning

*Andrea Mairani*



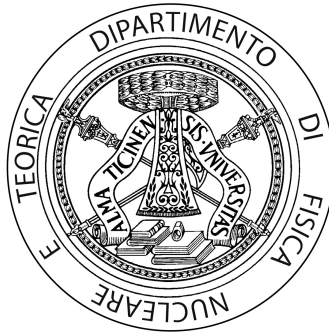
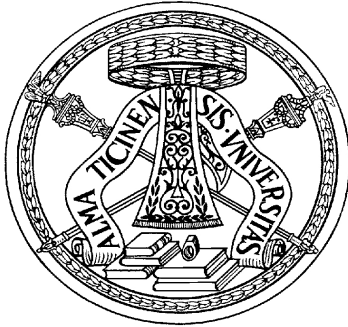
**Tesi per il conseguimento del titolo**



Università degli  
Studi di Pavia

Dipartimento di Fisica  
Nucleare e Teorica

Istituto Nazionale di  
Fisica Nucleare



DOTTORATO DI RICERCA IN FISICA – XX CICLO

# **Nucleus-Nucleus Interaction Modelling and Applications in Ion Therapy Treatment Planning**

dissertation submitted by

***Andrea Mairani***

to obtain the degree of

**DOTTORE DI RICERCA IN FISICA**

**Supervisors: Prof. A. Ottolenghi (Università di Pavia)**

**Prof. E. Gadioli (Università di Milano)**

**Referee: Dr. M. B. Chadwick (LANL)**

## Cover

- Top:* Double differential spectrum of  $^{15}\text{O}$  emitted in the 16.5 MeV/n  $^{12}\text{C} + ^{12}\text{C}$  reaction at  $12^\circ$ . More details can be found in Fig 2.13 of this thesis, on page 36.
- Bottom, left:* Monte Carlo CT-based calculation of dose for a cranial plan. More details can be found in Fig. 4.12 of this thesis, on page 77.
- Bottom, right:* Bragg Curve of a 400 MeV/n carbon beam on water. More details can be found in Fig. 3.2 of this thesis, on page 48.

Nucleus-Nucleus Interaction Modelling and Applications in Ion Therapy  
Treatment Planning

*Andrea Mairani*

PhD thesis – University of Pavia

Printed in Pavia, Italy, November 2007

ISBN 978-88-95767-09-3





*To my parents for their love and support  
To Enrica, the most fascinating ‘discover’ of my Ph.D.*





# Contents

<b>Introduction</b>	<b>1</b>
<b>1 A brief introduction to hadron therapy</b>	<b>5</b>
1.1 The physical basis of ion beam therapy . . . . .	7
1.2 The biological basis of ion beam therapy . . . . .	15
<b>2 Low energy light ion interaction</b>	<b>21</b>
2.1 Introduction . . . . .	21
2.2 Experiment . . . . .	22
2.3 Outline of the theory . . . . .	25
2.4 Comparison of experimental and theoretical spectra . . . . .	33
<b>3 Investigation of carbon ion fragmentation in water using the FLUKA code</b>	<b>43</b>
3.1 Introduction . . . . .	43
3.2 FLUKA code capabilities . . . . .	44
3.3 Characterization of the primary beams . . . . .	46
3.4 Characterization of charged fragments . . . . .	51
3.4.1 Angular distributions . . . . .	52
3.4.2 Build-up of charged fragments . . . . .	55
3.4.3 Energy spectra . . . . .	56
<b>4 Clinical CT-based calculations of dose in carbon ion therapy using the FLUKA code</b>	<b>61</b>
4.1 Introduction . . . . .	61
4.2 Analytical treatment planning for ion therapy: TRiP . . . . .	62
4.3 Monte Carlo calculations of dose in carbon ion therapy . . . . .	67
4.3.1 The GSI beam delivery system . . . . .	67
4.3.2 CT handling . . . . .	70
4.3.3 CT-based calculations of dose . . . . .	75

<b>5</b>	<b>The Local Effect Model and its interface with FLUKA</b>	<b>81</b>
5.1	Introduction . . . . .	81
5.2	The Local Effect Model . . . . .	82
5.3	The radiobiology in Treatment Planning: TRiP rapid calculation	86
5.4	Mixed radiation fields . . . . .	88
5.5	Results and discussion . . . . .	91
	<b>Conclusions and perspectives</b>	<b>97</b>
	<b>Bibliography</b>	<b>99</b>
	<b>List of publications</b>	<b>107</b>
	<b>Acknowledgments</b>	<b>111</b>

# List of Figures

1.1	Dose depth profiles of photons from different radiation sources and carbon ions in water [24]. . . . .	6
1.2	A pictorial view of one-dimensional spread-out Bragg peak. . . .	8
1.3	Electronic stopping power of different ions of therapeutic interest calculated in water as a function of the energy [41,42]. . . .	10
1.4	Dose depth profile in water calculated by means of the FLUKA code for carbon ions at increasing energies. . . . .	11
1.5	Calculated lateral deflection in water of several ion beams of therapeutic relevance [42,48]. . . . .	12
1.6	Measured $\beta^+$ -activity in comparison with the calculated dose distribution for a 212 MeV/n carbon ion beam stopped in a PMMA phantom [53,54] . . . . .	15
1.7	Principle of the RBE definition [5]. . . . .	17
1.8	Local dose distributions of X-rays and carbon ions at different specific energies [5]. . . . .	17
1.9	RBE $_{\alpha}$ values for CHO-K1 cells and their repair deficient mutant xrs-5 for different LET values and plotted as function of residual range in water [5,59]. . . . .	18
1.10	Survival curves for CHO-K1 cells after irradiation with ions of different atomic number and LET values of approximately 100 keV/ $\mu$ m [5]. . . . .	18
1.11	OER for neon, carbon and helium. OER and energy data from [65], residual range calculated with ATIMA [41]. . . . .	19
2.1	Particle identification spectrum of the silicon detector telescope obtained at an emission angle of 8°. . . . .	23
2.2	Laboratory double differential cross sections of different isotopes of C, N and O emitted at 8° in the bombardment of $^{12}\text{C}$ with 200 MeV $^{12}\text{C}$ ions. . . . .	24
2.3	Reaction cross section for $^{12}\text{C}+^{12}\text{C}$ [89]. . . . .	28
2.4	Differential reaction cross section for $^{12}\text{C}+^{12}\text{C}$ at 200 MeV total kinetic energy. . . . .	28

2.5	Theoretical prediction of the average total multiplicity of pre-equilibrium ejectiles in the complete fusion of two $^{12}\text{C}$ ions as a function of the incident energy. . . . .	31
2.6	Theoretical prediction of the relative multiplicities of a few pre-equilibrium particles emitted in the complete fusion of two $^{12}\text{C}$ ions, as a function of the incident energy. . . . .	32
2.7	Pictorial view of the proton theoretical CUMULATIVE angular distributions in the CM frame. . . . .	32
2.8	Theoretical prediction of double differential spectra (in the CM frame) of protons emitted during the thermalization of the non-equilibrated system formed by the $^{12}\text{C}+^{12}\text{C}$ complete fusion at 30 MeV/n. . . . .	33
2.9	Double differential spectra of $^{19}\text{F}$ and $^{20}\text{F}$ in the $^{12}\text{C}+^{12}\text{C}$ system at $E_{\text{LAB}}=200$ MeV. . . . .	34
2.10	Double differential spectra of $^{18}\text{O}$ in the $^{12}\text{C}+^{12}\text{C}$ system at $E_{\text{LAB}}=200$ MeV. . . . .	34
2.11	Double differential spectra of $^{17}\text{O}$ in the $^{12}\text{C}+^{12}\text{C}$ system at $E_{\text{LAB}}=200$ MeV. . . . .	35
2.12	Double differential spectra of $^{16}\text{O}$ in the $^{12}\text{C}+^{12}\text{C}$ system at $E_{\text{LAB}}=200$ MeV. . . . .	35
2.13	Double differential spectra of $^{15}\text{O}$ in the $^{12}\text{C}+^{12}\text{C}$ system at $E_{\text{LAB}}=200$ MeV. . . . .	36
2.14	Double differential spectra of $^{14}\text{O}$ in the $^{12}\text{C}+^{12}\text{C}$ system at $E_{\text{LAB}}=200$ MeV. . . . .	37
2.15	Double differential spectra of $^{15}\text{N}$ in the $^{12}\text{C}+^{12}\text{C}$ system at $E_{\text{LAB}}=200$ MeV. . . . .	37
2.16	Double differential spectra of $^{13}\text{N}$ in the $^{12}\text{C}+^{12}\text{C}$ system at $E_{\text{LAB}}=200$ MeV. . . . .	38
2.17	Double differential spectrum of O emitted at $15^\circ$ in the $^{12}\text{C}+^{12}\text{C}$ system. . . . .	38
2.18	Double differential spectra of $^{11}\text{C}$ in the $^{12}\text{C}+^{12}\text{C}$ system at $E_{\text{LAB}}=200$ MeV. . . . .	39
2.19	Double differential spectra of $^{11}\text{B}$ in the $^{12}\text{C}+^{12}\text{C}$ system at $E_{\text{LAB}}=200$ MeV. . . . .	40
2.20	Double differential spectra of $^{10}\text{B}$ in the $^{12}\text{C}+^{12}\text{C}$ system at $E_{\text{LAB}}=200$ MeV. . . . .	40
3.1	Sketch of the experimental setup for the beam attenuation experiment [18]. . . . .	47
3.2	Bragg curve for a 400 MeV/n carbon beam on water. . . . .	48
3.3	Close-up of the peak shown in Figure 3.2 . . . . .	48
3.4	Simulated contributions of the indicated secondary particles to the Bragg curve shown in Figure 3.2. . . . .	49
3.5	Calculated attenuation of a 400 MeV/n $^{12}\text{C}$ beam together the build-up of secondary carbon ions as a function of depth in water. . . . .	50

## LIST OF FIGURES

---

3.6	Experimental and simulated attenuation profile of a 400 MeV/n $^{12}\text{C}$ beam as a function of depth in water. . . . .	50
3.7	Sketch of the experimental setup used for the angular/energy distribution measurements [18]. . . . .	51
3.8	Particle identification spectrum obtained at an emission angle of $2^\circ$ . The data originate from a 400 MeV/n $^{12}\text{C}$ beam fully stopped in a 28.8 cm thick water target [18]. . . . .	52
3.9	Angular distributions of carbon ions behind thick water phantoms. . . . .	53
3.10	Angular distributions of secondary fragments behind a 15.9 cm thick water phantom. . . . .	53
3.11	Angular distributions of secondary fragments behind a 31.2 cm thick water phantom. . . . .	54
3.12	Build-up curves of secondary charged fragments. . . . .	55
3.13	Energy spectra of H fragments behind a 31.2 cm thick water phantom. . . . .	58
3.14	Energy spectra of He fragments behind a 28.8 cm thick water phantom. . . . .	58
3.15	Energy spectra of Li fragments behind a 28.8 cm thick water phantom. . . . .	59
3.16	Energy spectra of B fragments behind a 28.8 cm thick water phantom. . . . .	59
4.1	Energy spectrum and its cumulative distribution, as a function of kinetic energy, for $^4\text{He}$ particles produced by a 400 MeV/n carbon beam at about 29 cm in water. . . . .	64
4.2	Build-up of He fragments and attenuation of the carbon beam as a function of depth in water. . . . .	65
4.3	Patient CT and table systems [122]. . . . .	68
4.4	Spread-out Bragg peak in water. . . . .	69
4.5	Lateral profiles of the spread-out Bragg peak of Figure 4.4. . . . .	70
4.6	Transformation from CT into water equivalent system [7]. . . . .	71
4.7	Correlation between CT Hounsfield numbers and water-equivalent path lengths [125]. . . . .	72
4.8	Comparison between TRiP and FLUKA 270 MeV/n pristine Bragg peaks calculated in phantoms corresponding to different CT numbers. . . . .	74
4.9	Conversion of CT numbers into mass density. . . . .	74
4.10	A screen-shot of the developed ROOT based software used to visualize and to analyze CT images. . . . .	75
4.11	MC calculated dose deposition against the planned treatment in a transversal view of a cranial plan. . . . .	76
4.12	MC calculated dose deposition against the planned treatment in different views along the beam axis . . . . .	77
4.13	Comparison between MC and TRiP calculated depth-dose deposition. . . . .	78

---

4.14	Comparison between MC and TRiP lateral dose distribution. . .	79
5.1	Local dose distributions of X-rays and carbon ions at different specific energies [5]. . . . .	84
5.2	Schematic representation of the Local Effect Model [137]. . . . .	85
5.3	<i>Initial</i> RBE as a function of the particle kinetic energy for a Chordoma cell line. . . . .	86
5.4	Physical dose and linear-quadratic model parameters obtained with the FLUKA-LEM calculations as a function of depth in water for CHO cells, after irradiation with 187 MeV/n carbon ions. . . . .	90
5.5	Clonogenic survival of CHO cells after irradiation with 187 MeV/n carbon ions, as a function of depth in water [3]. . . . .	92
5.6	Simulated and experimental clonogenic survivals of CHO cells after irradiation with 270 MeV/n carbon ions, as a function of particle fluences, at various depths in water [3]. . . . .	93
5.7	Simulated clonogenic survival of CHO cells after irradiation with 270 MeV/n carbon ions, as a function of particle fluences, at various depths in water. . . . .	93
5.8	Clonogenic survival, biological dose and RBE for a Chordoma cell line as a function of depth in water after the irradiation with 219.8 MeV/n carbon ions. . . . .	94
5.9	RBE and biological dose for a Chordoma cell line as a function of depth in water for different carbon fluences . . . . .	95

# List of Tables

2.1	Energy integrated cross sections in (mb/sr) of the continuum as well as the discrete regions of the C-isotopes measured at laboratory angles of $8^\circ$ and $20^\circ$ in the bombardment of $^{12}\text{C}$ with 200 MeV $^{12}\text{C}$ ions. . . . .	25
2.2	Break-up cross sections and relative angular momenta for the different fragmentation modes considered in the calculation. . .	30
5.1	Parameters of the LEM model for the dose response of two cell lines [8, 145]. . . . .	91





# Introduction

The possibility of using hadron therapy (with protons or heavier ions) in every day clinical practice in cancer therapy, as a consequence of the worldwide fast growing of new proposals and facilities [1], requires an improvement of treatment-dedicated software including the development of new approaches able to provide a more accurate simulation of the interaction of radiation with biological tissue. The treatment planning system (TPS) is a complex computer software that helps to design radiation treatments and to compute the absorbed dose and/or the biological effective dose delivered to the patient.

One of the main objectives in radiotherapy is the conformal delivery of the prescribed dose to the target volume, while sparing as much as possible the surrounding healthy tissue and critical structures. In the intensity modulated particle therapy (IMPT), many thousands of narrow beams, individually weighted, are delivered to the patient along different directions in order to provide a uniform dose to an arbitrary shaped planned target volume (PTV). Computer aided *inverse planning* techniques are mandatory to create treatment plans. In IMPT, that means that beam spot positions and beam energies and intensities are determined from the prescribed dose distribution by means of an optimization procedure based on an appropriate objective function.

The most important difference between protons and heavier ions, is the increased biological effectiveness of the latter [2–5], i.e., a lower physical dose is needed with ions to obtain a given biological effect. For carbon ions, which are considered the optimal choice [6], the effect of the favourable absorbed dose distribution, very localized, is enhanced by the large relative biological effectiveness (RBE) towards the end of the particle range, offering an additional advantage for slow growing radioresistant tumors.

In this work, the analytical code TRiP (TReatment planning for Particles, 1998), i.e., the production version of the treatment planning used in clinical practice at GSI [7–9], is taken as the reference TPS. It will be also the TPS of new European facilities, HIT (Heidelberg, Germany) and CNAO (Pavia, Italy). This treatment planning system is an analytical code based on fast performing pencil-beam algorithms. Monte Carlo (MC) statistical method for dose calculation could represent, on the other hand, the most effective tool for the

verification, and eventually the correction, of analytical TPS. It could allow, in fact, the dose evaluation for every real situation and in all the cases for which experimental verification is impossible and/or the analytical approach is not sufficiently precise. Nevertheless, the limiting precision of a MC calculation, as the analytical ones, is related to the knowledge of the physical processes ruling the studied interactions, especially the nuclear ones. Giving this caveat, the MC simulations could be important tools for the development, validation, and monitoring of treatment planning. The main items where these techniques are more effective with respect to the traditional analytical methods can be summarized as follows:

- MC methods take into account the real composition of human body, with a clear advantage over the water-equivalent approach [10–13];
- MC methods naturally include mixed field description and three-dimensional spread of the particle fluence;
- in-beam monitoring of the irradiation plan through positron emission tomography can be accurately performed using MC simulations fully taking into account the complexity of mixed radiation field [14].

The required features of a MC code to be used for verification/improvement of analytical TPSs (inverse planning techniques are out of the scope of this work) are: (i) precise and reliable physical models for transport and interaction of all components of the expected radiation field, namely ions, hadrons, and the electromagnetic particles; (ii) the capability to import the irradiation *geometry* from CT scans and to carefully reproduce density and composition of the irradiated areas; (iii) the coupling to a radiobiological model for the evaluation of cell damage.

This work represents a contribution towards the aim of making available a MC validation tool for heavy ion treatment planning by the widely used transport and interaction code FLUKA [15, 16]. In fact, after a brief introduction to hadron therapy in Chapter 1, Chapter 2 presents the new BME event generator together with its first experimental validation. Through this model nucleus-nucleus reactions at energies ranging from the Coulomb barrier up to 100 MeV/n can now be described extending the FLUKA energy range of heavy ion interactions. Furthermore, the RQMD event generator [17] covering the intermediate energy interval (from 100 MeV/n up to 5 GeV/n), has been benchmarked against the mixed field measured at GSI for a 400 MeV/n carbon beam on water phantoms [18, 19] (Chapter 3). In addition, on the basis of the results discussed in [12, 13] it is now possible to import CT images in TRiP format, convert them into the FLUKA *geometry*, and perform CT-based calculations of the absorbed dose (comparisons with the reference software TRiP can be found in Chapter 4). Finally, the radiobiological model LEM (Local Effect Model) developed at GSI by M. Scholz *et al.* [2–4, 8] has been interfaced with the FLUKA code in order to perform biological effective dose calculations

(benchmark of the ‘FLUKA-LEM’ interface is given in Chapter 5). This latter has been carried out in common with M. Scholz, M. Krämer (GSI) and A. Ottolenghi (University of Pavia).



# Chapter 1

## A brief introduction to hadron therapy

After heart diseases, cancer is the second most frequent cause of disease in developed countries; every year, more than 1 million people in the European Union are diagnosed having cancer, 58% of them at the stage of a localised primary tumor. Surgery is the most efficient way to remove malignant tissue. However radiation alone and in combination with surgery improves the recovery rate to about 40%. For a generalized disease, where the cancer has spread over a larger part of the body, a final cure is much less likely. Current local or local-regional tumor treatments still fail for 18% of all patients. Since surgery is commonly considered to have reached the limits of its potential for cancer curing, there is a strong clinical demand for improving radiotherapy techniques [20–22].

In principle, any tissue can be destroyed by the radiation if only the applied dose is high enough. In practice, radiation therapy is limited by the radiation tolerance of the normal tissue surrounding the tumor. Consequently, the conformal delivery of the prescribed dose to the target volume, sparing as much as possible the surrounding healthy tissue and critical organs, is the key to have more chances of success in the treatment [23].

In conventional radiotherapy, dose delivery is limited by the physical parameters of the depth dose distribution and the scattering of the beam when penetrating a thick layer like the human body. Traditional sources like X-ray tubes (energy  $\leq 200$  keV) or radioactive isotopes e.g.  $^{60}\text{Co}$  (average photon energy of 1.25 MeV) have been replaced by modern high-energy (4–20 MeV) linear accelerators increasing the conformity of the dose applied to the tumor. Presently, sophisticated beam delivery methods are developed where a fine beam of high energy Bremsstrahlung is delivered in an intensity-controlled way and is restricted to the target volume by a multileaf collimator. Using the intensity modulated radiotherapy (IMRT) technique a very conformal dose can be applied even to tumors of complex shape. However, the IMRT with photons distributes an unwanted dose over a larger area of normal tissue. In

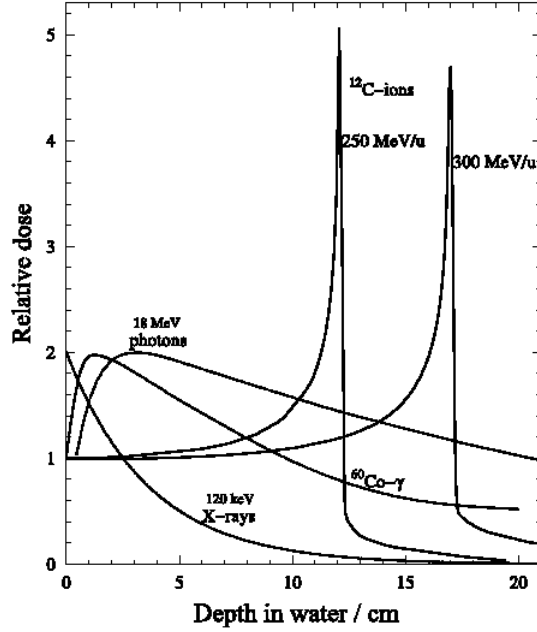


Figure 1.1: Dose depth profiles of photons from different radiation sources and carbon ions in water [24]. Variation of the ion energy allows the sharp dose maximum to be precisely located within the tumor.

addition the low biological effectiveness of these radiation types is inadequate for treatment of radioresistant tumors.

Charged hadrons like protons or heavier ones like carbon ions represent the necessary improvement for the external radiotherapy [24]. Charged hadron beams show an inverse dose profile compared to photons: the dose increasing with penetration depth up to a maximum value (Bragg peak) at the end of the range (Figure 1.1). In addition, ions heavier than protons offer a further reduced lateral scattering and an increased biological effectiveness especially in the region of the sharp dose maximum (Section 1.2).

At the beginning, most of the hadron therapy units were based on nuclear physics accelerators, like the pioneering and no more active one at Lawrence Berkeley Laboratory (LBL), USA, where proton and heavier ion treatment was started in 1954 (*p*), 1957 (He) and 1975 (Ar, Si, Ne) [25–27], as well as the Harvard Cyclotron Laboratory (HCL), USA, which has the longest and most extensive experience in proton therapy since 1961 [1]. The first dedicated hospital-based facilities have been the Loma Linda University Medical Center (LLUMC), USA, operating proton therapy since 1990 [28], and the Heavy Ion Medical Accelerator in Chiba (HIMAC), Japan, which started heavy-ion treatment in 1994 after the shutdown of the LBL accelerator in 1993 [29] and replaced the LBL neon ions by the carbon ions, which seem to offer an optimal compromise between physical selectivity and enhanced biological effectiveness [30]. Since then new proposals and facilities have been fast growing worldwide [1] mostly addressed to proton therapy due to the higher complexity and costs

of heavy ion therapy.

Predominantly, the size of the treatment field is modulated in longitudinal and lateral direction by means of collimators, compensators and range modulators. Using these passive systems, the target volume can be shaped according to the tumor volume in such a way that the tumor is completely covered by the high dose area. But a perfect congruence between irradiated volume and tumor cannot be reached with passive beam shaping systems and frequently a large fraction of normal tissue is contained in the high-dose region causing later-on side effects. In addition, in case of heavy ion beams, the presence of absorbers etc. on the beam line triggers the production of unwanted secondary products (in particular nuclear fragments) that may change significantly the mixed field and consequently the absorbed and the biological dose. In order to improve the situation a novel irradiation technique by active beam shaping, via magnetic deflection, has been introduced for protons at the Paul Scherrer Institute (PSI), Switzerland [31], by means of the spot scanning technique and for carbon ions at the Gesellschaft für Schwerionenforschung (GSI), Germany, with the raster scan device [32]. The three most advanced innovations introduced at GSI are: (i) three-dimensional (3D) conformal beam delivery based on 2D intensity controlled raster scanning in combination with active energy variation from the accelerator [32] (Chapter 4), (ii) radiobiological inverse treatment planning [8] and (iii) *in-situ* therapy monitoring by means of positron emission tomography (PET) [33].

Starting from the GSI experience, new centers are under construction (HIT in Heidelberg, Germany, and CNAO, in Pavia, Italy) and other centers such as, for example, Med-Austron, Austria, ETOILE, France, and Geisse-Marburg, Germany, are planned. This increased interest on hadron therapy, especially in heavy ion therapy, has to be followed by an improvement of the technical devices and treatment planning systems (TPSs) in order to better conform the dose to the tumor minimizing as much as possible the dose delivered to healthy tissue. The presented work addresses the problem of using Monte Carlo (MC) methods by means of the FLUKA code [15, 16] in treatment planning starting from nucleus-nucleus reactions modelling at low energies to CT-based dose calculations and biological effective dose calculations.

## 1.1 The physical basis of ion beam therapy

As already pointed out in the original proposal of R. R. Wilson [34], the main argument for particle therapy is the superior physical selectivity due to the relatively low energy deposition, i.e. dose, in the entrance channel (*plateau*) and a steep increase and fall-off towards the end of the ion path. The resulting sharp and narrow - few millimetres wide - maximum, well known as Bragg peak in memorial of W. H. Bragg [35], can be accurately adjusted in depth by proper selection of the ion energy. This allows to concentrate a higher dose in a deep-seated tumor and keep at the same time the radiation burden to the healthy

tissue in front of and beyond the tumor lower than it would be possible in conventional radiotherapy with photons and electrons. In Figure 1.1 the depth dose profile of electromagnetic radiation is compared to that of carbon ions. For low energy X-rays the stochastic absorption by photo and Compton processes yields an exponential decay of absorbed dose with penetration. For greater photon energies the produced Compton electrons are strongly forwardly scattered and transport some of the transferred energy from the surface to greater depth increasing the dose in the first few centimetres. For high-energy electron Bremsstrahlung, which is mostly used in conventional therapy, the maximum is shifted in a few centimetres from the surface of the patient's body sparing the very radio-sensitive skin. In addition, the exponential decay becomes less steep improving the ratio of entrance dose to the target dose for the treatment of deep-seated tumors. Moreover, the target dose can additionally be increased relative to the nearby healthy tissue by using multifield techniques where the photon beam is brought in from different directions.

Besides the favourable depth properties, the dose delivered by ions is well confined in space also in the lateral dimension due to the low angular scattering which decreases with increasing ion charge and mass numbers [36]. However, in most practical clinical cases, it is necessary to irradiate extended tumor volumes widening the very well localized dose distribution of mono-energetic pencil-like (i.e. of small cross section and low divergence) ion beams in both longitudinal and lateral direction. The longitudinal modification is accomplished by a proper superimposition of several Bragg peaks of different depth, i.e., ion energy (Figure 1.2) obtained either via passive energy degraders or active energy variation from the accelerator. A lateral spread of the dose distribution is achieved either by broadening the transverse beam profile by means of scattering systems or by exploiting lateral magnetic deflection of well-focused

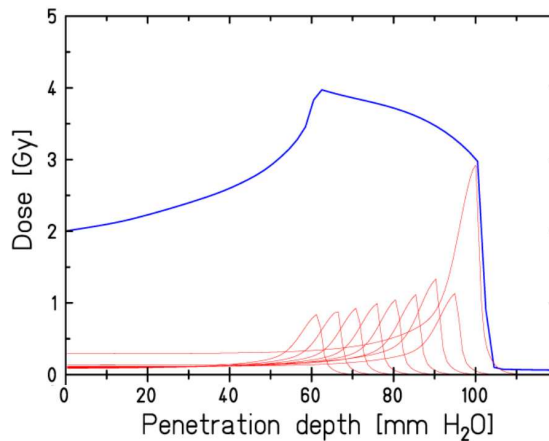


Figure 1.2: A pictorial view of one-dimensional spread-out Bragg peak (blue line) which is the sum of pencil beams of different energies and intensities (red lines).



pencil-like beams [26]. From Figure 1.2 it is evident that the overlap of several Bragg peaks leads to a reduction of the peak to plateau dose ratio with respect to the single mono-energetic case. However, the resulting dose depth distribution well known as *spread-out Bragg peak* (SOBP) is still by far better than that of conventional radiation. Moreover, the entrance dose can be reduced further without changing the tumor dose by exploiting multifield irradiation techniques (i.e. delivering several portals from different directions). Figure 1.2 shows an example of SOBP in carbon therapy: the dose profiles have to be adjusted to the biological efficiency dependence on penetration depth. Due to the increasing of the biological efficiency at the distal edge of a SOBP, the physical dose has to be lowered at the distal edge, in order to make the biological SOBP flat.

In the energy interval of clinical relevance ranging from the initial kinetic energy of about 70-500 MeV per nucleon down to rest, ions transfer most of their energy to the traversed medium in Coulomb inelastic collisions with atomic electrons. The average energy loss per unit path length is known as electronic stopping power and is typically described above about 1 MeV/n by the Bethe-Bloch formula [37, 38]:

$$-\frac{dE}{dx} = 2\pi r_e^2 m_e c^2 N_e \frac{Z^2}{\beta^2} \left[ \ln \left( \frac{2m_e c^2 W_{max} \beta^2}{I^2 (1 - \beta^2)} \right) - 2\beta^2 - 2\frac{C}{Z_t} - \delta \right] \quad (1.1)$$

where  $Z$  and  $\beta$  are the particle charge and velocity (scaled to the speed of light  $c$ ), respectively,  $r_e$  and  $m_e$  are the electron classical radius and rest mass, respectively,  $W_{max}$  is the largest possible energy loss in a single collision with a free electron, well approximated in the non-relativistic limit by  $2m_e c^2 \beta^2$ ,  $N_e$  and  $I$  are the electron density and ionization potential of the medium of atomic number  $Z_t$ , whereas  $C$  and  $\delta$  are the energy and absorber dependent shell and density corrections, respectively. Eq. 1.1 can be extended to lower energies provided that the particle charge  $Z$  is replaced by an effective charge  $Z_{eff}$  keeping into account the mean charge redistribution due to dynamic loss and capture of electrons from the target for ion velocities comparable to the electron orbital velocity ( $\simeq 0.008 c$ ). The functional dependence of  $Z_{eff}$  on the particle speed can be well approximated by the Barkas formula [39, 40]:

$$Z_{eff} = Z \left( 1 - e^{-a\beta Z^{-\frac{2}{3}}} \right) \quad (1.2)$$

with  $a \simeq 125$  in the original proposal of [39].

The functional relation between the electronic stopping power and the particle energy is shown in Figure 1.3 for different ions of therapeutic interest. From the dominant (at not relativistic energies)  $1/\beta^2 \simeq 1/E$  energy dependence in equation 1.1 it follows that the energy loss rate increases as the kinetic energy of the particle diminishes along the penetration depth, with a much steeper rise at low residual energy values corresponding to the last few millimetres of the particle path. At the end of the track, however, the stopping power of

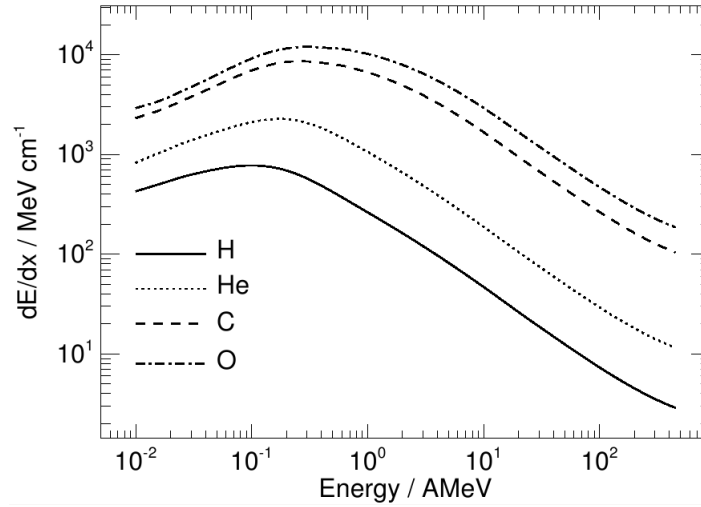


Figure 1.3: Electronic stopping power of different ions of therapeutic interest calculated in water as a function of the energy on the basis of the ATIMA code [41, 42].

heavy ions drops due to the rapid reduction of the ion effective charge  $Z_{eff}$  at very low energy values according to equation 1.2. Hence, the distribution of the ionization density induced by a heavy charged particle along its path shows a rather constant plateau followed by a sharp maximum towards the end, corresponding to the already discussed Bragg curve. The stopping power describes the loss of energy by the incident particle, whereas the absorbed dose refers to the spatial pattern of energy deposited to a medium either directly by the primary ions or by secondary particles (mostly electrons). In most practical conditions secondary electron equilibrium prevails, that means the energy carried in and out of a volume of interest by secondary electrons is on average the same. Under this assumption the macroscopic dose  $D$  delivered by a fluence  $\Phi$  of mono-energetic heavy charged particles to a medium of density  $\rho$  can be directly linked to the average loss  $dE/dx$  of the ion:

$$D = \frac{\Phi}{\rho} \frac{dE}{dx} . \quad (1.3)$$

The description of the heavy charged particle penetration in a medium as a continuously slowing down process at an energy loss rate mainly given by the electronic stopping power, allows to calculate a well defined mean range  $R$  for a given initial energy  $E_0$ :

$$R = \int_{E_0}^0 \left( \frac{dE}{dx} \right)^{-1} dE . \quad (1.4)$$

This integral provides a very close approximation to the length of the finite average path travelled by an ion in a material. In reality, however, statistical fluctuations of the energy loss around its average value occur [43, 44] and cause

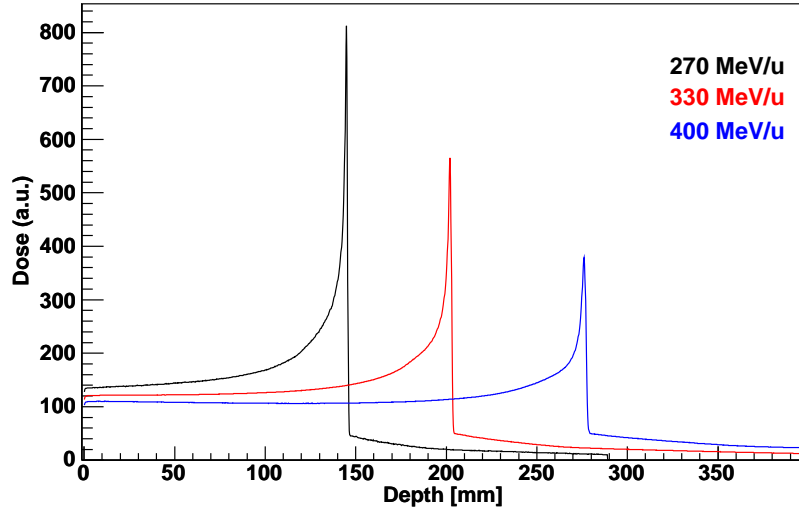


Figure 1.4: Dose depth profile in water calculated by means of the FLUKA code [15,16] for the same number of primary carbon ions at increasing energies. The energy spread  $\Delta E/E$  of the beams is 0.04%.

a small spread of range values around the mean. This phenomenon is known as range straggling and is responsible for the larger width of the Bragg peak measured for an ion beam with respect to the calculation based on the average energy loss of a single particle. The range straggling increases with the penetration depth in a given material, resulting in Bragg peaks of larger width for higher initial energies of the same ion type (Figure 1.4). Whereas the beam attenuation due to nuclear reactions lowers the height of the Bragg peak as initial energy of the beam increases. For different ion species the range straggling approximately varies as the inverse of the square-root of the mass [36]. Therefore, at the same penetration depth heavier ions exhibit a narrower Bragg peak with a steeper distal fall-off and a fragmentation tail beyond the maximum due to nuclear reactions, as it will be described later. In tissue range straggling amounts to about 1% of the mean range for protons and only to 0.3% for carbon ions [36]. Hence, for the latter ones its impact in practical therapeutic applications is smaller or comparable with the unavoidable momentum dispersion of the beam from the accelerator and delivery system. For the clinical application, the lateral scattering of the beam is more important than the longitudinal one. Generally, because of the possible range uncertainties, the treatment planning will avoid a beam just stopping in front of a critical structure. Therefore, tumor volumes close to critical structures can only be irradiated with the beam passing by. How close the beam can get is consequently determined by the lateral scattering, that so is what matters for clinical application. In addition to inelastic collisions with the atomic electrons, heavy charged particles passing through a medium experience also repeated elastic Coulomb collisions

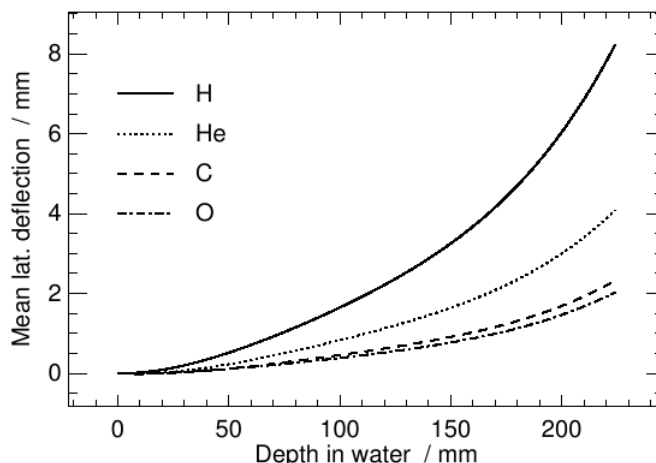


Figure 1.5: Calculated lateral deflection in water of several ion beams of therapeutic relevance [42, 48].

with the atomic nuclei, although with a somewhat lower probability [45]. After several scattering events a lateral spread and divergence is produced in an ion beam. The net angular distribution of the outgoing particles after a thick absorber with respect to the incident direction can be interpreted as the result from several highly probable deflections by small angles as well as rare large-angle single scattering events. The most comprehensive theory of multiple Coulomb scattering within the small-angle approximation is due to G. Molière [46]. However, the central part of the distribution containing very small angular values can be well approximated by a Gaussian shape originating from the statistical repetition of multiple scattering events at small angle ( $<10^\circ$ ) deflections. A good estimate of the standard deviation  $\sigma_\theta$  [rad] is given by the empirical formula [47]:

$$\sigma_\theta = \frac{14.1 \text{ MeV}}{\beta pc} Z \sqrt{\frac{x}{L_{rad}}} \left( 1 + \frac{1}{9} \log_{10} \frac{x}{L_{rad}} \right) \quad (1.5)$$

where  $p$  is the momentum of the particle and  $L_{rad}$  and  $x$  are the radiation length and mass thickness of the traversed medium, respectively. It follows that multiple Coulomb scattering increases as the particle energy decreases. Furthermore, at energies corresponding to similar penetration depths the lateral deflection is more pronounced for lighter ions. A comparison is given in Figure 1.5 for different hadrons of therapeutic interest. Beams of ions heavier than protons show a well confined lateral broadening ( $\leq 1 - 2$  mm) at typical penetration depths of relevance for therapy. However, even protons exhibit much less deflection than electrons because of their considerably higher mass. This produces a much sharper fall-off of the lateral dose distribution which can be very useful for delicate irradiation fields adjacent to critical structures.

Unlike conventional radiation species, heavy charged particles can interact with matter also via strong nuclear force. Nuclear processes in heavy ion col-

lisions differ as a function of energy: production mechanisms go from transfer reactions, observed at low energies, to *pure* fragmentation processes observed at the highest energies, around 1 GeV/n. At low energies ( $< 20$  MeV/n) a lot of data about fragmentation have been collected [49] and different reaction mechanisms contribute to the interaction. At this energy regime, reactions are not considered as *true* fragmentations and they cannot be described as a simple *two-step* process. Because of the low relative velocity between projectile and target the interaction time is long and the Fermi momentum of each nucleon of projectile and target is higher than the nucleus momentum. All these factors could determinate a lot of different processes, that also depend on the impact parameter of the collision, varying from Coulomb scattering to *deep-inelastic* processes and fusion, complete and incomplete. Reactions at higher energies ( $> 200$  MeV/n) are considered of *pure* fragmentation and can be described as a two-step process in which each step occurs in clearly separated time interval. The abrasion interaction is the initial fast process (times order  $10^{-23}$  s) in which the spectator nucleons of both, projectile and target, are assumed to undergo little changes in momentum. This step can lead to highly excited pre-fragments, which are usually very different from the final observed fragments. Before being detected, the pre-fragment, which continues in the original beam direction with practically unaltered beam velocity, loses its excitation energy through the emission of particles, like neutrons, protons and small clusters and gamma rays and re-arranges itself corresponding to the remaining number of protons and neutrons. This second step, that is de-excitation, is slower than the first step with typical times of the order of  $10^{-16} - 10^{-18}$  s, depending on the excitation energy of the pre-fragments. Evidently, transitions between dominant processes occur gradually as a function of the beam energy: their boundaries are not sharp defined. The intermediate energy regime (from 20 MeV/n up to 200 MeV/n) has proved to be very interesting and challenging, both from the experimental and theoretical point of view. In this work it will be presented the new BME event generator (Chapter 2) able to describe, at the moment, light ion reactions at low-intermediate energies ( $< 100$  MeV/n); at higher energy of therapeutic interest it will be briefly outlined the modified version of the rQMD-2.4 event generator [17] (Chapter 3) interfaced with the FLUKA code [15, 16].

As a consequence of nuclear reactions, the fluence distribution of the primary particles is exponentially attenuated in depth  $x$  according to the expression:

$$\Phi(x) = \Phi_0 e^{-N\sigma_R x} \quad (1.6)$$

where  $\Phi_0$  is the initial fluence,  $\sigma_R$  is the total reaction cross section and  $N$  is the atomic density of the medium. From equations 1.3 and 1.6 follow that the dose delivered by the primary ions is reduced with increasing depth due to nuclear reactions. Whereas nuclear recoils give typically negligible contributions to the dose delivery [50, 51], secondary nucleons, particles and fragments produced in nuclear reactions can considerably affect the spatial pattern of

energy deposition and must be carefully taken into account.

In therapeutic applications peripheral collisions in which fragments are stripped of only few nucleons are the most frequent reactions especially in the first few centimetres of depth. For proton beams only target fragmentation is possible. For heavier ions projectile fragmentation is the most important process leading to the build-up of secondary particles along the penetration depth. Because of the reaction kinematics, projectile fragments travel nearly in forward direction at almost the same velocity as the incident particle [52] and may therefore cause further fragmentation reactions, while the target nuclei remain approximately at rest at the interaction point. The secondary lower-charge fragments having a longer range than the primary beam give rise to an undesirable dose deposition beyond the Bragg peak (Figure 1.4). Furthermore, the angular emission of the fragments can contribute to an additional lateral spread of the beam particularly evident at the distal side of the Bragg peak, where the primary projectiles are stopped and the dose deposition is due to nuclear fragments only [24]. Hence, in the case of heavy ions, nuclear fragmentation reactions are responsible for the deterioration of the physical selectivity in the longitudinal and transversal dimension especially around the Bragg peak region. The amount of fragments produced generally increases with increasing mass and charge of the primary particle and is therefore one reason for discouraging the application of ions heavier than neon to therapy.

For heavy ions all the possible drawbacks originating from beam fragmentation are more than compensated by the possibility of *in-situ* beam monitoring using positron emission tomography (PET). Fragments stripped of few neutrons and traveling at almost the same velocity as the parent projectiles may be  $\beta^+$ -radioactive isotopes of the primary stable beam. They stop few millimetres before the primary beam according to the range dependence:

$$R = \frac{A}{Z^2} f(\beta) \quad (1.7)$$

where  $f(\beta)$  is a function of the ion velocity following from equations 1.1 and 1.4. In the case of carbon ion therapy,  $^{11}\text{C}$  and  $^{10}\text{C}$  are the most abundant  $\beta^+$ -emitting projectile fragments with useful half-lives (1222.8 and 19.3 s, respectively) for PET imaging simultaneously to the tumor irradiation or shortly after the end of the treatment ( $^{11}\text{C}$  only). Since the stopping process is faster than the radioactive decay, even in online monitoring, these projectile fragments give rise to a clear and pronounced  $\beta^+$ -activity maximum shortly before the Bragg peak (Figure 1.6) [53]. The depth profile of  $\beta^+$ -activity shows a prominent maximum formed by  $^{11}\text{C}$  and  $^{10}\text{C}$  fragments of the  $^{12}\text{C}$  projectiles, which is superimposed onto a plateau mainly formed by  $^{15}\text{O}$ ,  $^{11}\text{C}$ ,  $^{10}\text{C}$  and  $^{13}\text{N}$  target fragments as shown by analyzing the time dependence of the  $\beta^+$ -activity decay after finishing the irradiation [54]. Due to the half-life of 121.8 s the spatial distribution of  $^{15}\text{O}$  can be detected online only. Since the activated target nuclei stay almost at the place of interaction, their spatial distribution contains further useful information on the lateral localization of the beam and

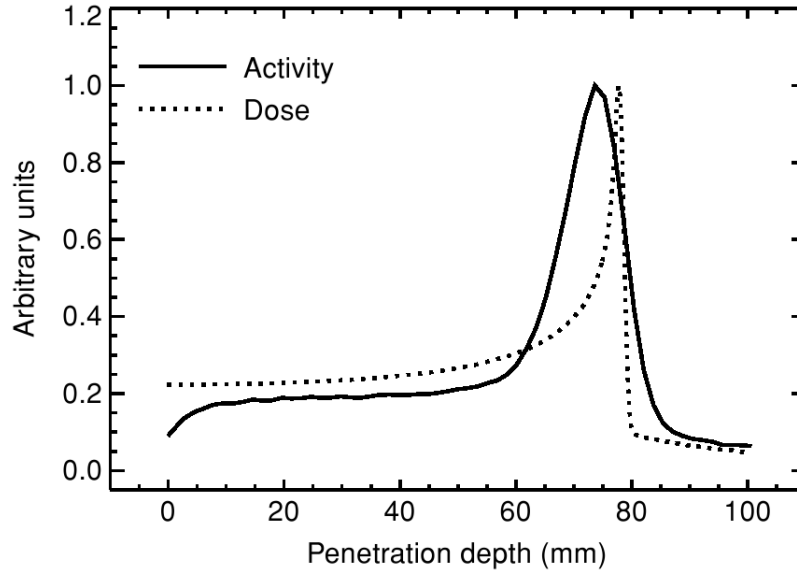


Figure 1.6: Measured  $\beta^+$ -activity (solid curve) in comparison with the calculated dose distribution (dotted curve) for a 212 MeV/n carbon ion beam stopped in a PMMA phantom [53].

of the dose delivery. However, according to the nuclear composition of the tissue and the partial reaction cross sections [55], only a small fraction of the stable beam and of the tissue is activated. This results in a relatively low  $\beta^+$ -activity count rate which demands special requirements in the sensitivity of the PET detector and a reduction of background sources [42]. This technique has a positive clinical impact as already demonstrated both in proton and in carbon ion therapy [33, 42].

## 1.2 The biological basis of ion beam therapy

One of the major rationales for the application of heavy charged particle beams in tumor therapy is their increased biological effectiveness in the tumor volume in comparison to the lower effectiveness in the surrounding healthy tissue. Using the appropriate ion species, the increased effectiveness is most pronounced at the end of the particle range and can thus be essentially restricted to the target volume, whereas the effectiveness is only slightly increased in the surrounding normal tissue. This leads to a further significant increase of the therapeutic gain - defined by the ratio of biologically effective doses in the tumor and normal tissue - compared to proton radiation.

The motivation for the use of high LET particles (heavy ions) from the biological point of view is the fact that they are more effective in cell killing than low LET radiation. This is a consequence of their track structures, their energy deposition is restricted to small subvolumes along the particle trajec-

tory. On the other hand, sparsely ionization radiation like X-rays deposits energy randomly through the cell and produces damage in a stochastic manner. At the microscopic scale of DNA as the sensitive target inside the cell, the elevated ionization density of heavy ions correlates with an elevated density of DNA lesions. Single and isolated lesions like single strand breaks can be repaired easily by the cell. Clusters of double strand breaks (DSB) are frequently connected with information loss at DNA level [24] and mostly irreparable. The hypothesis according to which DSB clusters play a fundamental role in the induction of relevant endpoints such as chromosome aberrations and cell killing has been validated by means of models and MC simulations e.g. by the Pavia group [56–58]. For low doses much of the produced damage can be repaired. While increasing dose the damages become more complex and thus more difficult to repair. This leads to a nonlinear function for the biological response, that can be approximated by a linear-quadratic expression.

For charged particles the energy loss is partially transferred to the liberated electrons which form a track around the particle trajectory. Most of the electrons are ejected with low energy, leading to high ionization densities in the track center close to the trajectory. Due to this high ionization density within the track, the damages in a high LET track are produced close together resulting in a high amount of clustered lesions that are mostly irreparable. As a consequence, a higher effectiveness is observed for high LET radiation.

This increased effectiveness is usually expressed in terms of the relative biological effectiveness (RBE), which is defined as the ratio of the photon dose (typically 250 KV X-rays) and the dose of the particle radiation leading to the same biological effect:

$$RBE = \frac{D_{Photon}}{D_{Ion}} \bigg|_{Isoeffect} . \quad (1.8)$$

The principle of the RBE definition is shown in Figure 1.7. The RBE depends strongly on dose or survival level due to the different shapes of the dose-response curves: shouldered for X-rays and pure exponential for a 11 MeV/u carbon beam for CHO-K1 cells. It is low for high doses and increases for lower doses up to a maximum,  $RBE_\alpha$ , which can be determined as the ratio of the  $\alpha$ -terms representing the initial slopes of the dose effect curves. Also using neutron beams in tumor therapy high RBE values could be reached, however, due to their unfavourable depth dose distribution, this increase of RBE is observed throughout the whole penetration depth of the beam leading not only to an improved tumor control, but simultaneously to significantly enhanced normal tissue complications. In contrast to neutrons, the efficiency of heavy ion beams changes along their path, showing a maximum in the Bragg peak region. This can be explained by the energy dependent track structure characteristics. The diameter of the ion track depends on the range of the ejected electrons and thus on the energy of the ions (Figure 1.8) [5]. For high energies the track is wide and the LET is comparably low. Thus, the distribution



## 1.2. The biological basis of ion beam therapy

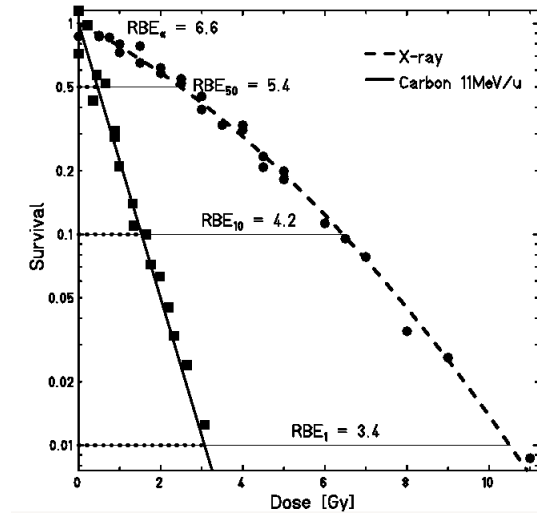


Figure 1.7: Principle of the RBE definition with X-ray curve and 11 MeV/u carbon curve for CHO-K1 cells as example [5].

of ionization events and therefore of the biological damages resemble those of sparsely ionizing radiation, making the repair possible and resulting in the shouldered curves similar to photons. On the other hand, decreasing the en-

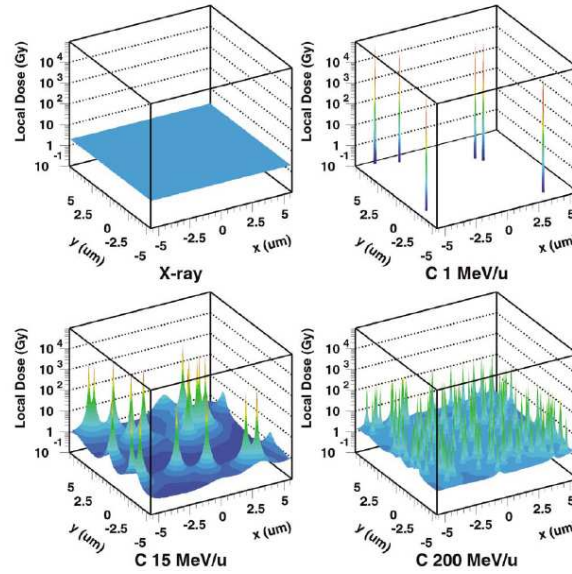


Figure 1.8: Local dose distributions of X-rays and carbon ions at different specific energies. The average dose is 2 Gy in each case. The size of the area is  $10 \times 10 \mu m^2$  and corresponds to the typical size of mammalian cell nuclei [5].

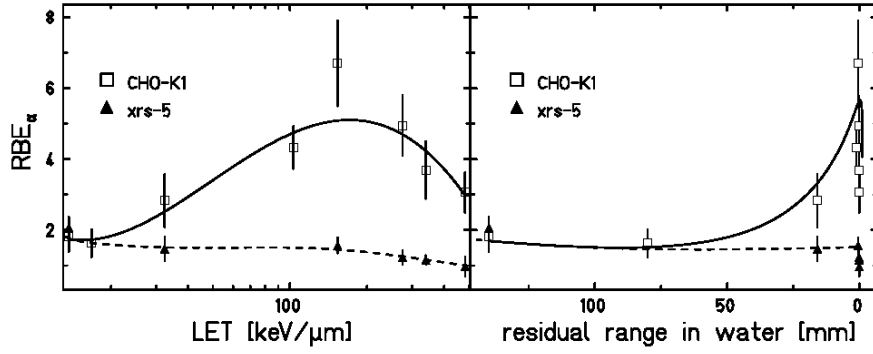


Figure 1.9:  $RBE_{\alpha}$  values for CHO-K1 Chinese hamster ovary cells and their repair deficient mutant xrs-5 for different LET values (left) and plotted as function of residual range in water (right) [5, 59].

ergy the diameter of the track diminishes and LET increases. The resulting higher ionization density leads to more irreparable damages increasing the RBE. Figure 1.9 - left panel - shows the RBE-LET dependence for CHO-K1 cells after carbon irradiation. Plotting RBE as a function of residual range rather than LET (Figure 1.9 - right panel) is clear that the increase of RBE is restricted to the end of the particle range. Thus the high RBE can be confined to the deep seated tumor without dramatic damage to the normal tissue. The dependence of RBE on LET is different for different ions, showing a separate maximum for each atomic number shifting from  $25 \text{ keV}/\mu\text{m}$  for protons [60, 61] to higher LET values for heavier ions [62, 63]. For a given LET the RBE is

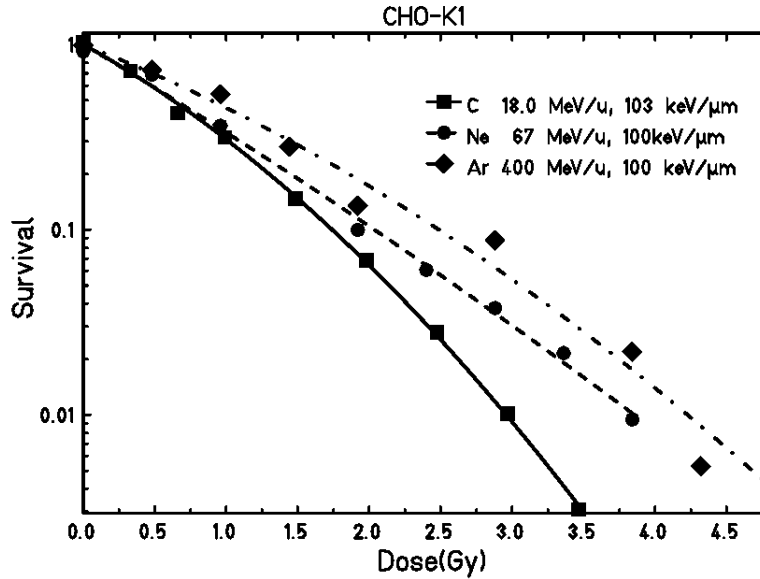


Figure 1.10: Survival curves for CHO-K1 cells after irradiation with ions of different atomic number and LET values of approximately  $100 \text{ keV}/\mu\text{m}$  [5].

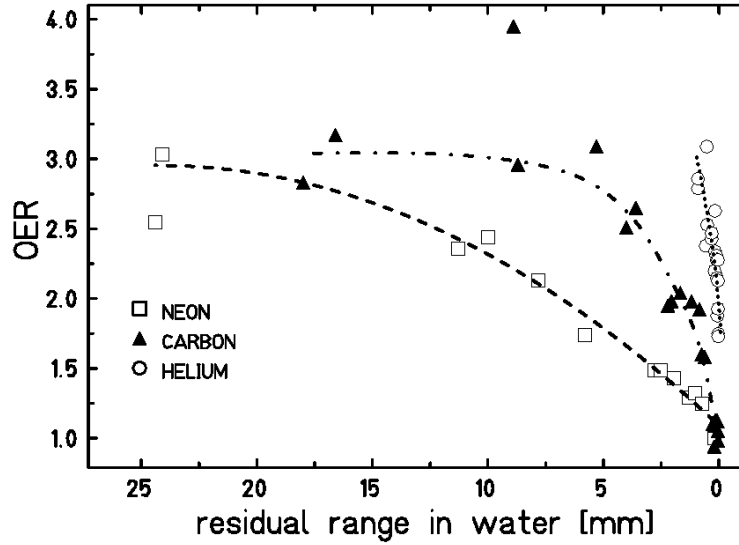


Figure 1.11: OER for neon, carbon and helium. OER and energy data from [65], residual range calculated with ATIMA [41].

higher for the lighter ions (Figure 1.10), as they reach the same LET at lower energies compared to the heavier ones, the diameter of the track is smaller and therefore the ionization density is higher leading to a higher RBE. The impact of the enhanced RBE on tumor killing is highest when the RBE maximum overlaps sufficiently with the Bragg maximum, thus synergistic effects of high dose and high RBE can be obtained. For lighter ions, especially for protons there is only a very sharp RBE maximum at the distal part of the Bragg peak [64], so that RBE is significantly lower in the case of spread-out Bragg peaks, e.g., in the irradiation of extended volumes. For protons a RBE value of 1.1 is used for clinical applications. For ions heavier than oxygen the RBE maximum is shifted with increasing atomic number from the proximal part of the Bragg peak to the plateau, bringing the risk of high-LET effects to the normal tissue, whereas the RBE in the Bragg peak decreases due to saturation effects. For cells with functioning repair system one could find high RBE values [59]. In contrast, for repair deficient cells RBE stays close to one (Figure 1.9). In general for a given particle at a given energy the RBE can be regarded in a first approximation as a function of the  $\alpha/\beta$ -coefficient of the photon dose effect curve, which can be used as a measure of the repair capacity of the cell system [66].

Another important aspect that has to be taken into account is the *oxygen effect*. Low LET irradiation in presence of oxygen causes higher biological damage than in absence of oxygen. The ratio of the doses leading to the same effect in oxic and in hypoxic cells or tissue is called Oxygen Enhancement Ratio (OER). The effect is mainly caused by radiation induced free radicals. The differences in sensitivity between the oxic and hypoxic cells gradually decrease with increasing LET. Corresponding to the decrease of OER, an increase of

RBE is observed for the generally radioresistant poorly oxygenated tissue [65]. For accelerated ions in the entrance OER is similar to photons, whereas in the Bragg peak region it is drastically reduced for heavy stopping particles. Figure 1.11 shows OER values for helium, carbon and neon ions as reported in [65] clearly indicating the drop of OER in the Bragg peak region for the heavier particles. That means that the existence of hypoxic tumor cells will be significantly less relevant with respect to tumor control in the case of charged particle beams as compared to proton or conventional photon beams.

The systematics of the increased RBE has to be considered when using charged particle beams for therapy. It becomes obvious from the different dependencies of RBE, that it cannot be represented by a single number, which can be used to convert physical dose to biologically efficient or photon equivalent dose. In principal, two strategies can be followed [5]: an experimental approach and a modelling approach.

For the experimental approach, the systematics of RBE has to be measured as precise as possible for a large number of different irradiation conditions. However, it will be impossible to represent all clinically relevant conditions with respect to beam energies, size of the target volume, dose levels etc. Thus, interpolation or extrapolation of the data is required. Moreover, since the systematics can be measured only with sufficient precision for *in vitro* systems, procedures have to be defined how to derive RBE values for more complex tissue systems *in vivo* from the measured *in vitro* data.

The second strategy is based on biophysical modelling. The goal is to develop a model which should be able to predict the response to charged particle radiation from the known response of the biological object to photon radiation. This will ultimately also allow to link the treatment planning for charged particle beams to the clinical experience with photon radiation.

The two facilities worldwide treating cancer patients with carbon ion beams are using different strategies. At HIMAC/Chiba, Japan, an experimentally oriented approach is used. This approach also includes a link to the clinical experience with neutrons, which show similar radiobiological characteristics as carbon beams at the end of their penetration depth [67,68]. At GSI/Darmstadt, Germany, the Local Effect Model [2–4] is used, which will be described in more detail in Chapter 5.

# Chapter 2

## Low energy light ion interaction

### 2.1 Introduction

An increasing demand for a comprehensive knowledge of the processes involved in the interaction of two light ions is emanating not only from basic research but also from applications in fields such as hadron therapy or radiation protection studies in space missions. Especially important seems to be the study of the reactions induced by  $^{12}\text{C}$  on nuclei of the biological tissue. In a recent experiment performed at iThemba LABS by our group [69, 70], the interaction of  $^{12}\text{C}$  with  $^{27}\text{Al}$  was studied at an incident energy of 13 MeV/n. This study suggests that the same mechanisms (complete fusion and break-up-fusion [71–76]) which were found to dominate in the interactions of light nuclei ( $^{12}\text{C}$  and  $^{16}\text{O}$ ) with heavier targets, could still account for most of the reactions observed in the interactions of two light nuclei at energies of few tens of MeV/n. Apart from being an important energy range where there seems to be a transition from mean field processes to an increasing influence of nucleonic degrees of freedom, this energy range corresponds to the Bragg peak region (BPR) of higher energy ions interacting with thick materials. In the above-mentioned experiment, intermediate mass fragments (IMFs) with mass larger than the heavier of the two interacting ions were also detected. All these IMFs were produced with quite large cross sections. The analysis of their double differential cross sections showed that these IMFs were produced, in most cases, as evaporation residues in complete fusion (CF) and break-up-fusion (BF) reactions. The extension of this study to even lighter systems, such as  $^{12}\text{C} + ^{12}\text{C}$ , at different incident energies up to the maximum energy available at iThemba LABS (about 35 MeV/n), was considered to allow to further test the adopted theoretical description. Furthermore, it is also of the utmost importance for hadron therapy since it aims to obtain information for estimating the production of positron emitters at energies very close to the BPR and, in addition, to measure the amount of fragments with mass greater than those of the interacting ions. These are mostly produced with relatively low energies (high

LET) increasing the relative biological effectiveness (RBE) of the beam in the BPR, as it will be discussed in Chapter 5.

The production of positron emitters is viewed to be extremely important. Through PET techniques these isotopes can be used for visualizing the beam during irradiation and consequently allowing a better conformation of the irradiated tumor volume [42, 53]. Positron emitter production was measured off beam, e.g., in the  $^{12}\text{C}$  irradiation of a thick PMMA ( $\text{C}_5\text{H}_8\text{O}_2$ ) phantom and mainly revealed the production of  $^{11}\text{C}$  ( $T_{1/2} = 20.39$  min) [54]. The production of  $^{11}\text{C}$  in the  $^{12}\text{C} + ^{12}\text{C}$  reaction was assumed to occur in simple reactions such as  $^{12}\text{C}(\text{p,pn})^{11}\text{C}$  [77, 78]. This conjecture is presumably correct at relatively high energy, but at lower energies, such as those corresponding to the BPR,  $^{11}\text{C}$  could also be produced as an evaporation residue in complete fusion and break-up-fusion reactions together with other positron emitters with either smaller or larger mass than the two interacting ions. This possibility should therefore be carefully investigated as a function of the incident energy in order to accurately relate the positron emitter yield distribution to the dose delivered by the beam in the BPR.

The evaporation residues which, as was mentioned before, may even have larger masses than those of the two interacting ions, have energies considerably smaller than the beam and thus have a very high and localized RBE. As a part of a complete study of the reaction mechanisms, a further objective is an accurate determination of their yields regardless of whether they are positron emitters or not. In the next section the experimental setup is described and the observed spectra shown. In Section 2.3 a new nucleus-nucleus event generator interfaced with the transport and interaction Monte Carlo code FLUKA [15, 16] is outlined and in the Section 2.4 the analysis of the data is discussed.

## 2.2 Experiment

$^{12}\text{C}$  ions with charge state of 4+ produced by an ECR ion source were accelerated by the cyclotron facility of iThemba LABS, South Africa to deliver a beam energy of 200 MeV. The beam was focussed to a spot of less than 3 mm in diameter on the target mounted at the center of a 1.5 m diameter scattering chamber. Events caused by beam halo were monitored by comparing count rates produced by the target and by an empty frame. Beam intensities were kept at levels such that the electronic dead time never exceeded 5%. A  $^{12}\text{C}$  target of a thickness of  $100 \mu\text{g}/\text{cm}^2$  was mounted on an aluminium frame with a 25 mm diameter aperture. The target frame was mounted onto an aluminium ladder, which fits into a target driving mechanism at the center of the scattering chamber. Inclusive spectra of IMFs of  $Z \geq 5$  produced in the  $^{12}\text{C} + ^{12}\text{C}$  reaction at incident energy of 200 were measured with a silicon detector telescope as well as a Bragg Curve Detector (BCD), each mounted inside the scattering chamber on a movable arm. The silicon detector telescope consisted of a 58  $\mu\text{m}$  thick ( $\Delta E$ ) followed by a 1000  $\mu\text{m}$  thick (E) silicon surface barrier

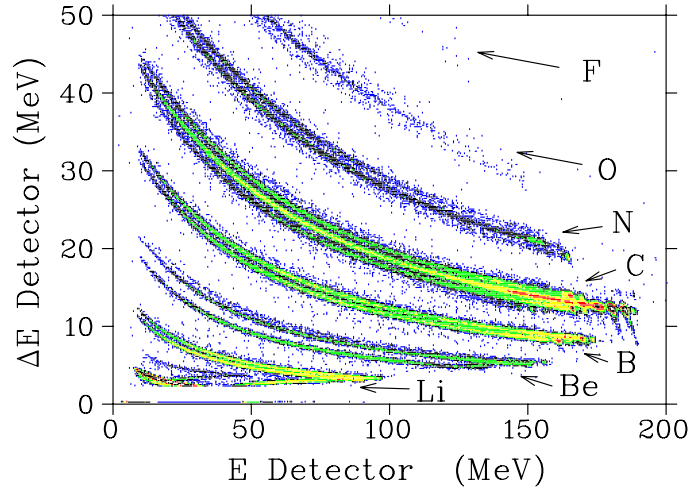


Figure 2.1: Particle identification spectrum of the silicon detector telescope obtained at an emission angle of  $8^\circ$ . The scale of the  $\Delta E$  detector has been reduced to illustrate the obtained mass resolution.

detector. A 8 mm thick brass collimator with a 8 mm thick brass insert was mounted in front of the detector telescope. This insert with an aperture of 8 mm in diameter, defined a solid angle of  $1.132 \pm 0.002$  msr. The full angular acceptance was  $2.2^\circ$ . The BCD had a  $1.1 \mu\text{m}$  thick Mylar entrance window which was coated on the inside with a thin carbon layer of  $2.6 \mu\text{m}$ . The detector volume was filled with isobutane to an absolute pressure of 300 mbar. The BCD, shielded by a 10 mm thick collimator, was mounted at a distance of 394 mm from the target. The collimator opening subtended a solid angle of  $5.189 \pm 0.001$  msr and an angular acceptance of  $4.7^\circ$ . Other design features as well as the modus of operation of the BCD are given in [79]. Under these operating conditions the low energy threshold for particle detection with the BCD was about 1.0 MeV/n while the detector configuration of the silicon detector telescope resulted in the following low-energy thresholds. For the detected B-ions it was (38-40 MeV), for the C-ions (46-50 MeV), for the N-ions (60-62 MeV), for the O-ions (70-76 MeV) and for the F-ions (84-88 MeV), respectively. Particle identification with the BCD was performed in the standard way by displaying Bragg peak signals against the total kinetic energy signals. A VME Flash ADC module was used together with standard NIM electronics to process the preamplifier signals from the anode. Standard  $\Delta E$  - E techniques were used to obtain particle identification as well as isotope separation for most of the fragments detected in the silicon detector telescope. The detectors were calibrated with a standard  $^{228}\text{Th}$  alpha source as well as with the elastically scattered  $^{12}\text{C}$  beams. The double differential cross sections, presented in this chapter, are believed to be accurate within a systematic error of 10%. Energy spectra were measured for most of the isotopes of the fragments which were detected with the silicon detector telescope. The achieved mass resolution is illustrated by the particle identification spectrum shown in Fig. 2.1 for IMFs

emitted at a laboratory angle of  $8^\circ$ . The features of the energy spectra agree qualitatively as well as quantitatively with the spectra measured by Czudek *et al* at the Forschungszentrum Jülich [80] for the same reaction but a higher incident energy.

Experimental double differential cross sections for all the ions with  $6 \leq Z \leq 8$  detected at the laboratory angle of  $8^\circ$  are shown in Fig. 2.2. The C energy spectra are characterized by mainly two features. While the spectra of the  $^{11,12,13}\text{C}$  ions are almost identical, the production of  $^{10,14}\text{C}$  ions has decreased by almost an order of magnitude, maintaining however a similar outgoing energy dependence. Furthermore these spectra are dominated by a broad continuum which extends over more than 100 MeV. At the most forward emission angle of  $8^\circ$  the high energy part of the spectra reveal features of discrete states. These features are extremely sensitive with emission angle as they decrease very rapidly as the angle increases. In order to estimate the relative contributions from the continuum region and the discrete states, the double differential cross sections of the C-isotopes measured at the emission angles of  $8^\circ$  and  $20^\circ$  were first fitted with Legendre polynomials which were then integrated over the outgoing energy. The energy regions which were used to define the continuum are given in Table 2.1. Values of the energy integrated cross sections of the continuum as well as the region corresponding to the discrete states are also presented in Table 2.1. These values indicate that the transfer of a few neutrons seems to play a less significant role even at a very forward emission angle such as  $8^\circ$  and that rather more complex mechanisms like break-up-fusion and complete fusion are required to describe the bulk of the cross section. The scenario also applies to the observed spectra of N-ions and O-ions. In the case of N the two

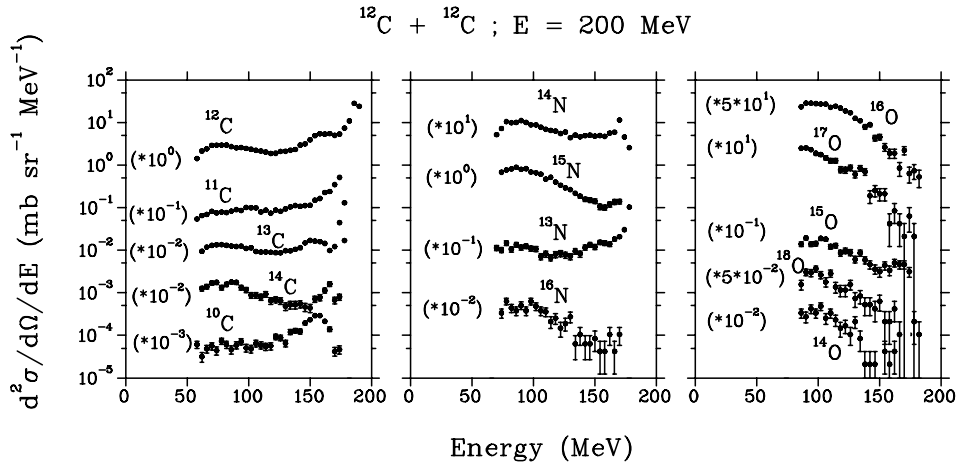


Figure 2.2: Laboratory double differential cross sections of different isotopes of C (left hand panel), N (middle panel) and O (right panel) emitted at  $8^\circ$  in the bombardment of  $^{12}\text{C}$  with 200 MeV  $^{12}\text{C}$  ions as indicated. The error bars reflect the statistical uncertainty. The spectra were multiplied by the indicated factors for clarity of display.



### 2.3. Outline of the theory

C-isotope	Continuum [mb/sr]		Discrete Region [mb/sr]		Continuum Region [MeV]
	8°	20°	8°	20°	
$^{12}\text{C}$	331.6	59.3	447.2	7.4	58-172
$^{11}\text{C}$	94.0	4.2	61.7	0.06	58-160
$^{13}\text{C}$	126.9	40.5	32.0	4.2	62-168
$^{14}\text{C}$	9.4	0.4	2.5	0.02	62-152
$^{10}\text{C}$	4.6	0.3	7.5	0.0	54-132

Table 2.1: Energy integrated cross sections in (mb/sr) of the continuum (energy range given in last column) as well as the discrete regions of the C-isotopes measured at laboratory angles of 8° and 20° in the bombardment of  $^{12}\text{C}$  with 200 MeV  $^{12}\text{C}$  ions.

isotopes  $^{13,14}\text{N}$  seem to be produced in a very similar process to the C-isotopes while  $^{15,16}\text{N}$  start to show a deviation from this trend. The energy spectra of the O-isotopes all roughly follow the same trend. At this emission angle  $^{16}\text{O}$  has the highest yield followed by  $^{15,17}\text{O}$  while  $^{14,18}\text{O}$  are produced with the lowest yields.

## 2.3 Outline of the theory

Many different reaction mechanisms may concur to a light ion interaction: mean field interactions, break-up of the projectile and the target, inelastic scattering, the formation of non-equilibrated nuclei which reach a state of thermal equilibrium through a sequence of two-body interactions in the course of which the emission of fast particles may occur (thermalization) [81]. The equilibrated nuclei which are eventually formed may evaporate particles and  $\gamma$  rays thus leaving a residue which, if radioactive, may further emit beta or alpha particles and  $\gamma$  rays. Consideration of a large set of data suggests in many instances the dominance of complete fusion and break-up-fusion reactions and in these cases the theory has essentially to deal with the description of ion break-up and the de-excitation of the non-equilibrated nuclei which may be created. Ion break-up is usually described in a Local Plane Wave Born Approximation (LP-WBA) [82–85], whereas the thermalization of the excited composite nucleus may be simulated with the Boltzmann Master Equation (BME) theory [86]. Within this theoretical framework a large set of experimental data has been reproduced including double differential spectra of emitted light particles and intermediate mass fragments (IMFs) [71–75, 86, 87] and excitation functions of the evaporative residues [76]. In this section, the main assumptions of the BME theory as formulated by our research group, explained in detail elsewhere [86], are reminded and only its Monte Carlo implementation in the transport and interaction code FLUKA [15, 16] is presented.

The theory describes the thermalization of an excited nucleus by evaluating the variation with time of the distribution of the momenta of its nucleons as

a result of their mutual interactions and their emission into the continuum either as separate entities or as a part of a cluster (a light particle or an IMF). To do that the nucleon momentum space is divided into bins of volume  $\Delta V = 2\pi \cdot m \cdot \Delta\epsilon \cdot \Delta p_z$  (where  $m$  and  $\epsilon$  are the nucleon mass and energy and  $p_z$  is the component of the nucleon momentum along the beam axis) and the time evolution of the occupation probability  $n_i(\epsilon, \theta, t)$  of the states in each bin is calculated. To this aim a set of coupled differential equations, expressing the variation of  $n_i(\epsilon, \theta, t)$  in the time interval between  $t$  and  $t + dt$  as a function of the occupation probabilities at time  $t$  and the decay rates for nucleon-nucleon scatterings and emissions into the continuum, has to be integrated. Initially, the momentum distribution of the nucleons of the excited nucleus is given by a set of  $n_i(\epsilon, \theta, t = 0)$  which depends on the two-ion mean field interaction. The occupation probabilities at a subsequent time  $t$  are evaluated by integrating the set of BMEs given below for proton states:

$$\begin{aligned} \frac{d(n_i g_i)^\pi}{dt} = & \sum_{jlm} [\omega_{lm \rightarrow ij}^{\pi\pi} g_l^\pi n_l^\pi g_m^\pi n_m^\pi (1 - n_i^\pi)(1 - n_j^\pi) \\ & - \omega_{ij \rightarrow lm}^{\pi\pi} g_i^\pi n_i^\pi g_j^\pi n_j^\pi (1 - n_l^\pi)(1 - n_m^\pi)] \\ & + \sum_{jlm} [\omega_{lm \rightarrow ij}^{\pi\nu} g_l^\pi n_l^\pi g_m^\nu n_m^\nu (1 - n_i^\pi)(1 - n_j^\nu) \\ & - \omega_{ij \rightarrow lm}^{\pi\nu} g_i^\pi n_i^\pi g_j^\nu n_j^\nu (1 - n_l^\pi)(1 - n_m^\nu)] \\ & - n_i^\pi g_i^\pi \omega_{i \rightarrow i'}^\pi g_{i'}^\pi \delta(\epsilon_i^\pi - \epsilon_F^\pi - B^\pi - \epsilon_{i'}^\pi) - \frac{dD_i^\pi}{dt} \end{aligned} \quad (2.1)$$

( $\pi$  and  $\nu$  indicate the protons and the neutrons, respectively). An analogous set of equations holds for the neutron states.

$g_i$  is the total number of states in bin  $i$ ;  $\omega_{ij \rightarrow lm}^\pi$ ,  $\omega_{i \rightarrow i'}^\pi$  and  $dD_i^\pi/dt$ , whose explicit expressions are discussed in [86], are, respectively, the internal transition decay rates (the probability per unit time that, in a two-nucleon interaction, the interacting nucleons initially in bins  $i$  and  $j$  scatter to bins  $l$  and  $m$ ), the decay rates for emission of single protons from the  $i$  bin, and a depletion term which accounts for the emission from the  $i$  bin of protons which are part of a cluster. These aggregates may be created, during the cascade of nucleon-nucleon interactions, by coalescence of nucleons with momenta within a sphere of radius  $p_{c,F}$  in momentum space. If not immediately emitted they dissolve into their constituents. The multiplicity spectrum for a cluster is given by

$$\frac{d^2 M_c(E'_c, \theta_c)}{dE'_c d\Omega_c} = \frac{R_c}{2\pi \sin \theta_c} \int N_c(E_c, \theta_c, t) \frac{\sigma_{inv,c} v_c}{V} \rho_c(E'_c, \theta_c) dt \quad (2.2)$$

where  $E_c$  and  $E'_c$  are, respectively, the cluster's energy inside and outside the nucleus and  $N_c(E_c, \theta_c, t)$ , which represents the probability that the momenta of  $(Z_c + N_c)$  nucleons are correlated in such a way to move together as a cluster, is a function of the occupation probabilities  $n_i(\epsilon, \theta, t)$  of the nucleon bins in the coalescence sphere. It is given by

$$N_c(E_c, \theta_c, t) = \Pi_i(n_i^\pi(\epsilon, \theta, t))^{P_i(E_c, \theta_c) Z_c} \cdot \Pi_i(n_i^\nu(\epsilon, \theta, t))^{P_i(E_c, \theta_c) N_c} \quad (2.3)$$

### 2.3. Outline of the theory

---

where the index  $i$  runs over all the bins to which the momenta of the protons and the neutrons of the cluster may belong and  $P_i(E_c, \theta_c)$  is the fraction of bin  $i$  within the cluster Fermi sphere of radius  $p_{c,F}$ .  $\sigma_{inv,c}$  is the cross section for the inverse process (cluster absorption into the residual nucleus),  $v_c$  is the relative velocity between the emitted cluster and the residual nucleus, and  $V$  the laboratory volume which cancels with an equal term appearing in the expression of  $\rho_c(E'_c, \theta_c)$ , i.e., the density of cluster states in the continuum.  $R_c$  is a numerical factor which accounts for the probability that the nucleons constituting the cluster are confined within the cluster volume in the co-ordinate space and that the cluster, once formed, is emitted before separating again into its constituents.

The information so obtained is inclusive, i.e., averaged over many different reaction paths. In other words, the theory provides the mean multiplicities of emitted particles and does not allow one to analyze exclusive processes or evaluate other measurable quantities like, for instance, the cross section for the formation of a particular residue. In order to eliminate such limitations we assume that the probability of emitting a particle  $i$  with energy between  $\epsilon$  and  $\epsilon + d\epsilon$  at a polar angle between  $\theta$  and  $\theta + d\theta$  in the time interval  $(t, t + dt)$  is equal to its differential multiplicity evaluated with the BMEs. The probability of any possible sequence of events may be evaluated as a joint probability using these elementary probabilities. This approach, anyway, cannot easily be integrated into a transport code such as FLUKA because the run-time calculation of the triple differential multiplicity spectra of all the particles which may be emitted through the pre-equilibrium phase, is too time consuming for allowing the simulation of the reactions induced in thick materials. Even the run-time access to pre-computed spectra is out of reach if we have to consider every possible projectile-target-incident energy combination. Thus, so far, to provide the FLUKA code with a more realistic treatment of nucleus-nucleus interactions below 100 MeV/n, it has been adopted the strategy of using the BME theory to describe the complete fusion of a representative set of ion pairs at different energies and fitting the predicted ejectile multiplicities and double differential spectra with analytical expressions containing a small number of parameters. The values of these parameters are stored in a database which may be read by the FLUKA code. This way the simulation of the thermalization for the systems covered by the database, can be performed in the short times needed to make feasible the transport code calculations [88]. The further de-excitation of the excited equilibrated nuclei which are produced is handled by the FLUKA evaporation/fission/fragmentation module. A strategy to allow the extrapolation of the parameter values to systems not processed by the BMEs, is on the way.

Let us describe with some more detail the new event generator implemented in FLUKA (not yet distributed) and its use to reproduce the double differential spectra of the IMFs measured at iThemba LABS. For any pair of interacting ions the reaction cross section ( $\sigma_R$ ) is calculated with an improved

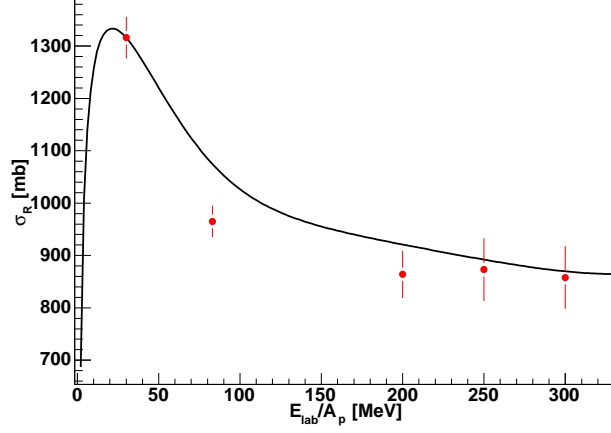


Figure 2.3: Reaction cross section for  $^{12}\text{C}+^{12}\text{C}$  [89]. The experimental values are given by the full red circles, the theoretical estimate by the full line.

version [89] of a model proposed by P. J. Karol [90] (see in Fig. 2.3 the comparison between the experimental values and the theoretical prediction for the interaction of two  $^{12}\text{C}$  ions) and is subdivided into two different mechanisms: the **complete fusion** with probability  $P_{CF} = \sigma_{CF}/\sigma_R$  and a **peripheral collision** with probability  $P = 1 - P_{CF}$ . In case of peripheral collision, the impact parameter  $b$  is randomly chosen using the differential cross-section  $d\sigma_R/db$ . As discussed in [89], the model predicts the formation of rather cold projectile-like and target-like nuclei, and a middle system preferentially excited, the mass number of which is obtained by integrating the projectile's and the target's Fermi densities over their overlapping region. At high impact parameters, this reaction mechanism smoothly develops into a sort of inelastic scattering

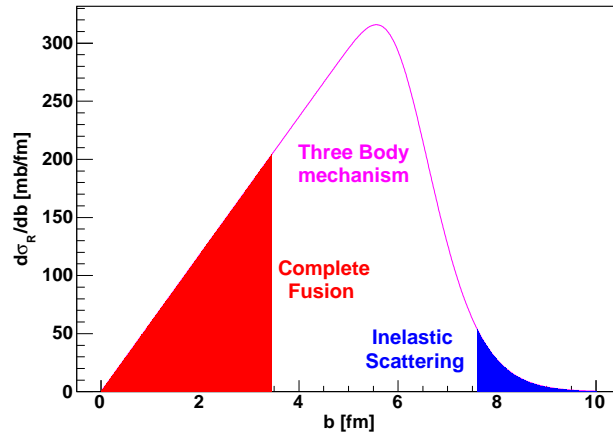


Figure 2.4: Differential reaction cross section for  $^{12}\text{C}+^{12}\text{C}$  at 200 MeV total kinetic energy.

(Fig. 2.4).

To calculate the double differential spectra of fragments produced by peripheral processes, in the  $^{12}\text{C}+^{12}\text{C}$  interaction at 200 MeV the break-up-fusion mechanism has been adopted by coupling a specific code with FLUKA. The binary fragmentation of carbon ions is known from previous studies of the interaction of  $^{12}\text{C}$  with heavier targets. It is reasonably well described in the LPWBA as proposed long ago in [82–85], together with allowing for an energy loss due to an initial state interaction, as discussed in [71–76]. In fact it has been observed that inelastically scattered ions may lose a considerable fraction of their energy [91, 92] and this energy loss may most presumably take place before break-up as well. We assume that the  $^{12}\text{C}$  ion's probability of surviving a break-up or a mass transfer reaction, exponentially decreases with increasing its energy loss, like the averaged inelastic scattering cross section does. According to this picture  $^{12}\text{C}$  breaks up into two fragments: the *spectator* and *participant* one. While the spectator fragment flies away without any further substantial interaction, the participant fragment fuses with the other nucleus. Following the above assumption the spectra of break-up fragments are evaluated by folding the LPWBA cross section with an exponential survival probability [71–73]:

$$P(E_l) = \exp[-C(E_l - E_{l,min})] \quad (2.4)$$

where  $E_l$  is the energy lost by the  $^{12}\text{C}$  ion before break-up and  $C$  and  $E_{l,min}$  are two parameters to be obtained by a best fit to the data (in this work we use the values proposed in [70]). The break-up spectra are then given by

$$\frac{d^2\sigma}{dE'd\Omega}(E_0, E', \theta) = \sigma_{bu} \frac{\int_{E_{l,min}}^{E_0} P(E_l) S(E_0 - E_l, E', \theta) dE_l}{\int_{E_{l,min}}^{E_0} P(E_l) dE_l} \quad (2.5)$$

where  $\sigma_{bu}$  is the angle and energy integrated break-up cross section and  $E_0$  is the initial asymptotic channel energy in the two ion center of mass (CM) system.

In the LPWBA for the spectrum of a fragment emitted at the angle  $\theta$  from the break-up of a nucleus of energy  $E$ , the following expression holds:

$$S(E, E', \theta) \propto P' P'' |\hat{\psi}(\mathbf{P})|^2 \quad (2.6)$$

where  $E'$  is the fragment's energy,  $P'$  and  $P''$  are the linear momenta of the spectator and participant fragments, respectively, at the break-up time in the two ion CM system, and

$$\hat{\psi}(\mathbf{P}) = \frac{1}{(2\pi\hbar)^{3/2}} \int \psi(\mathbf{r}) \exp[-\frac{i}{\hbar}(\mathbf{P} \cdot \mathbf{r})] d\mathbf{r} \quad (2.7)$$

is the Fourier transform of the wave function describing the motion of the spectator fragment within the breaking-up nucleus. The three momenta  $\mathbf{P}'$ ,  $\mathbf{P}''$ , and  $\mathbf{P}$  are related as follows.

$$\mathbf{P}' + \mathbf{P}'' = \mathbf{P}_P \quad (2.8)$$

where  $\mathbf{P}_P$  is the  $^{12}\text{C}$  momentum at the break-up time in the two ion CM system. The spectator fragment's internal momentum in the  $^{12}\text{C}$  ion is

$$\mathbf{P} = \mathbf{P}' - (m'/m_P)\mathbf{P}_P \quad (2.9)$$

being  $m'$  and  $m_P$  the mass of the spectator fragment and the breaking-up nucleus, respectively.

The choice of the wave function  $\psi(\mathbf{r})$  in Eq. 2.7 is tightly connected to the relative angular momentum  $L$  of the considered fragments. The values of  $L$  are determined assuming the breaking-up nucleus and the two fragments in their ground states. For a relative angular momentum  $L = 0$ ,  $\psi(\mathbf{r})$  is evaluated in a square well approximation for the potential acting on the fragment [93]. For  $L \geq 1$ , we adopted for the square of the Fourier transform the expression proposed in [94]

$$|\hat{\psi}(\mathbf{P})|^2 = P^{2L} \exp(-P^2/2P_L^2) \quad (2.10)$$

where the values of  $P_L$  were obtained by a best fitting of the measured spectra. The values of the parameter  $\sigma_{bu}$  for the different modes of fragmentation considered in the calculation (Table 2.2) are obtained *fitting*, at the forward angles, the highest energy data which correspond to the spectator fragment spectra in the projectile fragmentation. Where the experimental data were not available we took the values used in our previous studies [70]. It's worth remarking that the last fragmentation mode reported in Table 2.2 refers to  $^{12}\text{C}(^{12}\text{C}, ^4\text{He})^{20}\text{Ne}^*$  reaction path while the fourth one refers to the more peripheral process  $^{12}\text{C}(^{12}\text{C}, ^8\text{Be})^{16}\text{O}^*$ .

The break-up-fusion mechanism for the studied reaction has been simulated thanks to the coupling of the described binary fragmentation model with FLUKA. In particular, the emission angle and the energy of the spectator fragment are calculated according to the LPWBA while the de-excitation of the excited composite nucleus formed by the fusion of the participant fragment with the partner ion is handled by the FLUKA evaporation/fission/fragmentation module.

Let us focus on the complete fusion reaction path for the system studied in this chapter ( $^{12}\text{C}+^{12}\text{C}$ ) and included in the BME-FLUKA database. Fig. 2.5

Fragmentation	$\sigma_{bu}[\text{mb}]$	L
$^{12}\text{C} \rightarrow ^{11}\text{B} + ^1\text{H}$	100	1
$^{12}\text{C} \rightarrow ^{11}\text{C} + \text{n}$	100	1
$^{12}\text{C} \rightarrow ^{10}\text{B} + ^2\text{H}$	30	2
$^{12}\text{C} \rightarrow ^8\text{Be} + ^4\text{He}$	300	0
$^{12}\text{C} \rightarrow ^6\text{Li} + ^6\text{Li}$	50	1
$^{12}\text{C} \rightarrow ^4\text{He} + ^8\text{Be}$	200	0

Table 2.2: Break-up cross sections and relative angular momenta for the different fragmentation modes considered in the calculation.

### 2.3. Outline of the theory

---

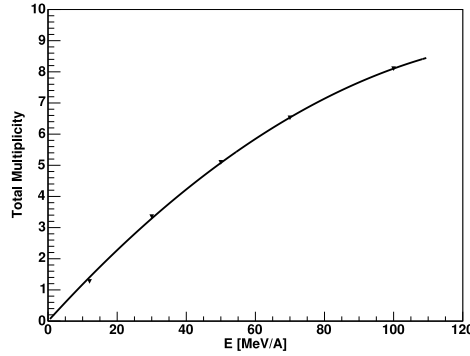


Figure 2.5: Theoretical prediction of the average total multiplicity of pre-equilibrium ejectiles in the complete fusion of two  $^{12}\text{C}$  ions as a function of the incident energy. The triangles give the values predicted by the BMEs, the line is a parabolic fit.

shows, as a function of the projectile incident energy, the average multiplicity of all light ( $Z \leq 2$ ) ejectiles emitted in the pre-equilibrium phase as predicted by the BMEs. The emission probability of some of the ejectiles which may be produced in the pre-equilibrium phase is shown in Fig. 2.6. To extract a possible value for the emission angle of a given particle, we use its predicted cumulative angular distribution  $\int_0^\theta \frac{dM}{d\theta} d\theta$  (in the CM frame) at the considered incident energy. This is obtained by an interpolation from those calculated at a few energies between 10 and 100 MeV/n as shown in Fig. 2.7 in the case of proton. Eventually, to obtain the energy of the ejectile we sample, using the standard rejection methods, from analytical functions (Eq. 2.11) which accurately reproduce its theoretical double differential spectra (in the CM frame), as shown in Fig. 2.8 for pre-equilibrium protons emitted in the  $^{12}\text{C}+^{12}\text{C}$  complete fusion at 30 MeV/n bombarding energy.

$$\frac{d^2M}{dEd\Omega} = E^{P_0(\theta)} \exp(-P_1(\theta) - P_2(\theta)E) \quad (2.11)$$

where  $E$  is the ejectile energy and  $P_0(\theta)$ ,  $P_1(\theta)$  and  $P_2(\theta)$  are parameters depending on the emission angle, particle type, incident energy, and interacting ions.

We get these parameters by interpolating from the values obtained for a few incident energies and emission angles. This way the simulation of the thermalization can be performed in the short times needed to make feasible the transport code calculations.

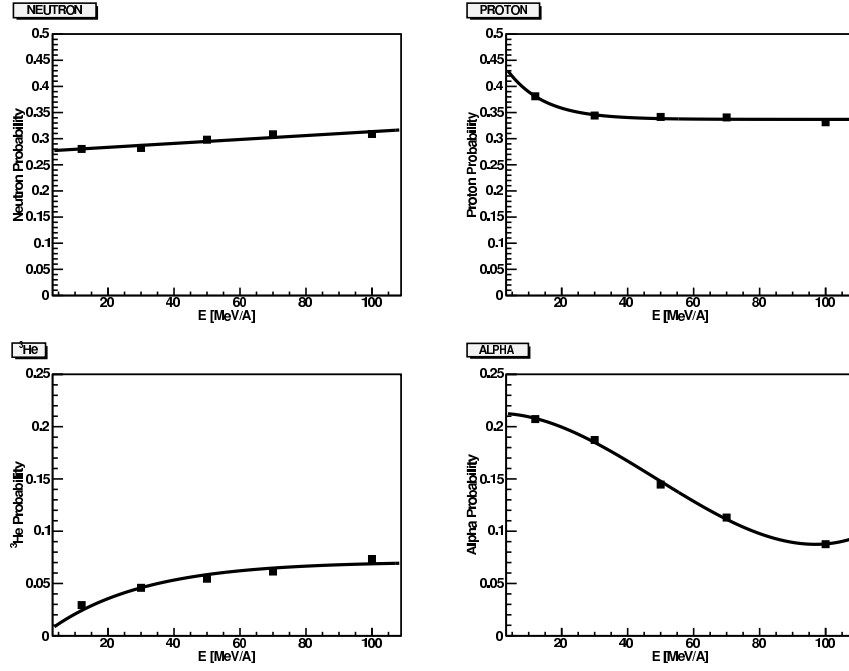


Figure 2.6: Theoretical prediction of the relative multiplicities of a few pre-equilibrium particles (top-left neutrons, top-right protons, bottom-left  $^3\text{He}$  and bottom right alphas) emitted in the complete fusion of two  $^{12}\text{C}$  ions, as a function of the incident energy. This quantity expresses the probability that a particle emitted during the thermalization of the complete fusion composite nucleus be the considered particle. The squares give the values predicted by the BMEs, the lines represent the adopted fit.

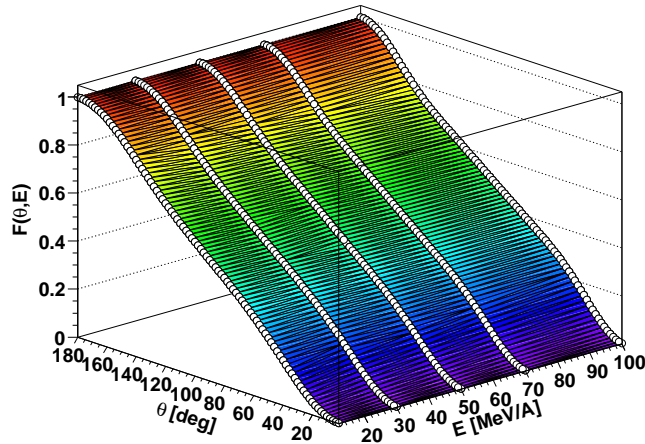


Figure 2.7: Pictorial view of the proton theoretical CUMULATIVE angular distributions in the CM frame.



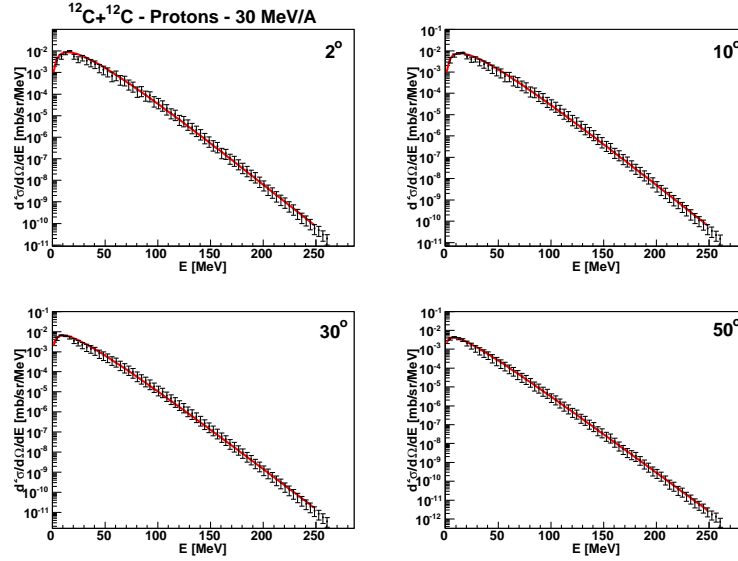


Figure 2.8: Theoretical prediction of double differential spectra (in the CM frame) of protons emitted during the thermalization of the non-equilibrated system formed by the  $^{12}\text{C}+^{12}\text{C}$  complete fusion at 30 MeV/n. The points with the error bars give the BME results, the lines represent the adopted fit.

## 2.4 Comparison of experimental and theoretical spectra

We may divide the observed fragments into two groups:

### a) High A fragments (HAFs) with mass $A > 12$

Among the residues which are observed in this experiment, those with high mass and charge such as the fluorine ( $^{19}\text{F}$  and  $^{20}\text{F}$ , Figure 2.9) and heaviest oxygen ( $^{18}\text{O}$ ,  $^{17}\text{O}$  and  $^{16}\text{O}$ , Figures 2.10-2.12) isotopes are mainly produced by a CF mechanism and the subsequent emission of light particles both in pre-equilibrium and the evaporation stage leaving them as residues. In fact, being of mass significantly larger than that of the interacting ions, it is quite unlikely that they be produced by nucleon coalescence [71–75, 86, 87] in the CF mechanism (the cross section of which is assumed to be about 250 mb) and it is also unlikely that they be produced in BF reactions, since, for instance, the incomplete fusion of a  $^8\text{Be}$  from one of the interacting carbons with the other, produces a  $^{20}\text{Ne}$ , with an excitation energy such that the subsequent pre-equilibrium and evaporation emissions will mainly produce lighter residues. To illustrate this consideration, in Figures 2.11 and 2.12 the contribution of BF processes (just the fusion of a  $^8\text{Be}$  fragment with a  $^{12}\text{C}$  ion, i.e. the most significant one) is shown.

In the case of lighter fragments such as, for instance,  $^{15}\text{O}$ ,  $^{14}\text{O}$ ,  $^{15}\text{N}$  and  $^{13}\text{N}$ , the scenario is more complex. At the moment their spectra are predicted through a hybrid calculation: these nuclei are obtained as evaporative residues

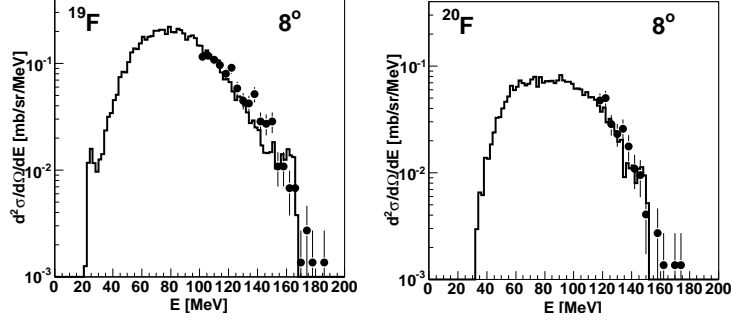


Figure 2.9: Double differential spectra of  $^{19}\text{F}$  (left panel) and  $^{20}\text{F}$  (right panel) in the  $^{12}\text{C}+^{12}\text{C}$  system at  $E_{\text{LAB}}=200$  MeV. Experimental data (full circles with error bars) are compared with the theoretical prediction (black line) given by the contribution of fragments produced in complete fusion reactions.

simulating the complete fusion with the BME event generator and the incomplete fusion with the FLUKA-LPWBA event generator, and finally as IMFs emitted in the pre-equilibrium phase applying the BMEs alone to the complete fusion composite nucleus. The red lines in Figures 2.13 to 2.20 depict the theoretical prediction of the CF mechanism given by the sum of two contributions: fragments produced as evaporative residues and IMFs emitted in the pre-equilibrium phase. This latter increases its importance as the mass of

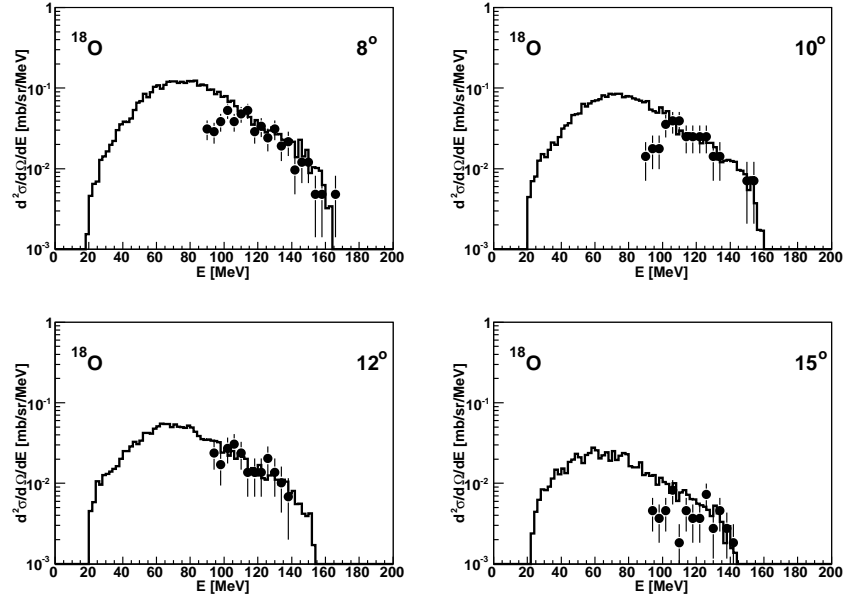


Figure 2.10: Double differential spectra of  $^{18}\text{O}$ . Experimental data (full circles with error bars) are compared with the theoretical prediction (black line) given by the contribution of fragments produced in complete fusion reactions.

## 2.4. Comparison of experimental and theoretical spectra

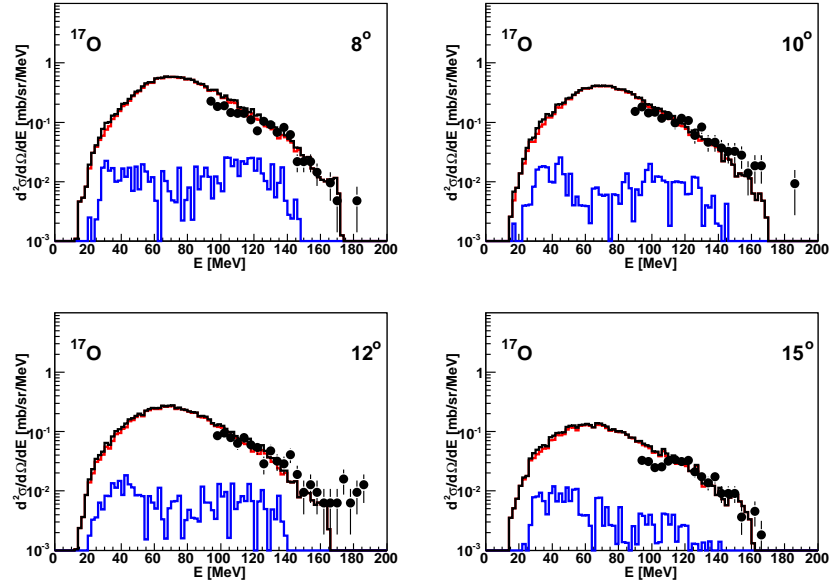


Figure 2.11: Double differential spectra of  $^{17}\text{O}$ . Experimental data (full circles with error bars) are compared with the theoretical prediction (black line) given by the sum of two contributions: fragments produced in CF (red line) and BF (blue line) reactions.

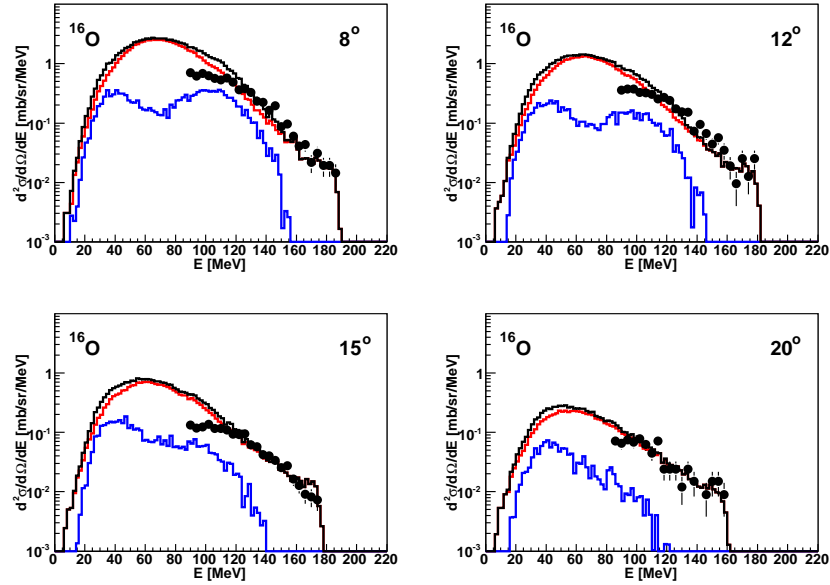


Figure 2.12: Double differential spectra of  $^{16}\text{O}$ . Experimental data (full circles with error bars) are compared with the theoretical prediction (black line) given by the sum of two contributions: fragments produced in CF (red line) and BF (blue line) reactions.

the fragment decreases. On the contrary, the blue lines in Figures 2.13 to 2.17 represent the theoretical prediction of the BF mechanism: fragments produced as evaporative residues in the incomplete fusion reactions.

Figures 2.13 to 2.15 show the comparison of the experimental and calculated spectra of  $^{15}\text{O}$ ,  $^{14}\text{O}$  and  $^{15}\text{N}$ , respectively. These isotopes are mainly produced as evaporation residues in the two C ion CF and in the incomplete fusion of a large number of different fragments of both the projectile and the target with the other ion. The BF role is found to be particularly significant in the case of  $^{15}\text{O}$  and  $^{15}\text{N}$ . The most important BF process for the production of these isotopes is the incomplete fusion of an alpha particle from one of the interacting carbons with the other forming the excited composite nucleus  $^{16}\text{O}$ . The subsequent emission of one neutron or one proton produces  $^{15}\text{O}$  and  $^{15}\text{N}$  as residues, respectively. The residues produced by incomplete fusion of target fragments with the projectile contribute mainly to the high energy part of the spectra while the low energy part is due mainly to projectile fragments fusing with the target. Fig. 2.16 shows the comparison of the experimental and calculated spectra of  $^{13}\text{N}$ . This isotope is mainly produced as evaporation residue in CF and BF reactions and by proton pick-up. Fusion mechanisms account for the quite structureless contribution extending up to about 160 MeV. The high energy peak is due to contribution of proton pick-up, which in fact we describe as break-up of the target nucleus followed by the absorption of the participant proton.

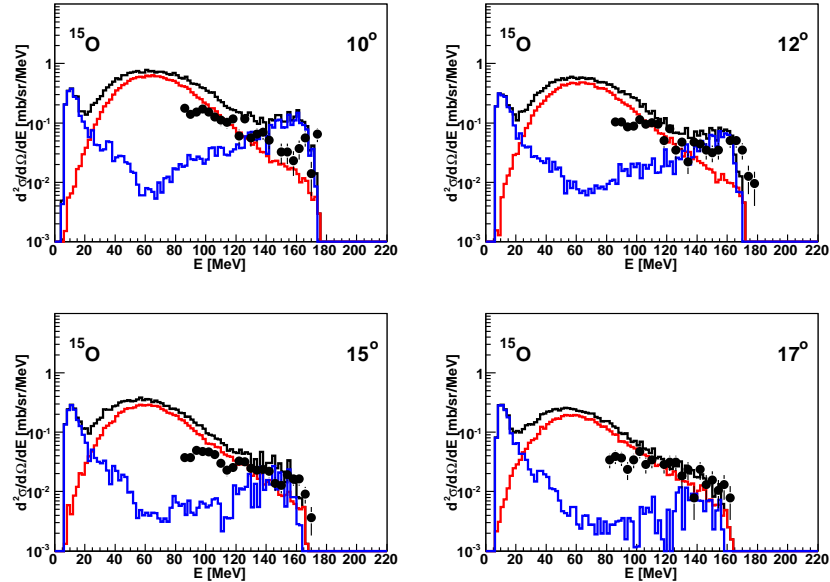


Figure 2.13: Double differential spectra of  $^{15}\text{O}$ . Experimental data (full circles with error bars) are compared with the theoretical prediction (black line) given by the sum of two contributions: fragments produced in CF (red line) and BF (blue line) reactions.

## 2.4. Comparison of experimental and theoretical spectra

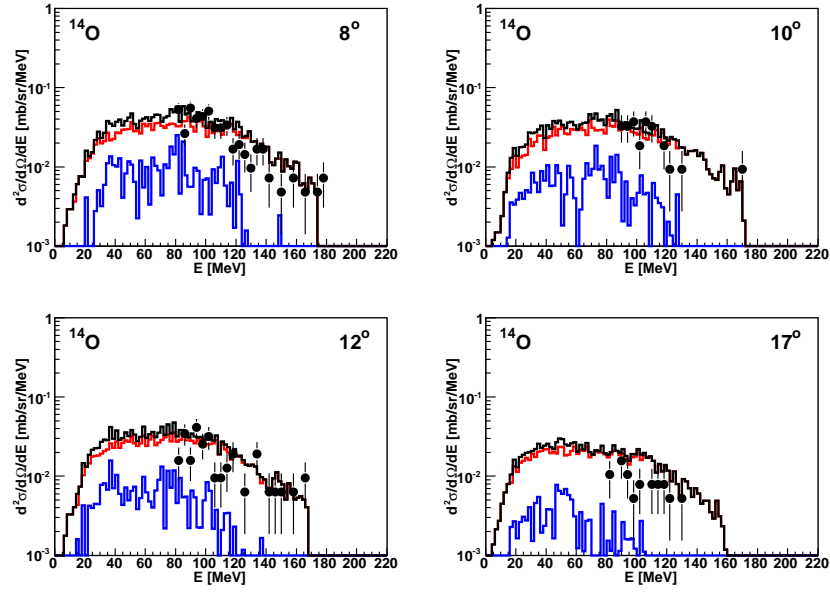


Figure 2.14: Double differential spectra of  $^{14}\text{O}$ . Experimental data (full circles with error bars) are compared with the theoretical prediction (black line) given by the sum of two contributions: fragments produced in CF (red line) and BF (blue line) reactions.

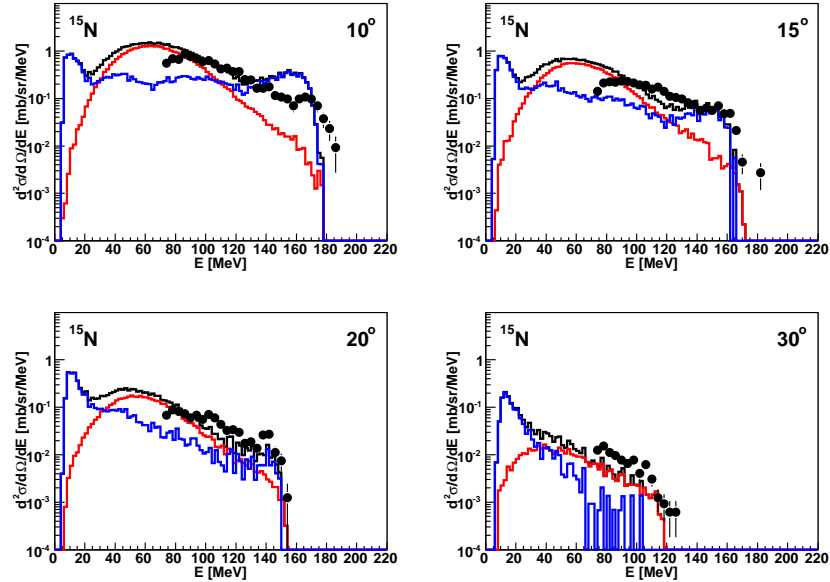


Figure 2.15: Double differential spectra of  $^{15}\text{N}$ . Experimental data (full circles with error bars) are compared with the theoretical prediction (black line) given by the sum of two contributions: fragments produced in CF (red line) and BF (blue line) reactions.

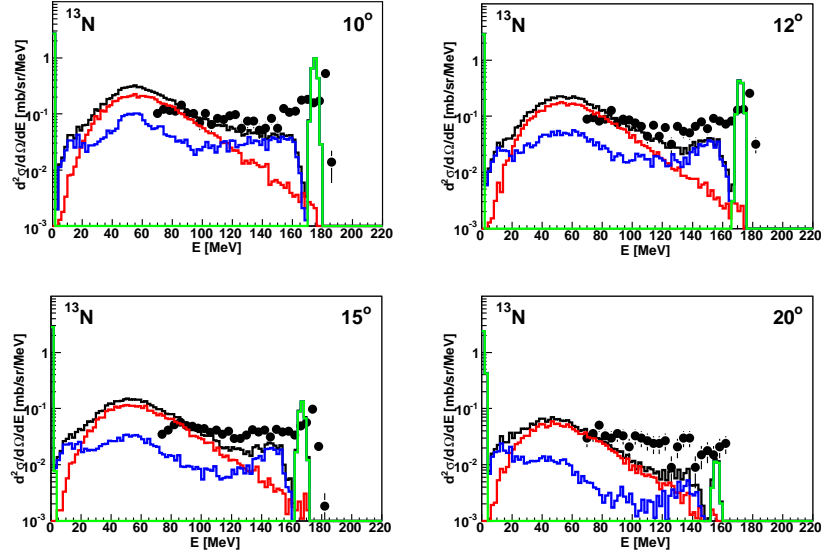


Figure 2.16: Double differential spectra of  $^{13}\text{N}$ . Experimental data (full circles with error bars) are compared with the theoretical prediction (black line) given by the sum of three contributions: fragments produced in CF (red line), BF (blue line) reactions and by proton pick-up (green line).

Fig. 2.17 shows the comparison between the measured and calculated spectrum of O emitted at  $15^\circ$ . The low energy experimental data were measured at iThemba LABS with a Bragg Curve Detector [79] that has a low energy threshold of about 1.0 MeV/n. However, no isotopic identification was possible through this detector. This comparison is significant because it shows that the measured low energy yield is of the expected amount.

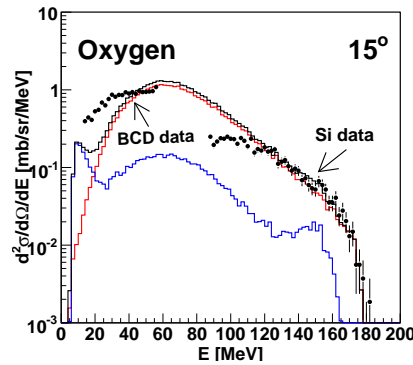


Figure 2.17: Double differential spectrum of O. Experimental data measured with silicon detector telescope and Bragg Curve Detector (full circles with error bars) are compared with the theoretical prediction (black line) given by the sum of two contributions: fragments produced in CF (red line) and BF (blue line) reactions.

### b) Low A fragments (LAFs) with mass A < 12

These fragments are lighter than the  $^{12}\text{C}$  ion and are mainly produced by projectile and target fragmentation as well as nucleon coalescence in complete fusion reactions. The probability that LAFs are produced as evaporation residues is smaller than that of heavier fragments. Figures 2.18 to 2.20 show the comparison of the experimental and calculated spectra of  $^{11}\text{C}$  and  $^{11,10}\text{B}$ . To the production of these nuclei the following processes mainly contribute: at the highest energies they are produced as spectator fragments in the projectile fragmentation and as IMFs in the pre-equilibrium phase, at lower energies they are produced as evaporation residues in the two ion CF and the incomplete fusion of a large number of different fragments of both the projectile and the target with the other ion and as spectator fragments in the target fragmentation. In particular, the green lines in Figures 2.18 to 2.20 refer to the production of these fragments in the following reaction paths:  $^{12}\text{C}(^{12}\text{C}, ^{11}\text{C})^{13}\text{C}^*$  (Figure 2.18),  $^{12}\text{C}(^{12}\text{C}, ^{11}\text{B})^{13}\text{N}^*$  (Figure 2.19) and  $^{12}\text{C}(^{12}\text{C}, ^{10}\text{B})^{14}\text{N}^*$  (Figure 2.20).

Although the agreement between the experimental spectra and the theoretical predictions obtained with the new event generators, by which complete fusion and break-up-fusion reactions were considered, is far from being perfect in several instances, nevertheless the overall comparison with the data shows that these reaction mechanisms certainly play an important role. These mechanisms are not only able to reproduce the qualitative features, which characterize the measured spectra, but in many cases also provide a reasonable quantitative re-

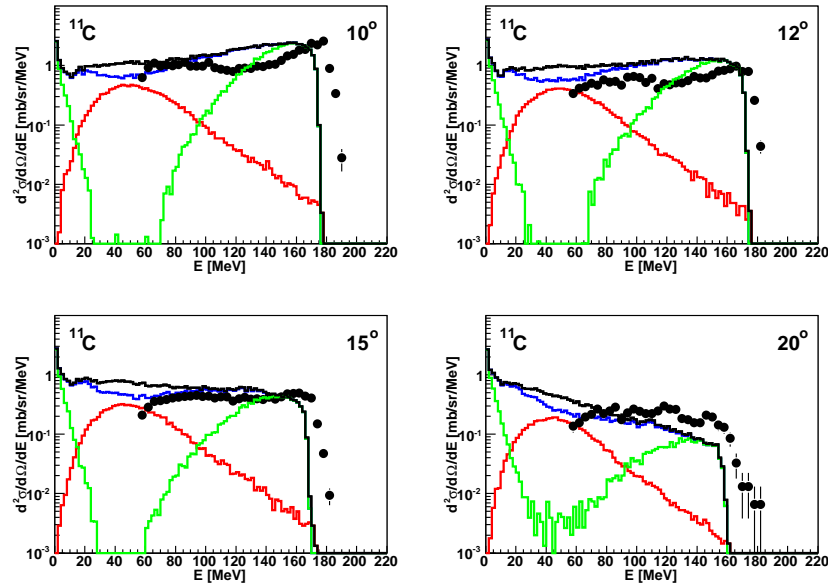


Figure 2.18: Double differential spectra of  $^{11}\text{C}$ . Experimental data (full circles with error bars) are compared with the theoretical prediction (black line) given by the sum of two contributions: fragments produced in CF (red line) and BF (blue line) reactions. The green line refers to  $^{12}\text{C}(^{12}\text{C}, ^{11}\text{C})^{13}\text{C}^*$  reaction path.

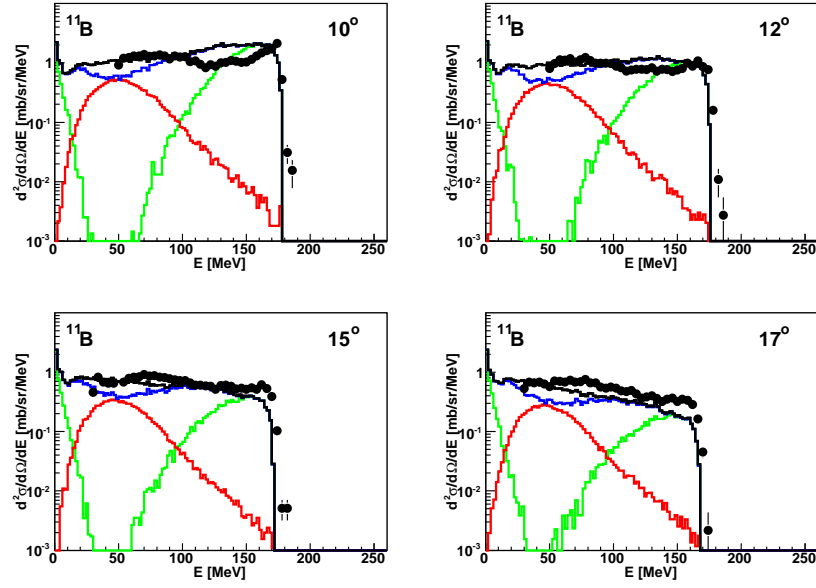


Figure 2.19: Double differential spectra of  $^{11}\text{B}$ . Experimental data (full circles with error bars) are compared with the theoretical prediction (black line) given by the sum of two contributions: fragments produced in CF (red line) and BF (blue line) reactions. The green line refers to  $^{12}\text{C}(^{12}\text{C}, ^{11}\text{B})^{13}\text{N}^*$  reaction path.

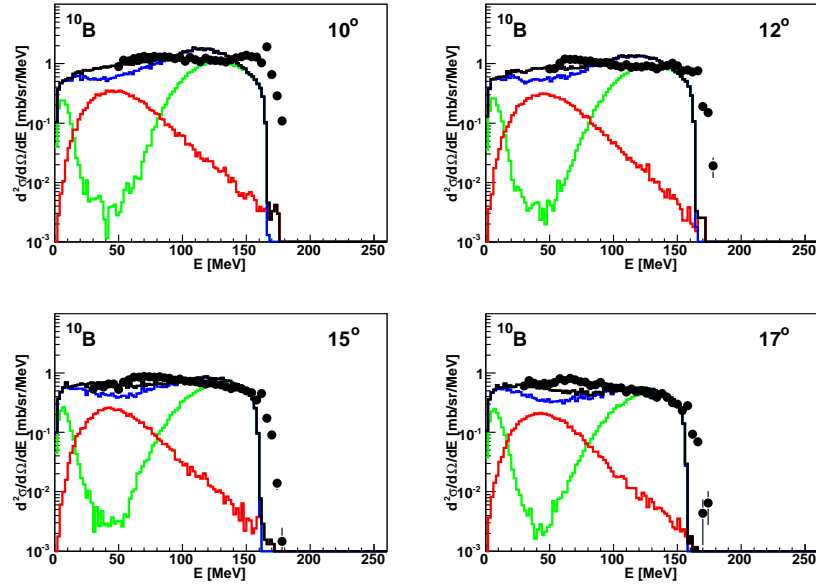


Figure 2.20: Double differential spectra of  $^{10}\text{B}$ . Experimental data (full circles with error bars) are compared with the theoretical prediction (black line) given by the sum of two contributions: fragments produced in CF (red line) and BF (blue line) reactions. The green line refers to  $^{12}\text{C}(^{12}\text{C}, ^{10}\text{B})^{14}\text{N}^*$  reaction path.



## 2.4. Comparison of experimental and theoretical spectra

---

production of the data. In spite of the many simplifications and assumptions which were made to make the calculations of the spectra feasible, such as the description of the nucleon transfer reactions in the LPWBA framework which certainly requires further investigation, the considered mechanisms are shown to prevail.

The reaction cross section for the interaction of  $^{12}\text{C}$  and  $^{12}\text{C}$  is expected to be about 1340 mb [89]. By adding up the cross section of all the mechanisms considered we obtain a total value of about 1030 mb, which corresponds to 77 % of the reaction cross section. The complete fusion cross section contributes for 250 mb, as reported above, and the cross section of the break-up-fusion reactions for 780 mb. If one also includes the probable contribution of inelastic scattering of the two interacting ions, the not unreasonable conclusion is that these reaction mechanisms (complete fusion + break-up-fusion + inelastic scattering) almost exhaust the reaction cross section.



# Investigation of carbon ion fragmentation in water using the FLUKA code

## 3.1 Introduction

In heavy ion therapy nuclear reactions causes a significant alteration of the radiation field. This shows mainly through a loss of primary beam particles and a build-up of secondary lower-charge fragments. Consequently, the dose distribution along the beam path is different as compared to the dose profile resulting from the passage of primary ions in absence of nuclear interactions. In particular, the secondary lower-charge fragments, having longer ranges than the primary beam, give rise to the characteristic dose tail beyond the Bragg peak. The importance of these effects generally increases as a function of the beam energy (or penetration depth). For example, for a  $^{12}\text{C}$  beam at 200 MeV/n about 30% of the primary carbon ions undergo nuclear reactions and do not reach the Bragg maximum at about 8.6 cm depth in water whereas at 400 MeV/n only the 30% of the primary particles reach the Bragg peak at about 27.5 cm depth in water [18].

Nuclear processes in heavy ion collisions differ as a function of energy. In the energy interval of therapeutic interest, interaction mechanisms go from *pure* fragmentation at highest energies to more complex ones at the lowest energies. Depending on the nuclear structure of the interacting ions and on the impact parameter, the low energy reaction mechanisms vary from Coulomb Scattering to *deep inelastic processes* and fusion, complete and incomplete. In the FLUKA code nucleus-nucleus reactions relevant for therapeutic applications are treated thanks to the interfaces with the RQMD [17] and the new BME event generator (Chapter 2).

The use of ion beams in therapy requires very accurate understanding of the complex processes of the ion interaction with matter, especially regarding the

production of secondary particles. In fact, during radiation therapy, secondary neutrons, protons and heavier ions contribute to the dose delivered to tumor and healthy tissues outside the treated volume. Production of light fragments is of special interest since these particles are transported through the patient broadening the irradiation field and increasing the risk of secondary tumors in healthy tissues. In addition, the secondary particles leaving the patient, mainly neutrons, are important for studying the radiation background in the therapy room. Furthermore, the biological efficacy of the reaction products is different from the primary ions and has to be included in the biological effect calculations (Chapter 5).

In this chapter, after a brief account of the FLUKA code [15, 16] (Section 3.2), the RQMD event generator is benchmarked against the mixed field measured at GSI for a 400 MeV/n carbon beam on water phantoms [18, 19] (Section 3.3 and Section 3.4). The preliminary data [18, 19] (partially still unpublished) resulting from the experiments and the analysis performed at GSI by E. Haettner, H. Iwase and D. Schardt *et al.* were kindly provided by K. Parodi and S. Brons (HIT). The FLUKA calculations shown within this chapter, warmly supported by the colleagues from HIT, are obtained using a development version of the official release (*fluka2006.3b*) which includes the FLUKA-BME interface in order to treat nucleus-nucleus reactions at low energies (Chapter 2).

## 3.2 FLUKA code capabilities

FLUKA [15, 16] is a general purpose Monte Carlo code describing particle transport and interaction with matter, covering an extended range of applications spanning from proton and electron accelerator shielding to target design, calorimetry, activation, dosimetry, detector design, Accelerator Driven Systems, space radiation and cosmic ray showers, neutrino physics, radiotherapy. About 60 different particles plus heavy ions can be transported by the code. The energy range covered for hadron-hadron and hadron-nucleus interactions is from threshold up to 10000 TeV, while electromagnetic interactions can be dealt with from 1 keV up to 10000 TeV. Neutron transport and interactions below 20 MeV down to thermal energies are treated in the framework of a multi-group approach, with cross section data sets developed for FLUKA starting from standard evaluated databases (mostly ENDF/B-VI, JENDL and JEFF). Transport in arbitrarily complex geometries, including magnetic field, can be accomplished using the FLUKA combinatorial geometry. In the following, some of the most important capabilities of the FLUKA code relevant to the reproduction of the GSI experimental data are briefly outlined; description of other FLUKA models and extensive benchmarking can be found in the literature (see the FLUKA website <http://www.fluka.org>).

In FLUKA, the transport of charged particles is performed through an original Multiple Coulomb scattering algorithm [95], supplemented by an optional single scattering method. The treatment of ionization energy loss is

based on a statistical approach alternative to the standard Landau and Valivov ones that provides a very good reproduction of average ionization and fluctuations [96]. Multiple scattering with inclusion of nuclear form factors is applied also to heavy ion transport. Up-to-date effective charge parametrizations are employed, and straggling of ion energy loss is described in *normal* first Born approximation with inclusion of charge exchange effects. The precise determination of ion range and ionization losses is of utmost importance in dosimetry and in therapeutical applications. For this reason, FLUKA is being heavily benchmarked [97] against models and experimental data concerning ion beams of interest for hadron therapy. Such a validation for a 400 MeV/n carbon beam on a water phantom will be outlined in the next section.

Nucleus-nucleus interactions are also supported [98,99] up to 10000 TeV/n, thanks to the interfaces with a modified version of rQMD-2.4 [17] and with DPMJET-III [100]. The implementation of the Boltzmann Master Equation (BME) theory for nucleus-nucleus interactions below 100 MeV/n, as partially described in Chapter 2, is ongoing. At higher energies, Quantum Molecular Dynamics (QMD) models represent a suitable way to describe the initial hot stage of heavy ion reactions. It was decided to use a relativistic QMD code (named rQMD-2.4) developed in Frankfurt as a solution to cover the energy range between 100 MeV/n and 5 GeV/n. Above this threshold the DPMJET-III event generator - based on the two component Dual Parton Model in connection with the Glauber formalism - is used. The original version of the RQMD code has been successfully applied to A-A particle production over a wide energy range, however, it does not identify nucleon clusters in the final state. Thus their de-excitation by pre-equilibrium emissions, fission, evaporation, or fragmentation cannot be evaluated. This is a quite severe limitation: in fact, because of huge kinematical effects, ejectiles having low energy in the reference frame of the decaying projectile-like nucleus may contribute to the highest energy side of observed spectra at forward angles. At bombarding energies of interest, serious energy non-conservation issues are also affecting the original code, particularly when run in full QMD mode (rQMD-2.4 can run either in full QMD mode or in the so called *fast cascade* mode where it behaves like an Intra Nuclear Cascade code). Therefore a meaningful calculation of residual excitation energies is impossible. It has been then developed a modified version of rQMD-2.4, where projectile- and target-like residues are identified by gathering the spectator nucleons, and their excitation energies are assumed to be essentially due to the holes left by the hit nucleons. Moreover, the exact energy balance is assured taking into account the experimental binding energies of nuclei, as is the case for all other models used in FLUKA. After these improvements, the fragment final de-excitation can be reasonably evaluated by the FLUKA evaporation/fission/fragmentation module. Examples of the FLUKA performances, when running with the modified rQMD-2.4 event generator, can be found in [98,101]. They concern double differential neutron spectra for Fe and Ar ions at 400 MeV/n bombarding thick Al targets [102],

and fragment charge cross-sections for 1.05 GeV/n Fe ions on thin Al and Cu targets [103]. In addition, a promising result has been obtained in an even more demanding test represented by the analysis of 24 isotopic distributions of fragmentation products measured at GSI for the reaction  $^{238}\text{U} + ^{208}\text{Pb}$  at 750 MeV/n [101, 104]. Work on a further development of rQMD-2.4, in order to calculate the pre-equilibrium de-excitation of the projectile- and target-like residues by the FLUKA module based on the exciton model, is ongoing. This is an important improvement for a more accurate evaluation of the equilibrated nucleus excitation energy, to be spent on evaporation/fission/fragmentation.

For very light ions, namely from deuterons to alpha particles, the FLUKA developers are instead implementing an approach based on the already existing hadronic interaction model. This model, called PEANUT [105, 106], includes a detailed intranuclear cascade stage, coupled to preequilibrium and equilibrium particle emission.

## 3.3 Characterization of the primary beam

The nuclear interactions undergone by an ion beam in a thick target lead to a loss of primary ions and a build-up of secondary fragments. While the characteristics of the charged secondaries will be described in the next section, here we focus on the experiments [18, 19] together with the FLUKA calculations performed in order to investigate the properties of a 400 MeV/n  $^{12}\text{C}$  beam on water phantoms. This beam energy is not typical for treatment (especially in head and neck patients, because of the corresponding very high penetration depth in water) but is a good extreme case for testing the nuclear models. The aim of this section is to validate the FLUKA code against experimental data concerning Bragg curve and beam attenuation profile as a function of depth in water.

### i) Experimental methods

Bragg curve in water was measured at GSI for a 400 MeV/n  $^{12}\text{C}$  beam using two ionization chambers: a small one placed behind the beam exit window and a greater one downstream to the target (more details about the experimental procedure can be found in [18]). In order to calculate the absolute Bragg peak (BP) position in water, the water-equivalent thickness of all the materials along the beam path was measured using a 150 MeV/n carbon beam. The resulting BP was  $27.5 \pm 0.05$  cm [18].

For the attenuation experiment, indeed, the objective of the measurements was to provide the number of surviving carbon ions, normalized to the primary beam ions, leaving the water phantom as a function of its thickness. A sketch of the experimental setup is shown in Figure 3.1. It was assumed that the number of carbon ions hitting the target was equal to the number of ions hitting the Start detector. Possible nuclear interactions before the target were neglected. However, some of the carbon ions, depending on the phantom

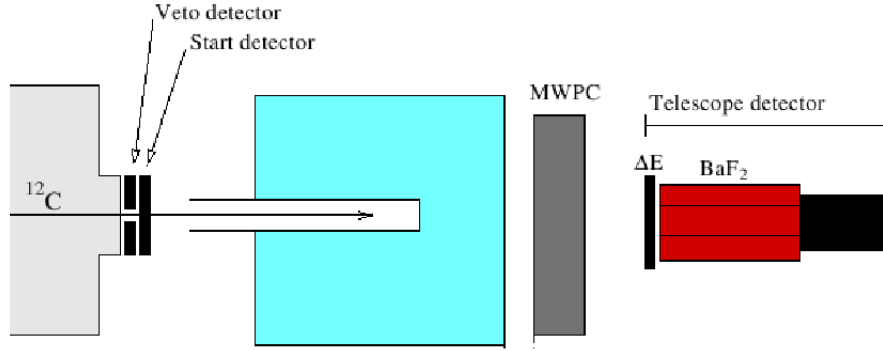


Figure 3.1: Sketch of the experimental setup for the beam attenuation experiment [18].

length, undergo nuclear reactions with the target nuclei. Hence, the secondary particles had to be identified. For this purpose, a  $\Delta E$ - $\text{BaF}_2$  telescope detector [107], which provides energy loss and total energy information, has been used. In addition, the time-of-flight (TOF) was measured between the Start and the telescope detector contributing to the particle identification. Moreover, a position sensitive multi-wire proportional chamber (MWPC) was used in order to control that the solid angle covered by the telescope detector was large enough to detect all the carbon ions emerging from the target.

#### ii) The simulation approach

One of the fundamental conditions for using a Monte Carlo code for validation of a treatment planning in ion therapy is the sub-millimetre agreement with the BP position experimentally measured in water phantoms. The range of a charged particle mainly depends on the electronic stopping power. A possible way to achieve an agreement between the particle range obtained by FLUKA and the one experimentally measured is to adjust the stopping power of water in the simulation. In FLUKA this can be accomplished by changing the ionization potential (I). Its standard value is set to 75 eV, according to ICRU recommendations ( $75 \pm 3$  eV) [108], values up to 80 eV can be found elsewhere [109]. As pointed out in [97], the optimal value of I to use in FLUKA to have a sub-millimetre agreement with the particle range predicted by the treatment planning system TRiP [7] (Chapter 4) is 80 eV. Furthermore, using this value, the FLUKA calculations agree with the Bragg curves experimentally measured for 270 and 330 MeV/n carbon beams on water phantoms [97]. However, for the simulations presented within this chapter it has been found that the optimal value to reproduce the experimental data is 76.75 eV. In the calculations, the nominal beam energy, 400 MeV/n, with a Gaussian energy spread of 0.2 MeV/n (FWHM) is used. The cited inconsistency of I given by several literature sources [110] suggests the need for more accurate, facility independent, experimental investigations for an objective assessment of the true stopping power values, which is beyond the purpose of this work.

In order to simulate the measured Bragg curve with FLUKA, the target was

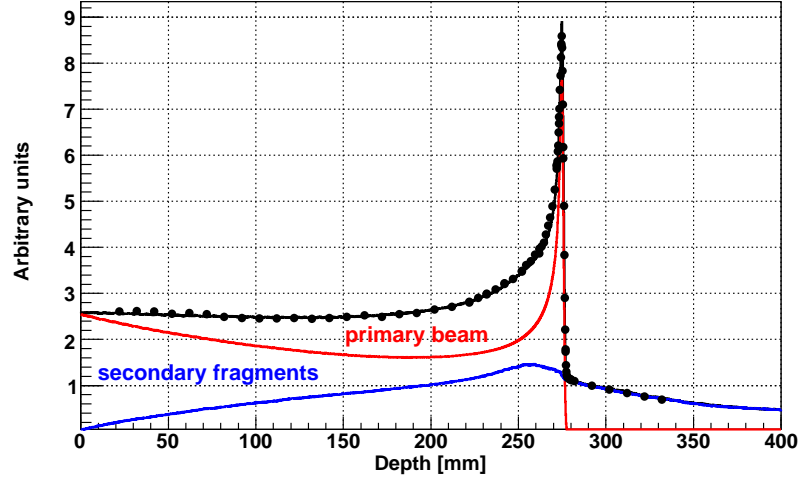


Figure 3.2: Bragg curve of a 400 MeV/n carbon beam on water. The points [18,19] give the experimental data while the black line represents the FLUKA results. The red and blue lines show, respectively, the contribution from primary  $^{12}\text{C}$  ions and secondary fragments. Both the experimental data and the MC results are normalized by the integral of the Bragg curve calculated between the entrance region and the BP.

modelled as a single block of water and the plastic around the water and the materials in the beam path were neglected because already taken into account in the experimental data. To achieve good statistics, especially for determining the energy deposition from secondary fragments, the simulation was run ten times each for  $5 \times 10^4$  primaries and different random number sequences. A nice agreement with experimental data is shown in Figure 3.2, where the con-

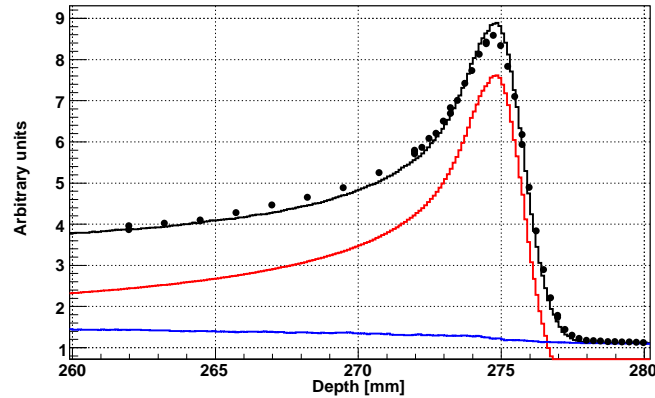


Figure 3.3: Close-up of the peak shown in Figure 3.2. Both the experimental data and the MC results are normalized by the integral of the Bragg curve calculated between the entrance region and the BP.



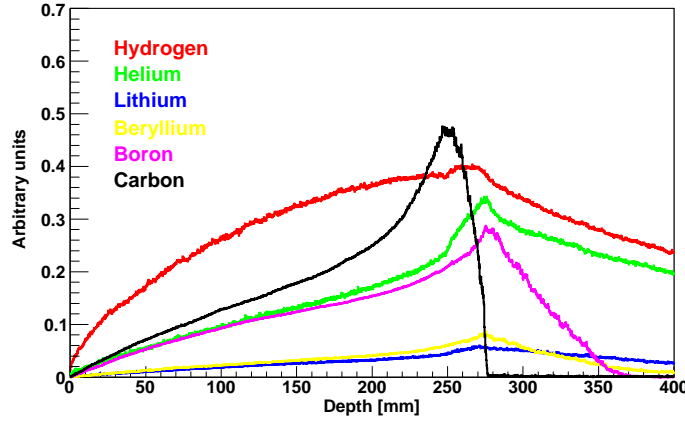


Figure 3.4: Simulated contributions of the indicated secondary particles to the Bragg curve shown in Figure 3.2.

tribution from primary  $^{12}\text{C}$  ions and secondary fragments is depicted. Depth dose profile calculated by FLUKA reproduces very well the experimental values in the entrance region and, thanks to the adopted value of  $I$ , in the position of the BP (Figure 3.3). Both the experimental data and the Monte Carlo results are normalized by the integral of the Bragg curve calculated between the entrance region and the BP because the experimental data are obtained as relative values. Figure 3.2 also indicates that the dose beyond the Bragg peak (tail) predicted by FLUKA agrees with the experimental one. The tail, as well-known, is due to the lower-charge fragments with longer ranges than the primary beam produced principally in the projectile fragmentation. It consists mainly of H and He fragments but a not negligible contribution is due to heavier fragments such as boron (Figure 3.4). Its correct estimation is demanded for a reliable determination of the dose delivered to the healthy tissues in the proximity of the treated tumor.

For comparison with the attenuation experiment, similarly to [97], instead of running individual simulations with water phantoms of variable lengths, only one simulation was performed, where the number of carbon ions was registered at different positions in the target. At the end of the simulation a nearly continuous attenuation curve is obtained by normalizing with the number of simulated histories. Also in this case the phantom was modelled as single block of water and all the materials along the beam path were neglected. The  $I$  of water, as for the Bragg curve calculations, was set to 76.75 eV. Experimentally, the carbon ions were identified by their energy loss and by their total energy using a  $\text{BaF}_2$  detector or the TOF technique. However, no isotopic separation was performed. So, all the resulting carbon ions, not only the primary beam, have to be included for the comparison with the experimental data. The number of carbon ions ( $N_c$ ) normalized to the primary simulated histories ( $N_0$ ) as a function of depth in water is shown in Figure 3.5. In addition to the atten-

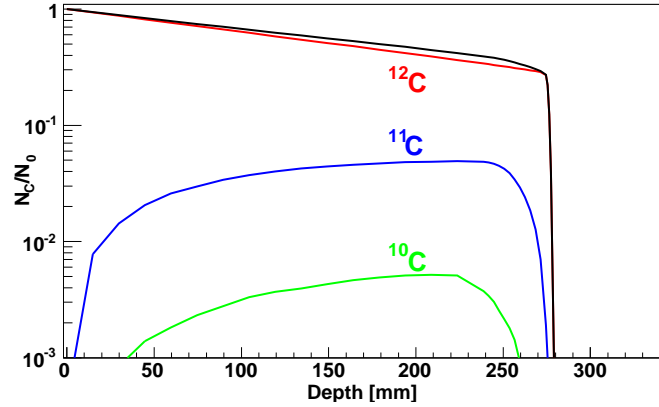


Figure 3.5: Attenuation of a 400 MeV/n  $^{12}\text{C}$  beam together with the build-up of secondary carbon ions as a function of depth in water:  $^{12}\text{C}$  (red line),  $^{11}\text{C}$  (blue line) and  $^{10}\text{C}$  (green line). The back line represents the total prediction.

uation of the  $^{12}\text{C}$  beam, the build-up of secondary C ions ( $^{10,11}\text{C}$ ) produced in the fragmentation of the incoming beam plays an important role. Figure 3.6 shows the comparison between the calculated (solid line) and experimental measured [19] (points) attenuation profile as a function of depth in water for a 400 MeV/n carbon beam. A satisfactory agreement, except in the BP region, has been found. The discrepancies are probably due to the occurring of nuclear reactions before the water target or to the experimental water-equivalent conversion of the materials in the beam-line. In addition it's worth remarking that at this energy only the 30 % of the carbon ions surviving the passage through the water absorber reaching the Bragg peak, while the remaining 70 % undergo nuclear reactions altering considerably the radiation field.

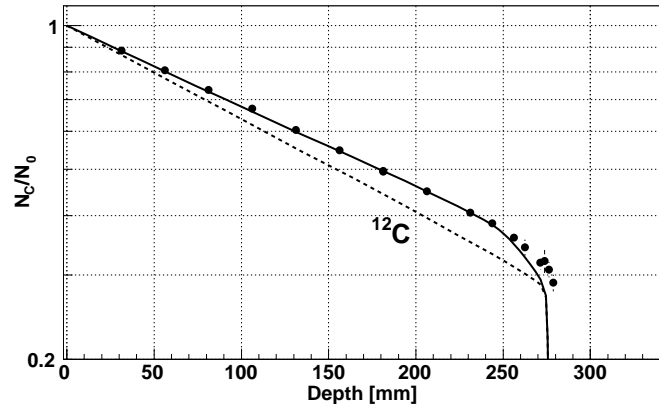


Figure 3.6: Attenuation profile of a 400 MeV/n  $^{12}\text{C}$  beam as a function of depth in water. The experimental data [18,19] (points) are compared with the FLUKA results (solid line).

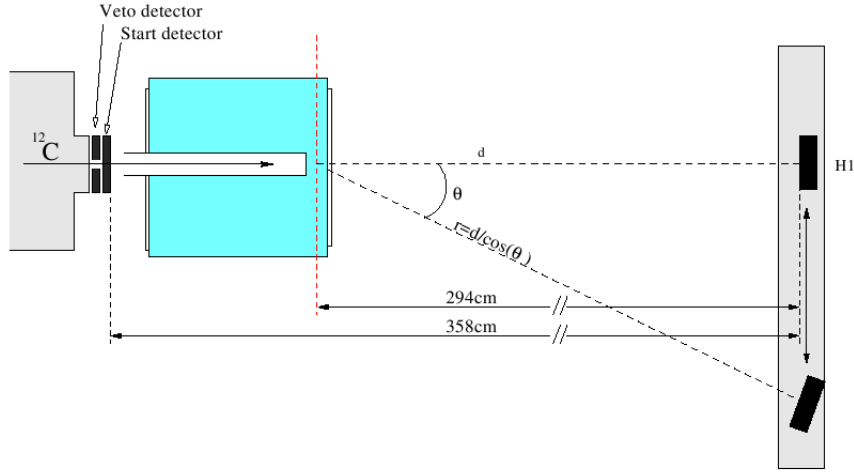


Figure 3.7: Sketch of the experimental setup used for the angular/energy distribution measurements. The target center is indicated by a red line. The measures are not in scale [18].

## 3.4 Characterization of charged fragments

The aim of this section is to outline the mixed field measurements [18, 19] and their Monte Carlo simulations for a 400 MeV/n  $^{12}\text{C}$  beam on water targets. The latter include calculation of the build-up of secondary charged fragments, i.e., the fragment yield as a function of the depth, starting, as in the experimental procedure, from their angular distribution for various water thicknesses corresponding at depths before and behind the measured BP. In addition, some experimental/theoretical energy spectra of few secondary fragments will be presented. In this section only a small set of the simulations done to reproduce the experimental data [18] is reported, the same conclusions could be obtained also for the other calculations not shown here.

### i) Experimental methods

In two experiments performed at GSI [18, 19], angular/energy distributions of charged fragments produced in water were measured by means of time-of-flight (TOF) and energy loss techniques. Similar to the attenuation experiment, the beam exit window was followed by the Start detector and the water target. Behind the target an energy loss detector, H1, was positioned at a distance of approximately 3 m. Figure 3.7 shows a sketch of the experimental setup. The emission angle of the fragment is defined as the angle between the beam axis and H1 detector seen from the target center. The H1 detector was mounted on a linear drive and could be moved to positions ranging from  $-1^\circ$  to  $10^\circ$ . A mechanical construction made the H1 detector to rotate simultaneously with the linear movement of H1 to assure the scintillator always to be perpendicular to the target center. The particles were identified in the standard way plotting energy loss versus TOF. Figure 3.8 is an example of the achieved charge

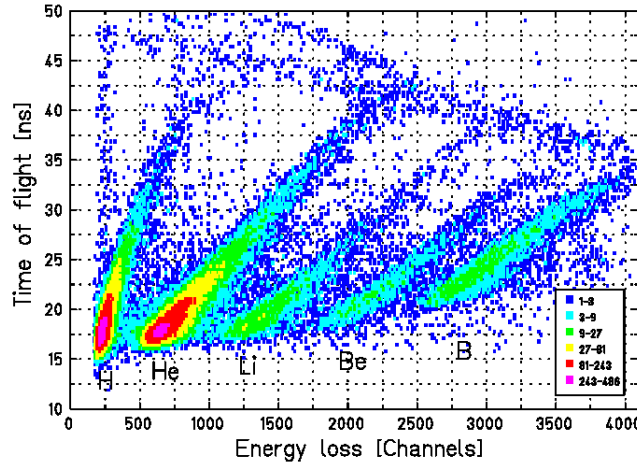


Figure 3.8: Particle identification spectrum obtained at an emission angle of  $2^\circ$ . The data originate from a 400 MeV/n  $^{12}\text{C}$  beam fully stopped in a 28.8 cm thick water target [18].

resolution (see [18] for more details).

#### ii) The simulation approach

For simulating the experiment of E. Haettner, D. Schardt *et al.* with FLUKA, the target was modelled as a single block of water while the detecting system as a half sphere with a radius of approximately 3 m surrounding the target. Special properties of the detector system were not taken into account. Angular and energy spectra of the emitted fragments were scored in the same simulation using the FLUKA ‘USRYIELD’ card [97]. To achieve good statistics, especially for the angular/energy spectra of the less produced fragments, the simulations were run 10 times each for  $2 \times 10^5$  primaries and different random number sequences.

### 3.4.1 Angular distributions

The energy and angular distributions of the escaping secondary fragments were experimentally investigated at seven different lengths of the water absorber corresponding to depths before and behind the BP. Figure 3.9 shows the angular distributions of carbon ions at two depths before the BP ( $27.5 \pm 0.05$  cm). As the thickness of the water absorber increases the angular distribution becomes wider due to the multiple scattering of the surviving primary beam and to the secondary carbon ions generated in nuclear collisions. The FLUKA calculations reproduce satisfactory the experimental data.

Generally, the width of the angular distribution depends on the element. Helium and especially hydrogen have broad distributions and can be detected at angles greater than the experimental limit of  $10^\circ$ . With increasing mass, the distributions become more and more narrow. Such a behavior is reported in Figures 3.10 and 3.11 for fragments escaping a 15.9 cm and 31.2 cm thick water

### 3.4. Characterization of charged fragments

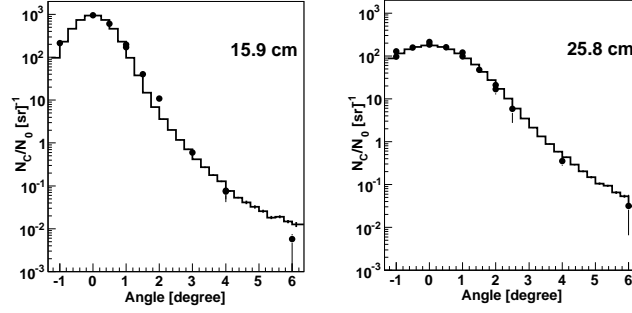


Figure 3.9: Angular distributions of carbon ions behind a 15.9 cm (left panel) and 25.8 cm (right panel) thick water phantom. The points [18] give the experimental data while the histograms represent the FLUKA results.

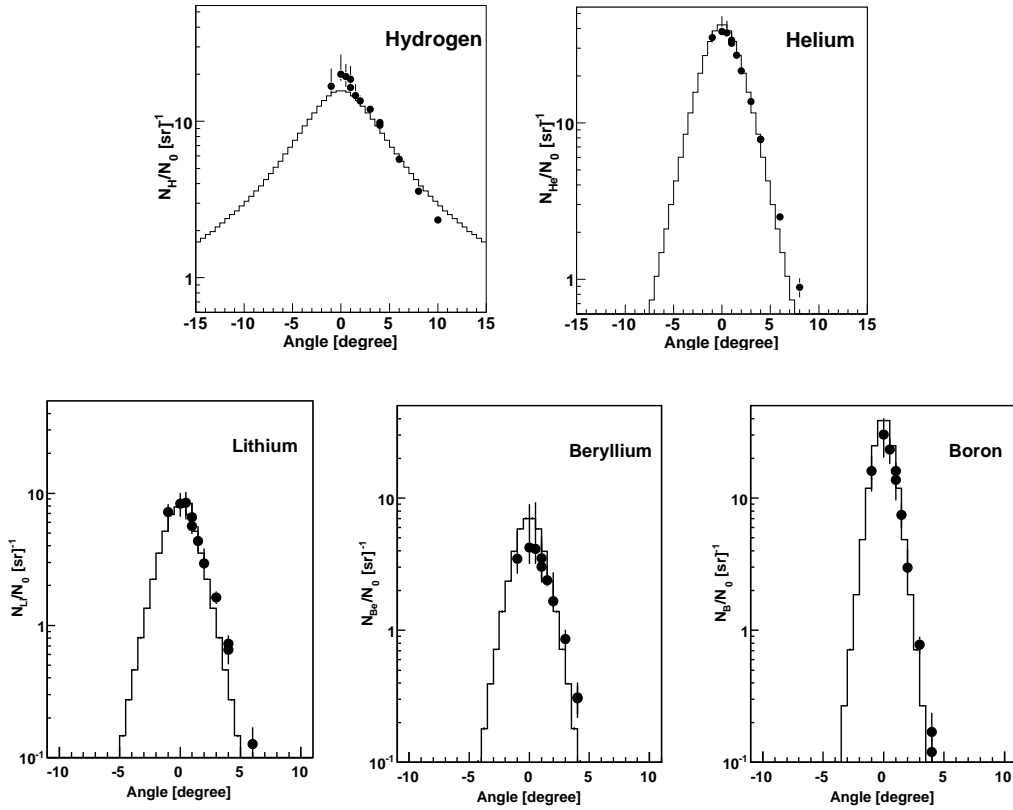


Figure 3.10: Angular distributions of the indicated secondary fragments behind a 15.9 cm thick water phantom. The points [18] give the experimental data while the histograms depict the FLUKA results.

### 3. Investigation of carbon ion fragmentation in water using the FLUKA code

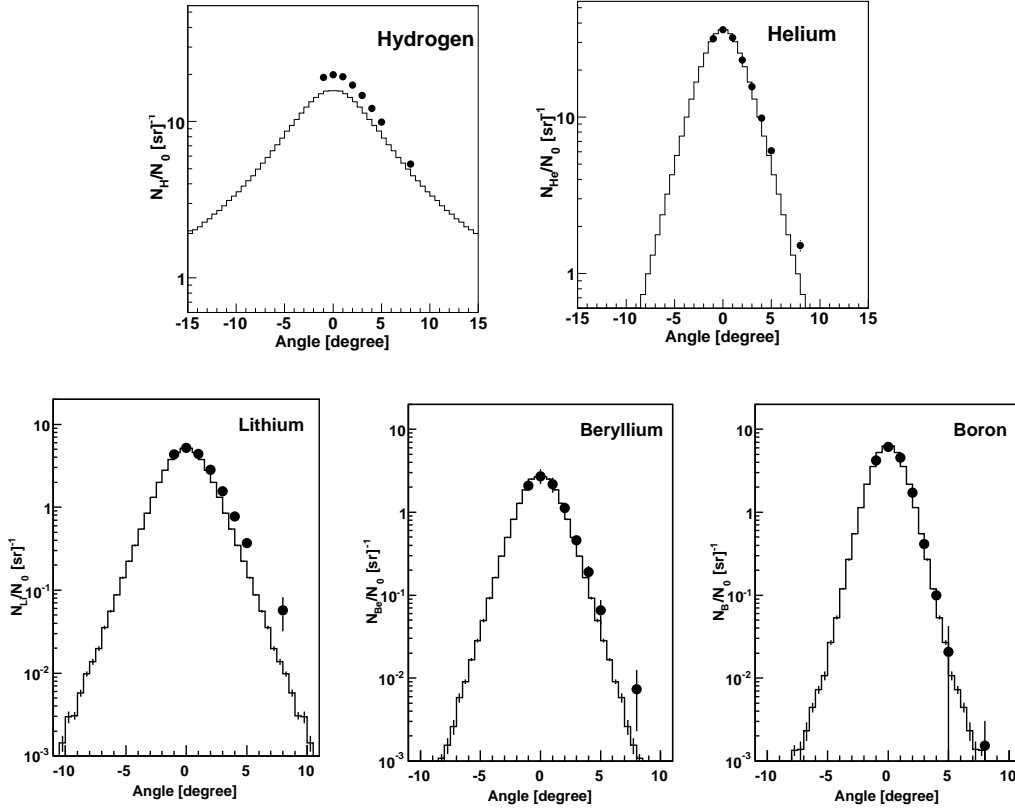


Figure 3.11: Angular distributions of the indicated secondary fragments behind a 31.2 cm thick water phantom. The points [18] give the experimental data while the histograms depict the FLUKA results.

phantom, respectively. In the direction of the beam axis at depths before the BP, the most dominating particle is helium. The second most frequent element detected at 0° is boron, followed by hydrogen and lithium. Behind the BP the fragment spectrum is dominated by H and He fragments while the amount of boron drops rapidly. The lighter fragments show the broadest angular spectra while the heavier ones (Li, Be and B) are emitted in a rather low narrow cone of about 0° to 5°. The Monte Carlo simulations reproduce all these features except for hydrogen where it is evident an underestimation of its yield in the very forward direction. The found discrepancy suggests the necessity of further investigations both in the nucleus-nucleus event generators and in the transport algorithms, since in the simulation of a thick target experiment a lot of effects come into play. Among them, the modelling of the experimental setup could be one of the most critical. However, the obtained results seem to indicate that FLUKA reliably describes the angular distribution of the mixed field before and behind the BP. This is an important aspect in order to estimate the broadening of the irradiation field in therapy applications. In fact due to the possible range uncertainties, in treatment planning a beam just stopping in

### 3.4. Characterization of charged fragments

front of a critical structure is usually avoided. Therefore, tumor volumes close to critical structures can only be irradiated with the beam passing by. How close the beam can get is consequently determined by the lateral scattering, which is therefore relevant for clinical application.

#### 3.4.2 Build-up of charged fragments

The build-up curve describes the particle yield as a function of depth. The yield represents the number of produced fragments per primary  $^{12}\text{C}$  ion. Experimentally, the build-up curves were obtained integrating the angular distributions from  $0^\circ$  to  $10^\circ$  [18]. The experimental data were fitted with a Gaussian function for small angles and with an exponential function for larger angles. In the case of heavy fragments, from lithium up to boron, the integration gives, due to their narrow angular distributions, the total number of secondary particles produced per incident carbon ion. On the contrary, for hydrogen and helium, the integration gives their yield in the experimental angular window because they are spread at angles greater than  $10^\circ$ . The build-up curves of secondary charged fragments produced by the irradiation of a water phantom with a 400

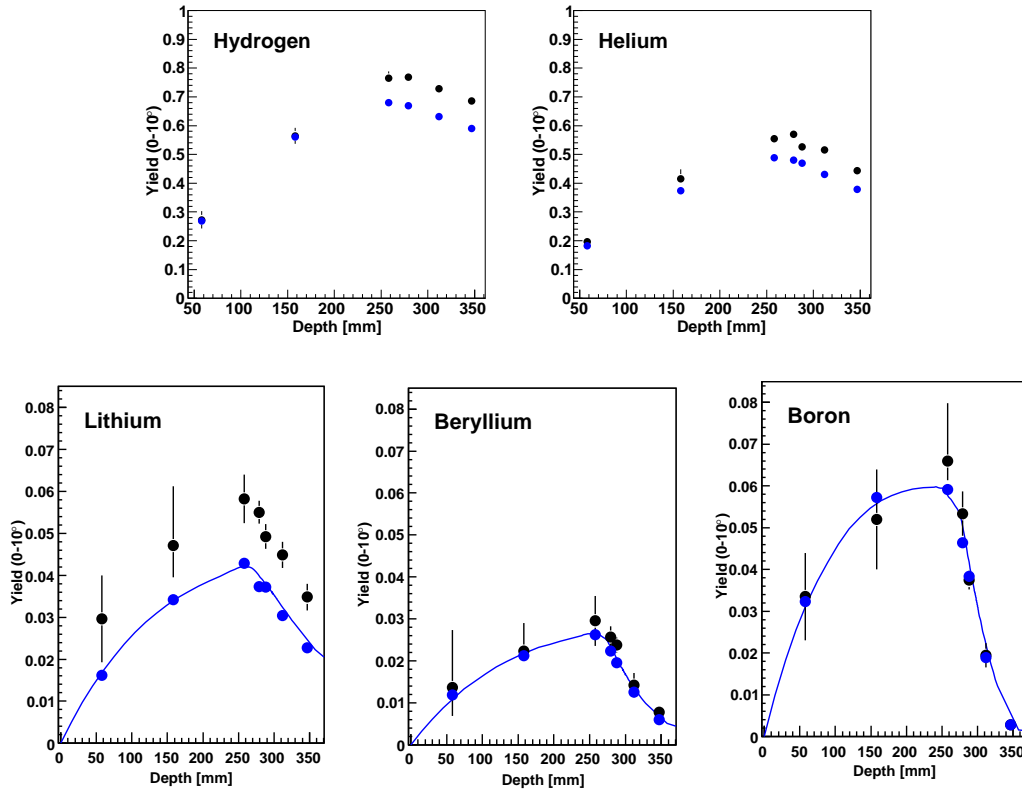


Figure 3.12: Build-up curves of the indicated charged fragments. The black points give the experimental data [18, 19] while the blue points together with the blue lines (see the text for more details) depict the FLUKA results.

MeV/n carbon beam are shown in Figure 3.12. The amount of charged fragments increases with increasing depth reaching a maximum around the BP. Behind the BP the amount of fragments drops since all primary carbon ions have stopped and cannot produce new fragments. Light fragments, such as hydrogen and helium, can still be produced from nuclear interactions of heavier fragments.

In order to obtain the build-up curves two simulation approaches were followed. One was to integrate numerically the angular distributions of all the charged fragments running seven individual simulations with water phantoms of variable lengths. These calculations are reported as blue points in Figure 3.12. The other was to perform only one simulation, where the number of charged ions was registered at different positions in the water phantom and at the end of the simulation a nearly continuous attenuation curve is obtained by normalizing with the number of simulated histories (blue lines in Figure 3.12). However, this method cannot be easily used for light fragments due to the fact that they are also spread outside the experimental angular window. The production of fragments, especially for increasing difference of charge from the primary beam, though reasonably reproduced by the MC simulations, still demands refinements of the FLUKA modelling both in the RQMD [17] and BME (Chapter 2) event generators.

#### 3.4.3 Energy spectra

Another important result of the experiments performed at GSI by E. Haettner, D. Schardt *et al.* [18, 19], was the determination of the energy spectra of the secondary fragments. These are obtained measuring TOF between the Start and the H1 detector. The TOF data represent a measurement of the velocity of a particle, closely related to its kinetic energy. The total energy of a relativistic particle is given by the well-known equation:

$$E_{total} = m_0c^2 + E_{kinetic} = \gamma m_0c^2 \quad (3.1)$$

while the kinetic energy is given by:

$$E_{kinetic} = (\gamma - 1)m_0c^2 = \left(\frac{1}{\sqrt{1 - \beta^2}} - 1\right)m_0c^2 \quad (3.2)$$

where  $\beta c$  and  $m_0$  are, respectively, the velocity and the rest mass of the particle. Eq. 3.2 shows that the kinetic energy is easily obtainable if the velocity is known. In order to calculate the velocity of the fragments, experimentally it has been assumed that all the interactions take place in the target center. Hence, the measured  $TOF_{total}$ , between the Start and energy loss detector, H1, is the sum of the time needed for a primary carbon ion to reach the interaction point (the center of the target),  $TOF_C$ , and time needed by the produced fragment to reach the H1 detector,  $TOF_{frag}$ . The time  $TOF_C$  has been calculated with



### 3.4. Characterization of charged fragments

---

a dedicated code [111–113] taking into account all the materials in the beam-line. Moreover, the velocity is calculated as  $\frac{r}{TOF_{frag}}$  where  $r$  is the distance between the target center and the energy loss detector.

The calculation of energy depends mainly on the finite time resolution and two assumptions. In fact, using the TOF technique the energy resolution is associated to the resolution in time which is originated from the electronics. After measuring the TOF spectrum of a  $^{12}\text{C}$  beam without any target, it has been estimated as the full width half maximum of the measured peak,  $\Delta t_{FWHM}=0.53$  ns [18]. The first assumption was indeed, as already mentioned, that all fragments are produced in the target center while the second one was that the velocity at the target exit can be calculated as the mean velocity between the target center and H1 detector. This latter represents the true velocity for a point somewhere between the target center and the H1 detector. This method neglects the energy loss suffered by fragments between the target center and the H1 detector. These assumptions could influence the experimental data and this fact has to be taken into account when the simulated spectra are compared with the experimental ones. Additional considerations about the experimental procedure and the related errors can be found in [18].

Now, we present the energy spectra calculated scoring directly the kinetic energy of the fragments. The detector has been modelled as a half sphere with a radius of approximately 3 m surrounding the target. Examples of such spectra are shown in Figures 3.13 to 3.16. The overall comparison with the data shows that FLUKA reasonably predicts the energy spectra. However, for hydrogen the MC results underestimate the yield especially at the most forward angles, as already pointed out for the angular distributions. Conversely, for He and Li differences between simulated and experimental spectra increase as the emission angle increases. Furthermore, for the boron spectra, it is clear that the simulated spectra are shifted to lower energies with respect to the experimental ones. Probably, the experimental assumptions play an important role in this case.

The described results represent only a first step in comparing our simulations with the experimental data of energy spectra. In fact, future simulations taking into account the exact description of the irradiated geometry and the experimental procedure are planned in collaboration with K. Parodi and S. Brons (HIT). In particular, we would like to reconstruct the fragment energy starting from the TOF spectra according to the experimental assumptions.

### 3. Investigation of carbon ion fragmentation in water using the FLUKA code

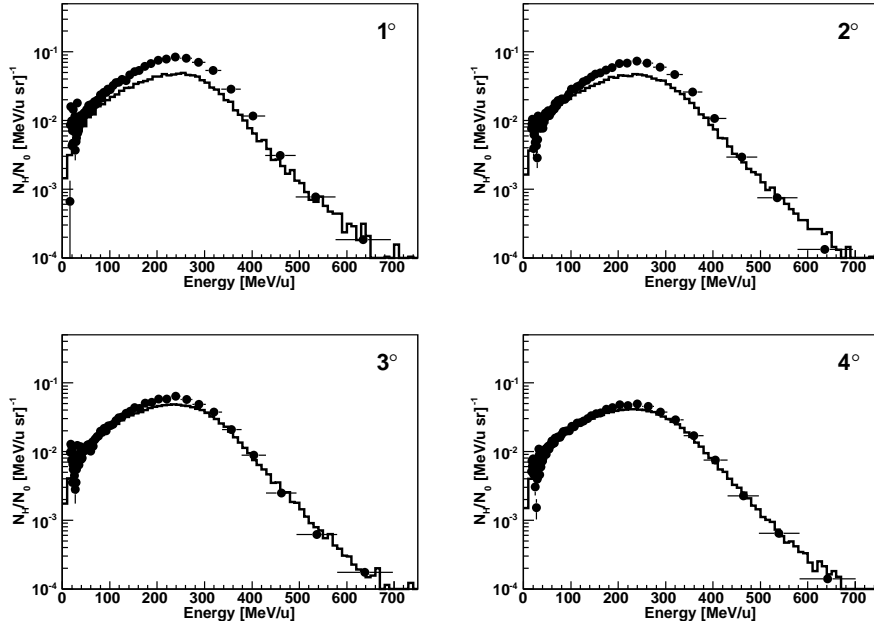


Figure 3.13: Energy spectra of H fragments behind a 31.2 cm thick water phantom. The points [18] give the experimental data while the histograms represent the FLUKA results.

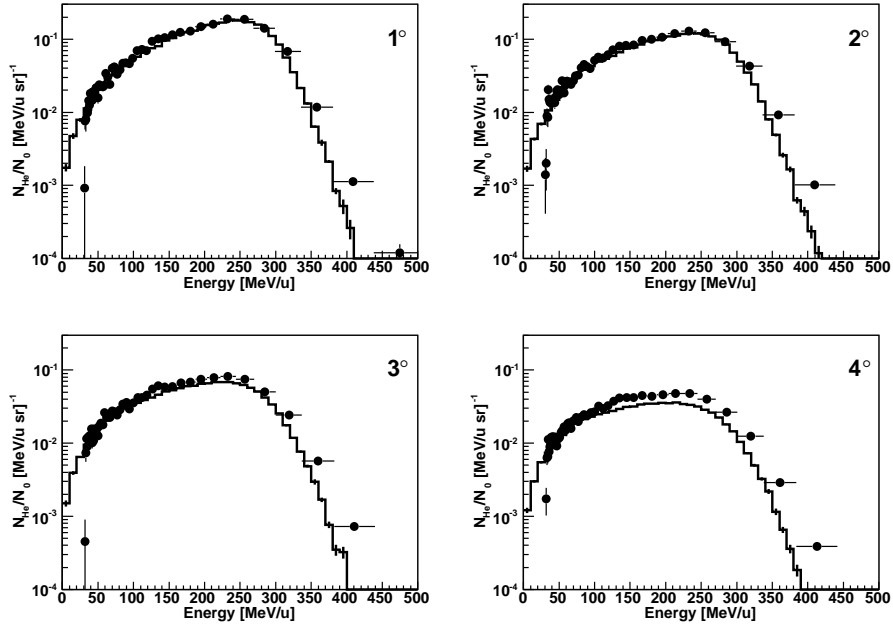


Figure 3.14: Energy spectra of He fragments behind a 28.8 cm thick water phantom. The points [18] give the experimental data while the histograms represent the FLUKA results.

### 3.4. Characterization of charged fragments

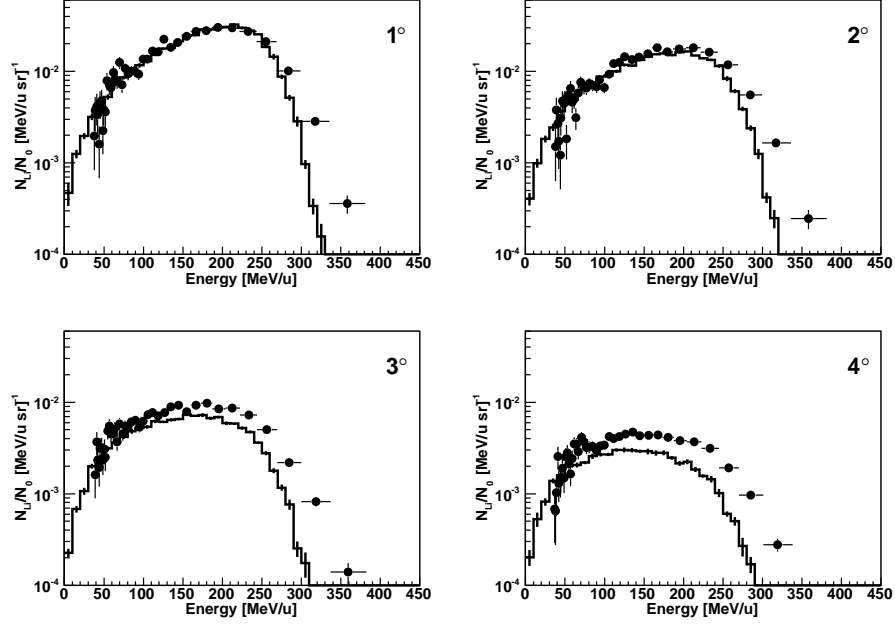


Figure 3.15: Energy spectra of Li fragments behind a 28.8 cm thick water phantom. The points [18] give the experimental data while the histograms represent the FLUKA results.

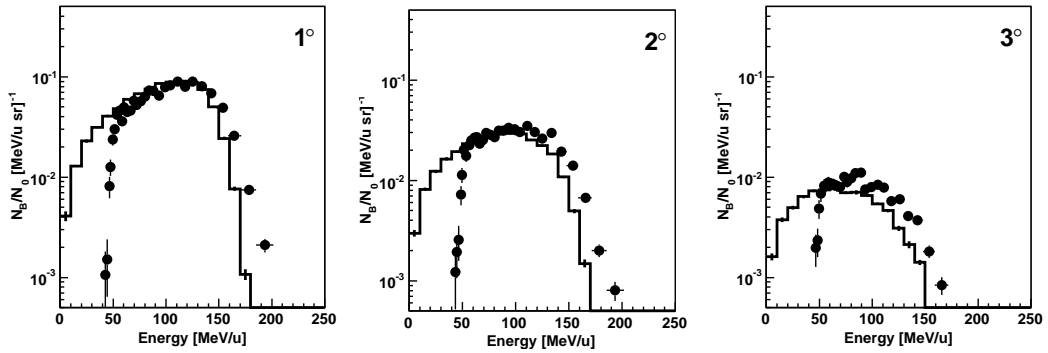


Figure 3.16: Energy spectra of B fragments behind a 28.8 cm thick water phantom. The points [18] give the experimental data while the histograms represent the FLUKA results.

### 3. Investigation of carbon ion fragmentation in water using the FLUKA code

---

# Clinical CT-based calculations of dose in carbon ion therapy using the FLUKA code

## 4.1 Introduction

Nowadays, dedicated or commercial treatment planning systems (TPSs) for ion therapy are essentially analytical codes based on fast performing pencil-beam algorithms. However, Monte Carlo (MC) statistical methods are increasingly considered powerful tools for accurate calculations of dose deposition. They are assumed to provide a more realistic representation of the physical interactions, especially the nuclear ones, undergone by the primary beam and the resulting secondaries. Moreover, MC methods include naturally mixed field capabilities and three dimensional spread of the particle fluence. Although the long computing time prevents, at the moment, their use in clinical routine, MC tools can be very useful for verification, and in certain cases improvement, of the dose calculations performed by the analytical treatment planning engines. In fact, they allow the dose evaluation for every real situation, taking into account the realistic patient anatomy instead of the water-equivalent approach, and for all the cases in which the experimental dosimetric verification is impossible. MC codes can be particularly advantageous in situations sensitive to lateral scattering (especially for protons), nuclear reactions (especially for heavier ions), and in the presence of large inhomogeneities, e.g., due to metallic implants [12]. Furthermore, MC simulations can provide accurate physical databases to be input into TPSs.

In case of proton therapy, dose calculations in clinical CT-patient environment have been already performed using the MC codes GEANT4 [11] and FLUKA [12, 13]. In this work, for the first time, clinical CT-based calculations of dose for carbon ion therapy applications are carried out using the FLUKA code thanks to its reliable nucleus-nucleus event generators in the en-

ergy range of therapeutic relevance. Nucleus-nucleus interactions at energies ranging from the Coulomb barrier up to 100 MeV/n could now be treated using the new BME event generator (Chapter 2) extending the previous FLUKA energy range for nuclear reactions. The MC simulations are compared with the results of the analytical code TRiP (TReatment planning for Particle) which is the production version (1998) of the treatment planning used in every day clinical experience at GSI [7–9]. In general, MC dose distributions are found in good agreement with the analytical calculations, except in the distal part due to the different fragmentation tails and in presence of air/tissue interfaces.

The TRiP code is in clinical use since the start of the GSI pilot project in December 1997. It is designed to cooperate with the GSI three-dimensional active dose shaping device, the raster scan system [32]. This beam delivery system allows to select any combination from a list of 253 individual beam energies, 7 different beam spot sizes and 15 intensity levels. Inverse planning techniques, which are out of the scope of this work, are implemented in order to obtain a uniform target dose distribution from clinical input data, i.e., CT images and patient contours. This implies the automatic generation of intensity modulated fields in terms of beam position, energy and particle fluence. This set of data is directly passed to the beam delivery and control system.

The chapter is organized as follows: in Section 4.2 the TRiP code (for more details [7]) is briefly described whereas the last section is devoted to the work done in order to perform clinical calculations of dose in the CT environment using the FLUKA code. The latter implies the implementation of the GSI delivery system and its validation against experimental data, the handling of CT images and the simulation, as an example, of a clinical cranial plan.

## 4.2 Analytical treatment planning for ion therapy: TRiP

The GSI facility (Darmstadt, Germany) realized for the first time the combination of active field shaping, using a scanned beam via magnetic deflection [32], with active energy variation of the beam, thus making full use of the advantages of heavy charged particles for therapy. Due to the mentioned technique and strong dependence of the RBE on the particle charge, energy and absorbed dose (Chapter 1), the GSI group developed an inverse treatment planning code, TRiP, completely different from the software generally used in conventional radiotherapy. Like in conventional radiotherapy, TRiP uses input diagnostic information from computer tomography (CT) and magnetic resonance (MR) images to model the volume to be irradiated; the CT data are mandatory for dose computation and optimization.

In order to describe the ion interaction with tissue, the GSI group developed an analytical model able to calculate the distribution of primary and secondary particles and their energies as a function of depth [7]. In TRiP, the

## 4.2. Analytical treatment planning for ion therapy: TRiP

---

multiple Coulomb scattering of the beam and of the secondary fragments is neglected. In addition, all the other particles which might be generated during  $^{12}\text{C}$  slowing down such as  $\gamma$ -rays and  $\delta$ -rays are neglected because they make only a small contribution to the dose (compared with the primary  $^{12}\text{C}$ ) or because they are already included in the energy loss (low energy  $\delta$  electrons). Following these assumptions, the partial dose generated by a single ion beam with energy  $E_{beam}$  is described in TRiP as

$$D(E_{beam}, \vec{x})[Gy] = Cd(E_{beam}, z) \left[ \frac{MeV}{g \cdot cm^{-2}} \right] \frac{N}{2\pi\sigma^2[mm^2]} \exp\left(-\frac{r^2}{2\sigma^2}\right) \quad (4.1)$$

where  $r$  is the distance from the beam center,  $\sigma$  is the actual variance of the Gaussian beam profile and  $N$  is the total number of particles. The lateral beam profile is assumed to be Gaussian in shape and symmetric in  $x$  and  $y$ .  $d(E_{beam}, z)$  is the energy loss distribution, for a given initial beam energy,  $E_{beam}$ , as a function of the penetration depth,  $z$ , in water or water-equivalent material. It is described by a dedicated model, the YIELD transport model [7], that takes into account not only the single particle energy loss but also the energy loss straggling and the projectile fragmentation. YIELD transports the primary beam and the generated secondary particles only in one dimension.

The irradiated target under consideration is divided into approximately 80 slices with variable thickness in order to have a finer grid in the Bragg peak region and a wider one in the entrance region where the irradiation field changes slowly. For each slice, energy spectra  $dN(E_{beam}, z, T, E)/dE$  for ingoing (index I) and outgoing (index F) particles are defined, where T represents a particular particle species defined by the nuclear charge  $Z$  and the mass number  $A$ . Within each of these material slices of varying thickness  $\Delta z_i$ , new particles can be created by fragmentation of the ingoing ones:

$$\begin{aligned} \frac{dN_F}{dE_F}(T_F, E_F) = \sum_{T_I, E_I} \frac{dN_I}{dE_I}(T_I, E_I) [1 - \exp(-\Delta z \sigma_{I \rightarrow F}(T_I, E_I) n_{nuclei})] \\ \times \exp\left(-\frac{1}{2} \frac{(E_F - \langle E(E_I, E'_I) \rangle)^2}{\langle \sigma^2(E_I, E'_I) \rangle}\right) \end{aligned} \quad (4.2)$$

where  $\sigma_{I \rightarrow F}(T_I, E_I)$  is the cross section for the production of a fragment species  $T_F$  from its parent species  $T_I$  by nuclear fragmentation reactions. These cross sections are derived from semi-empirical formulations [114, 115].  $n_{nuclei}$  is the number density of nuclei. The values  $\langle E \rangle$  and  $\langle \sigma^2 \rangle$  are the mean energy and the mean energy variance after momentum loss by fragmentation [116], with  $E'_I = E_I - dE/dx(T_I, E_I)\Delta z$ ; the energy loss  $dE/dx(T, E)$  is interpolated from tables proposed in [117]. Simultaneously the ingoing particle spectrum is transformed by attenuation, energy loss and energy straggling:

$$\begin{aligned} \frac{dN_F}{dE_F}(T_F, E_F) = \sum_{E_I} \frac{dN_I}{dE_I}(T_I = T_F, E_I) \exp(-\Delta z \sigma_{att}(T_I, E_I) n_{nuclei}) \\ \times \exp\left(-\frac{1}{2} \frac{(E_F - \langle E(E_I) \rangle)^2}{\langle \sigma^2(E_I) \rangle}\right) \end{aligned} \quad (4.3)$$

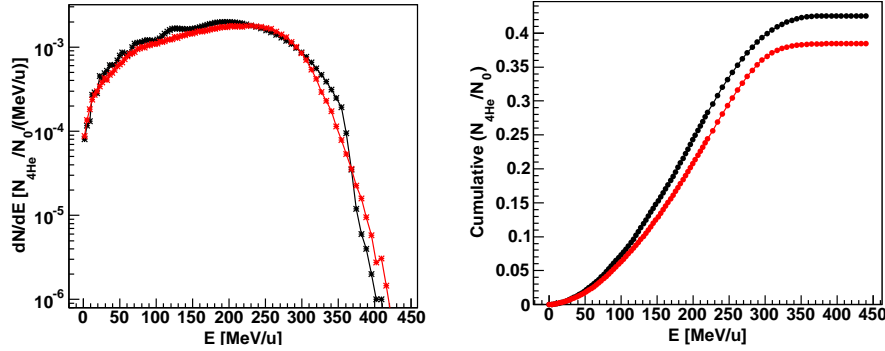


Figure 4.1: Energy spectrum (left panel) and its cumulative distribution (right panel), as a function of kinetic energy, for  $^4\text{He}$  particles produced by a 400 MeV/n carbon beam at about 29 cm in water. The energy spread  $\Delta E/E$  of the beam is 0.04 %. The black and red lines give, respectively, the TRiPbeam, status of May 2006, (*courtesy of M. Krämer, GSI, Darmstadt, and K. Parodi and S. Brons, HIT, Heidelberg*) and the FLUKA results.

where  $\sigma_{att}$  is the empirically corrected total reaction cross section. The values  $\langle E \rangle$  and  $\langle \sigma^2 \rangle$  are the mean energy and the mean energy loss straggling, respectively, after electronic energy loss within the slice under consideration. After the calculation for one slice is completed the *outgoing* spectrum becomes *ingoing* spectrum for the next slice, finally the depth dose distribution is derived:

$$d(E_{beam}, z) = \sum_T \int_E dE \frac{dN}{dE}(E_{beam}, z, T, E) \frac{dE}{\rho dx}(T, E) . \quad (4.4)$$

For practical use in therapy planning, the depth dose profiles are pre-calculated once in steps of 10 MeV/n (in term of initial beam energy) from 50 to 500 MeV/n and then stored as tables. The fragment spectra  $dN(E_{beam}, z, T, E)/dE$  for each depth are stored as well, in order to carry out biological effect calculations. As an example, the  $dN(E_{beam}, z, T, E)/dE$  spectrum for alpha particles produced by a 400 MeV/n carbon beam at about 29 cm in water is reported in Figure 4.1 (left panel) together with its cumulative distribution (right panel). By the cumulative distribution the TRiP code samples the number of particles per incident carbon beam produced at different energies. Moreover, the secondary fragments build-up and the primary beam attenuation profiles, as a function of depth, are obtained integrating the  $dN(E_{beam}, z, T, E)/dE$  spectra. In Figure 4.2 are reported such profiles for He (left panel) and carbon ions (right panel). The analytical calculations refer to the TRiPbeam code which is a development version of TRiP. Whereas the FLUKA results are obtained using a development version of the official release (*fluka2006.3b*) which includes the FLUKA-BME interface in order to treat nucleus-nucleus reactions at low energies (Chapter 2). The  $dN(E_{beam}, z, T, E)/dE$  spectra obtained with FLUKA are saved in the same format of TRiP to be input into TPSs, thus to



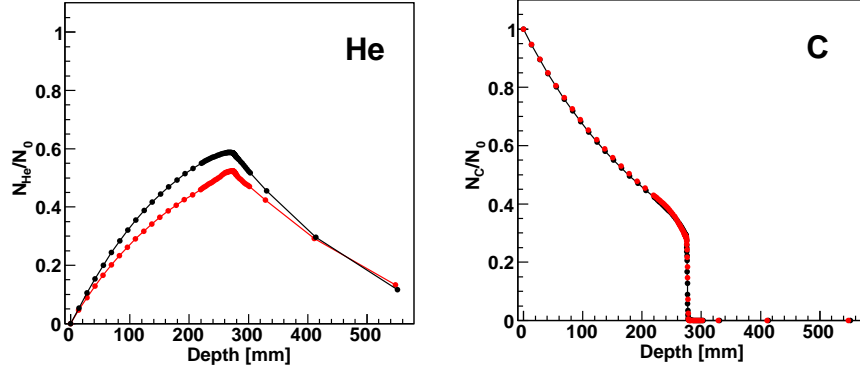


Figure 4.2: Build-up of He fragments (left panel) and attenuation of the carbon beam (right panel) as a function of depth in water. The  $^{12}\text{C}$  beam energy is 400 MeV/n with  $\Delta E/E = 0.04\%$ . The black and red lines give, respectively, the TRiPbeam, status of May 2006, (*courtesy of M. Krämer, GSI, Darmstadt, and K. Parodi and S. Brons, HIT, Heidelberg*) and the FLUKA results.

understand the effect of a different treatment of nuclear reactions on physical and biological dose calculations. Future studies on this hybrid solution are planned in collaboration with K. Parodi and S. Brons (HIT, Heidelberg).

As previously mentioned, the GSI facility uses a three-dimensional active dose shaping device. The only passive (static) shaping element is the so-called ripple filter [118]. This element was introduced to broad the Bragg peaks especially at low beam energies. In fact, at beam energies below about 150 MeV/n the unmodified Bragg peaks become very sharp ( $\approx 1$  mm FWHM in water at 100 MeV/n), so many energy slices would be needed to deliver a homogeneous dose distribution increasing the treatment time. In TRiP the ripple filter is taken into account through its transmission function which is described as a set of different Bragg peak displacements,  $\Delta z_i$ , caused by different beam traversal paths occurring with probabilities  $w_i$ . In presence of the ripple filter, the depth dose profiles (Eq. 4.4) and the spectral distributions  $dN(E_{beam}, z, T, E)/dE$  become:

$$\begin{aligned}
 d'(E_{beam}, z) &= \sum_i d(E_{beam}, z + \Delta z_i) w_i \\
 \frac{dN'}{dE}(E_{beam}, z, T, E) &= \sum_i \frac{dN}{dE}(E_{beam}, z + \Delta z_i, T, E) w_i \\
 \sum_i w_i &= 1
 \end{aligned} \tag{4.5}$$

All dose and optimization algorithms remain unchanged, only the databases are chosen differently with and without the ripple filter. On the contrary for MC simulations, the ripple filter has been implemented in the FLUKA geometry reproducing the real clinical/experimental setup [119].

The TRiP algorithms described till now are based on the assumption of water targets while the patient tissue is inhomogeneous with regions of various densities like water, bone, muscle, fat, air cavity and so on. The basic idea to account for such density variations into the TRiP code is to apply the concept of water-equivalent path length (WEPL) as it will be described in the Section 4.3.2.

For dose optimization the one-dimensional dose distributions  $d(E_{beam}, z)$  are used because the lateral beam scattering is negligible compared with the initial beam width as delivered by the beam optics [7]. Following this assumption, Eq. 4.1 becomes

$$D(E_{beam}, \vec{x})[Gy] = Cd(E_{beam}, z) \left[ \frac{MeV}{g \cdot cm^{-2}} \right] F(E_{beam}, x, y)[mm^{-2}] \quad (4.6)$$

with the fluence

$$F(E_{beam}, x, y) = \frac{N(E_{beam}, x, y)}{\Delta x \Delta y} \quad (4.7)$$

where  $\Delta x$  and  $\Delta y$  are the scanner step sizes in  $x$  and  $y$  respectively. This crude approximation, a Gaussian profile in term of a delta function, is sufficiently accurate if the lateral scanning steps are chosen as a small fraction of the beam width

$$\Delta x = \Delta y \leq f_F \times FWHM \quad (4.8)$$

where for  $f_F$  is empirically adopted a value of 1/3. With the scanner positions chosen in this way, the dose  $D(\vec{x})$  is calculated as a superposition of many elementary beams:

$$D(\vec{x}) = \sum_{E_{beam}} d(E_{beam}, \vec{x}) . \quad (4.9)$$

At this point TRiP uses sophisticated optimization procedures in order to calculate the optimum set of accelerator energies  $E_{beam}$  to cover the whole depth range and for each energy and scanner position the corresponding particles  $N(E_{beam}, x, y)$  to achieve the prescribed dose. This optimization is performed in the water-equivalent system (see [7] for more details) and only a single field (beam port) is optimized at a time. After single-field optimization in the water-equivalent system the dose distribution is calculated in the CT system. Extension of the TRiP capabilities to include multiple Coulomb scattering and multi-field optimization are underway in the mentioned TRiPbeam development version.

## 4.3 Monte Carlo calculations of dose in carbon ion therapy

### 4.3.1 The GSI beam delivery system

This section briefly outlines the beam delivery system for radiotherapy at GSI and how it has been coded in FLUKA. The general design idea of the GSI group was to use completely active volume scanning in three dimensions. This is achieved by magnetic deflection of the  $^{12}\text{C}$  beam in the lateral direction [32] and by energy variation of the GSI synchrotron to cover different depths spreading out the dose across the target volume. The magnetic scanning system deflects the ion beam in the lateral  $(x,y)$  direction across a maximum field size of  $200 \times 200 \text{ mm}^2$ . The GSI SIS accelerator provides ion beams from protons to uranium with energies up to 2 GeV/n for lighter ions ( $\approx 1 \text{ GeV/n}$  for uranium). In order to match the needs of radiotherapy, the accelerator control system was modified to allow selection of energy, spot size and intensity level of the beam from one synchrotron cycle to the next [120]. A list of 253 energies has been set up, ranging from 80 MeV/n to 430 MeV/n, in order to achieve a constant spacing of the corresponding ranges in water, 20 mm and 330 mm respectively. The ion energy can be switched within  $\approx 5 \text{ s}$  and thus different depths can be reached without the need of additional absorbers. The target region is divided into subsequent slices corresponding to beams of different energies. The nominal beam spot diameter can be chosen from a predefined list; narrow beams are used for small volumes and in situations where sharp dose gradients at the field boundary are required, while larger ones are preferred for large target volumes because they reduce the number of scanning steps needed to cover such volumes. The beam profile is approximately symmetric and Gaussian shaped; the most common spot size setting is 5 to 6 mm FWHM, yielding a lateral dose fall-off (from 90% to 10%) of the same magnitude.

The main input to the control system are the particle fluences  $F(E_{\text{beam}}, x, y)$  obtained, as mentioned in Section 4.2, from the TPS optimization. The particle fluences for each energy and position are monitored in order to verify the correct delivery of the prescribed dose. This is achieved by a set of transmission ionization chambers (ICs) [121] which are calibrated against a standard dosimeter every morning as part of the daily checks. These monitors and the air between the beam outlet and the patient, which are not part of the CT plan, are taken into account into the treatment planning calculations adding an extra water-equivalent offset. Its value, experimentally determined, is equal to 1.709 mm. In the FLUKA geometry a layer of water with the same thickness of the offset is included; a detail description of the ICs is not needed because the nuclear reactions undergone by the primary beam in these materials are negligible.

Irradiation times for typical cases are of the order of few minutes. Large tumors of some hundred cubic centimetres in volume may require about 20

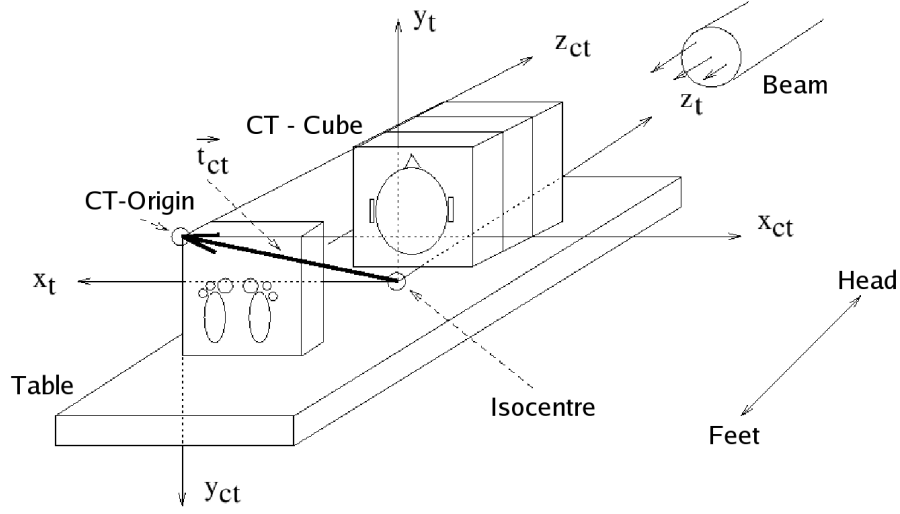


Figure 4.3: Patient CT and table systems [122].

minutes treatment time. In the treatment room there is only a fixed horizontal beam line. However, the patient couch can be rotated, so that multi-field irradiation is possible, at least in a single plane. Most patients are treated with two approximately opposing fields.

As result of the treatment planning optimization, TRiP produces a data file, the raster scan file ('rst-file'), directly passed to the beam delivery and control system. It contains, among the others, the following information:

- the particle beam species defined by the nuclear charge  $Z$  and the mass number  $A$ ;
- the ripple filter used;
- the *gantry angle*;
- the *couch angle*;
- the number of beam energies used to irradiated the target volume and for each beam energy and position the particle fluence  $N(E_{beam}, x, y)$ .

While  $N(E_{beam}, x, y)$  refers to the raster scan system (RST), the dose calculations are performed in the patient CT system, the necessary transformations from one system to the other are described in detail in [122]. Briefly, the RST system ( $\vec{r}_s$ ) differs from the treatment room system ( $\vec{r}_r$ ) by a rotation along the  $x_r$  axis while the patient table system ( $\vec{r}_t$ ) differs from the treatment room system by a rotation along the  $y_r$  axis:

$$\begin{aligned}\vec{r}_s &= R_x(-\Theta_S)\vec{r}_r \\ \vec{r}_r &= R_y(-\Theta_T)\vec{r}_t\end{aligned}$$

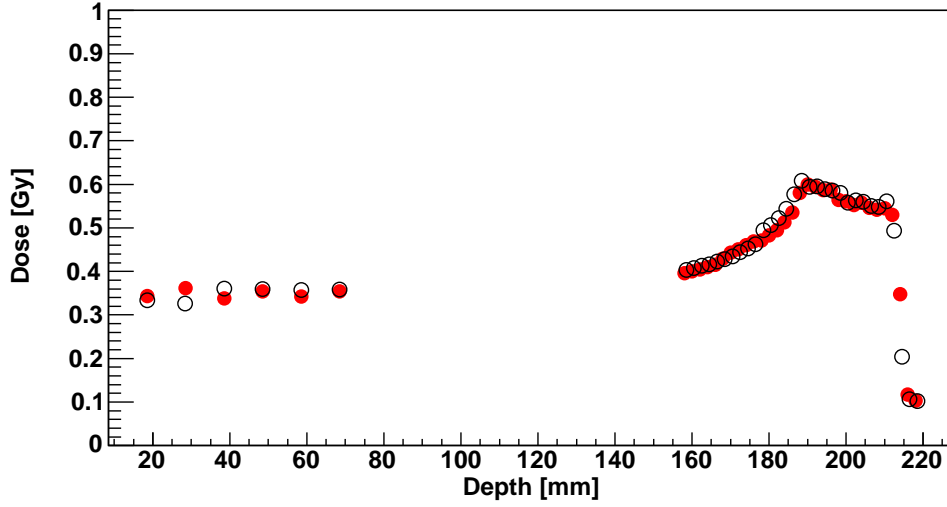


Figure 4.4: Spread-out Bragg peak in water. The experimental data, red full circles (*courtesy of K. Parodi and S. Brons*), are compared with the FLUKA results, black open circles.

where  $\Theta_S$  and  $\Theta_T$  are the *gantry angle* (usually equal to  $-2.203^\circ$ ) and the *couch angle*, respectively. To move from the CT system ( $\vec{r}_{CT}$ ) to the table system (Figure 4.3) is needed a rotation of  $180^\circ$  along the  $z_t$  axis together with a translation of  $\vec{t}_{CT}$  between the origin of the CT and the isocentre:

$$\vec{r}_t = T(\vec{t}_{CT})R_z^{-1}(180^\circ)\vec{r}_{CT} . \quad (4.10)$$

Putting things together the transformation from the RST system to the CT system becomes:

$$\vec{r}_s = R_x(-\Theta_S)R_y(-\Theta_T)T(\vec{t}_{CT})R_z^{-1}(180^\circ)\vec{r}_{CT} . \quad (4.11)$$

For MC simulations, the user oriented program ‘source.f’ included in the FLUKA distribution has been customized in order to perform dose calculations in the CT system starting from the particle fluences  $N(E_{beam}, x, y)$  (*courtesy of F. Sommerer, CERN*). At the initialization stage, the code reads the ‘rst-file’ and makes the necessary transformations from the RST system to the CT system where the phantom/patient geometry is coded. Energy, position and cosinus directors of the primary beams are randomly chosen according to  $N(E_{beam}, x, y)$ . For reasonable computation times, only a fraction of the particles are simulated therefore the resulting energy deposition is only a fraction of the planned dose. At the end of the simulation the results are rescaled to the dose prescription using a factor given by the ratio between the total number of primary carbon ions (as reported in the ‘rst-file’) and FLUKA simulated one. Using the described ‘source.f’ code and implementing in the FLUKA geometry the experimental setup (the ripple filter, the target phantom etc.) we are able

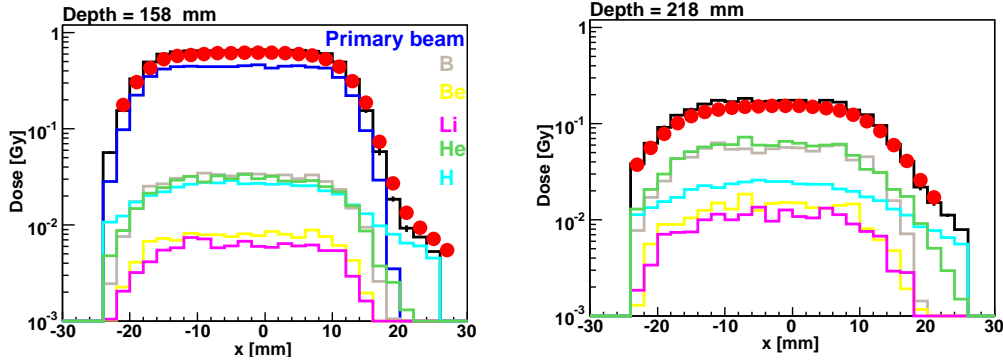


Figure 4.5: Lateral profiles of the SOBP of Figure 4.4. The experimental data, red full circles (*courtesy of K. Parodi and S. Bruns*), are compared with the FLUKA results, black histograms. The coloured histograms refer to the energy deposition by the indicated ions.

to perform three-dimensional dose calculations in water in the same way that the GSI radiotherapy facility experimentally does. On the contrary to simulate a clinical patient plan, we need one more step, the processing of CT images as it will be described in Section 4.3.2.

Figure 4.4 shows the comparison between a measured and simulated one-dimensional spread-out Bragg peak (SOBP) in water. The satisfactory agreement permits to state that the GSI irradiation setup has been correctly implemented and the FLUKA code is a valuable choice among the other MC codes to perform this kind of calculations. In addition Figure 4.5 shows a nice comparison between the calculated and measured lateral dose profiles at depths before and beyond the SOBP of Figure 4.4. At 158 mm depth the main contribution to the dose is due to the energy deposition by the primary beam. The secondary fragments, especially the lighter ones such H and He, broaden the lateral dose profiles. This is more clear beyond the SOBP (Figure 4.5 - right panel) where the total dose is the sum of the energy deposition only by the secondary fragments. In general, the nuclear reactions tend to deteriorate the sharp dose contours by enhanced lateral and longitudinal scattering. The treatment planning has to take into account these effects because in the clinical application beams directly stopping in front of a critical structure are avoided due to possible range uncertainties. Therefore, tumor volumes close to critical structures are typically irradiated with the beam passing by and how close the beam can get is consequently determined by the lateral scattering especially of secondary fragments.

### 4.3.2 CT handling

Treatment planning for ion beams uses, like conventional planning, diagnostic images such as MR and CT to generate a digital model of the irradiation region. While MR images deliver high-resolution information on tumor location

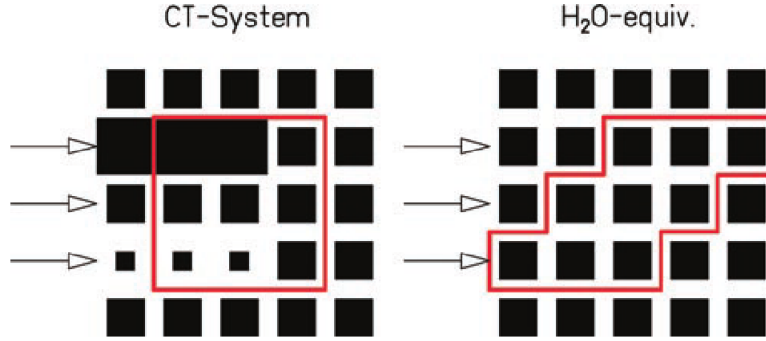


Figure 4.6: Transformation from CT into water equivalent system [7].

and critical structures, the CT data are mandatory for dose computation. CT data are usually expressed in terms of HU (Hounsfield unit):

$$HU = \left( \frac{\bar{\mu}}{\bar{\mu}_{H_2O}} - 1 \right) \cdot 1000 \quad (4.12)$$

where  $\bar{\mu}$  and  $\bar{\mu}_{H_2O}$  are the mean values of the attenuation coefficient of tissue and water, respectively. Therefore the CT number is a CT-scanner-dependent quantity with fixed values for water, 0, and air, -1000. Now the task is how to convert the HU of the patient's CT into information suitable for treatment planning. At least, two different approaches could be used: in the TRiP code, by establishing a relation between particle ranges and CT numbers [7]; in MC codes as proposed by Schneider *et al.* in [10] and already used in [11–13], by converting the CT data into mass density and chemical composition of human tissues. CT data essentially represent the density of the electrons in tissue, and it is the electron density which determines, in first approximation, the ion stopping power and hence the dose deposited as well as the particle range. The TRiP code, as described in Section 4.2, is based on the assumption of water targets. However, biological tissues, for example lung and bone, have densities which differ considerably from that of water. In TRiP, the basic idea to account for such density variations is to apply the concept of water equivalent path length (WEPL) when an ion traverses a CT voxel. High density voxels correspond to ion path lengths larger than that for water, low density voxels to shorter ion path lengths. In this way the trajectory of an ion through a CT cube is transformed from the CT system into a water-equivalent system in the beam's-eye view. Thus an originally regular shaped target volume will be distorted in the water equivalent system (Figure 4.6). The advantage of this approach is that the models developed for water targets can be used without any major changes taking into account only the necessary coordinate system transformations between the CT system and the beam's-eye view. However, there is no direct functional dependence between Hounsfield numbers and equivalent path lengths on the basis of a theoretical approach. The Hounsfield numbers reflect the attenuation of X-rays, mainly by photoelectric effect at the energy

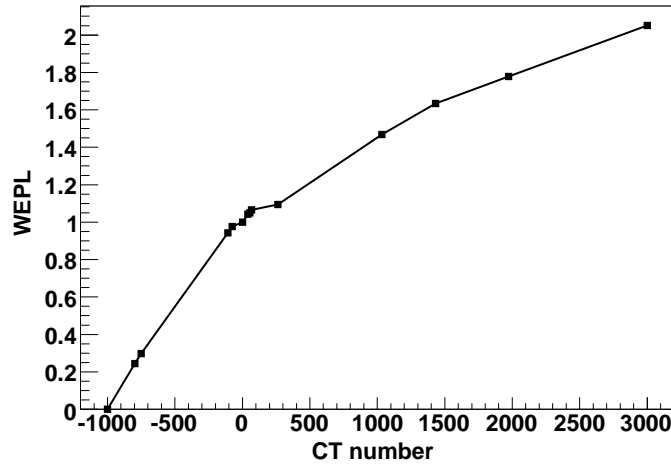


Figure 4.7: Correlation between CT Hounsfield numbers and water-equivalent path lengths (*courtesy of K. Parodi*) [125].

regime of the conventional CT-scanners (typical mean energy 50-100 keV), while the ion path length is dominated by the ion energy loss process. So, for the TRiP code, it has been adopted an experimental approach to deal with this problem: residual ranges behind tissue equivalent phantom materials as well as bovine and human bony tissues [123,124] were compared to ranges in water. A scatter plot of measured path lengths versus CT numbers is reported in Figure 4.7. In this way, the ion path length is stretched according to Figure 4.7.

On the contrary, Monte Carlo codes could be able to take into account the realist patient anatomy with a clear advantage over the water-equivalent approach. In the FLUKA code it is possible to model parts of the simulated geometry in terms of voxels. Voxels are three-dimensional parallelepipeds, all of equal dimensions, which fill a given region of space like small bricks. The algorithm used for voxel geometries is designed in order to minimize memory requirements (2 bytes per voxel only) and it employs a dynamical scheme which allows to keep at minimum the number of voxels actually used for tracking (two per each different material), resulting in very fast-tracking performances. In this work, the CT data in the TRiP format are processed offline prior to the start of the simulation and converted into a suitable voxel format to be input into FLUKA. The latter step is achieved using a modified version, ‘READPATIENT.f’, of the user-oriented ‘writegolem.f’ program included in the FLUKA distribution. This routine originally provided by K. Parodi (HIT) has been further developed in order to read and then to transform the CT scans used by TRiP into density and elemental composition for MC simulations. According to the logic of FLUKA, all voxels with the same CT number are identified as a spatial *region*, while a segmentation of the CT is performed to reduce the number of *material* to be assigned to the regions. CT scans



### 4.3. Monte Carlo calculations of dose in carbon ion therapy

---

are subdivided into 33 HU intervals, i.e., materials to be defined in FLUKA via the ‘MATERIAL’ and ‘COMPOUND’ cards. Elemental composition and nominal density (i.e., density corresponding to the HU value at the center of the considered interval) of 24 materials are taken from the work of [10] resulting from the analysis of 71 human tissues in the HU range between -1000 and 1600. To constrain the variation of the real mass density within a given interval, the two original intervals for  $-1000 \leq \text{HU} < -120$  are implemented as nine materials of the same composition but different nominal density [12,13]. For HU larger than 1600, the extension proposed in [12,13] is implemented.

Nuclear and electromagnetic processes depend on the mass density, varying with the HU values within each material characterized only by the nominal density in the MC. To account for this, region (i.e., CT number) dependent scaling factors are introduced, as suggested in [11] and already applied in [12,13] for dose calculations in proton therapy. While nuclear processes are assumed to rescale only with the ratio between the mass density and the nominal mean density, the electromagnetic processes are furthermore adjusted to reproduce the same dependence between HU and the water equivalent path length shown in Figure 4.7. Starting from the electron density and mean ionization energy of the 33 materials (the original 24 as proposed in [10], plus the subdivision in the lung/adipose tissue region, plus the extension to larger CT numbers in the bone region [12,13]) implemented in FLUKA, it has been calculated the carbon ion stopping power relative to water ( $\rho_s$ ) using the Bethe-Bloch formula [126].  $\rho_s$  can be approximated by

$$\rho_s = \rho_e \frac{\log \left[ \frac{2m_e c^2 \beta^2}{I_m (1-\beta^2)} \right] - \beta^2}{\log \left[ \frac{2m_e c^2 \beta^2}{I_{\text{water}} (1-\beta^2)} \right] - \beta^2} \quad (4.13)$$

where  $\rho_e$  is the relative electron density,  $\beta c$  is the carbon ion velocity,  $m_e$  is the electron mass and  $I_m$  is the mean ionization energy of the target atoms. The carbon ion stopping power relative to water  $\rho_s$  could approximately reproduce the WEPL. The electromagnetic scaling factors have been then calculated taking into account the density variation within each HU interval and further adjusted reproducing the calibration curve reported in Figure 4.7. In order to validate this approach it has been simulated the irradiation of phantoms, corresponding to different CT numbers, with carbon ion pencil beams at different energies. An example of the sub-millimetre agreement of the FLUKA calculations with the TRiP ones is reported in Figure 4.8. With the mentioned approximation the difference between the Bragg peak positions is less than 1 mm (the histogram bin width is 0.5 mm) fulfilling the clinical requirements. The discrepancies in the absolute value are due to the different weighting of the energy deposition, TRiP considers the CT phantoms as water stretching the ion path using the WEPL table, while in our calculations we divide the energy deposition (already normalized per unit volume) by the real density of tissue

#### 4. Clinical CT-based calculations of dose in carbon ion therapy using the FLUKA code

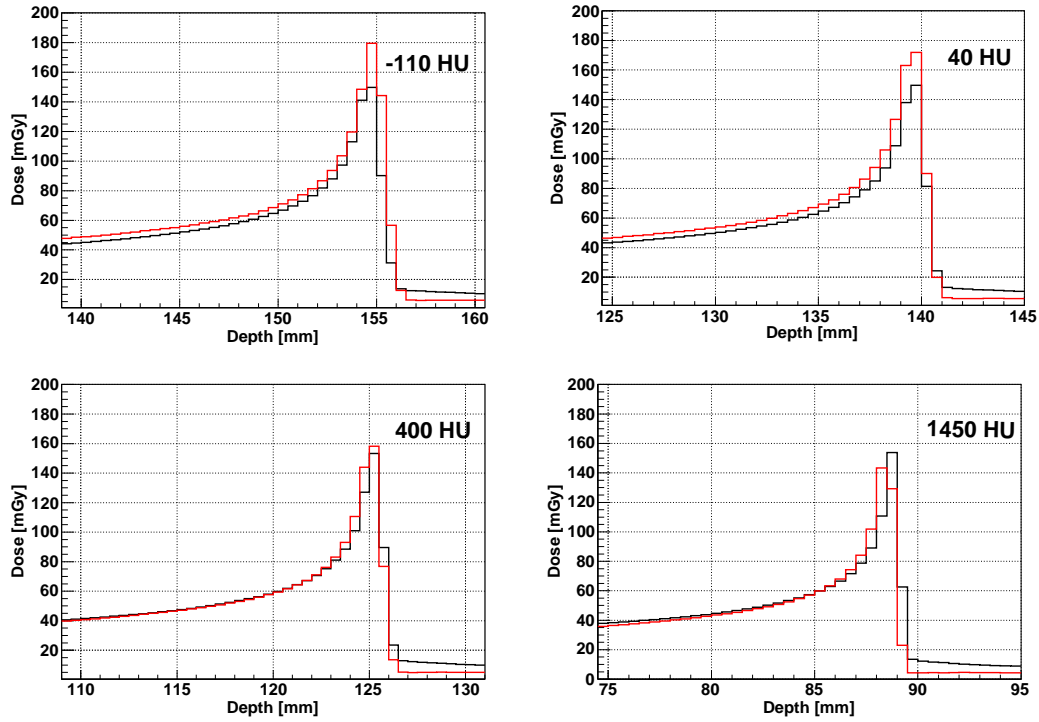


Figure 4.8: Comparison between TRiP (black histograms, *courtesy of K. Parodi and S. Brons*) and FLUKA (red histograms) 270 MeV/n pristine Bragg peaks ( $\Delta E/E = 0.04\%$ ) calculated in phantoms corresponding to the indicated CT numbers.

corresponding to the CT number. The conversion of CT numbers into mass density used in our calculation is reported in Figure 4.9. The resulting patient-specific information on the materials and scaling factors to be assigned to the regions corresponding to the processed CT scan is finally stored in suitable

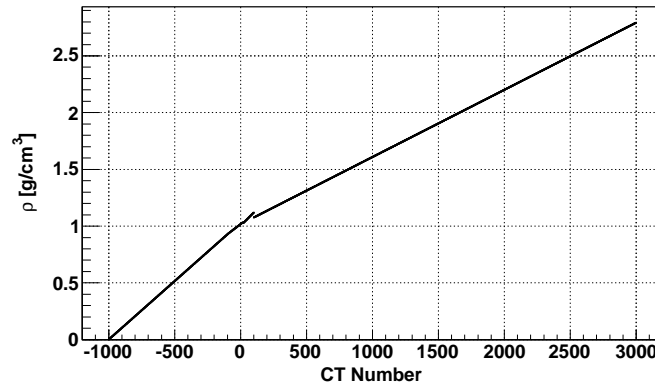


Figure 4.9: Conversion of CT numbers into mass density extending the original one proposed in [10] to HU > 1600.

### 4.3. Monte Carlo calculations of dose in carbon ion therapy

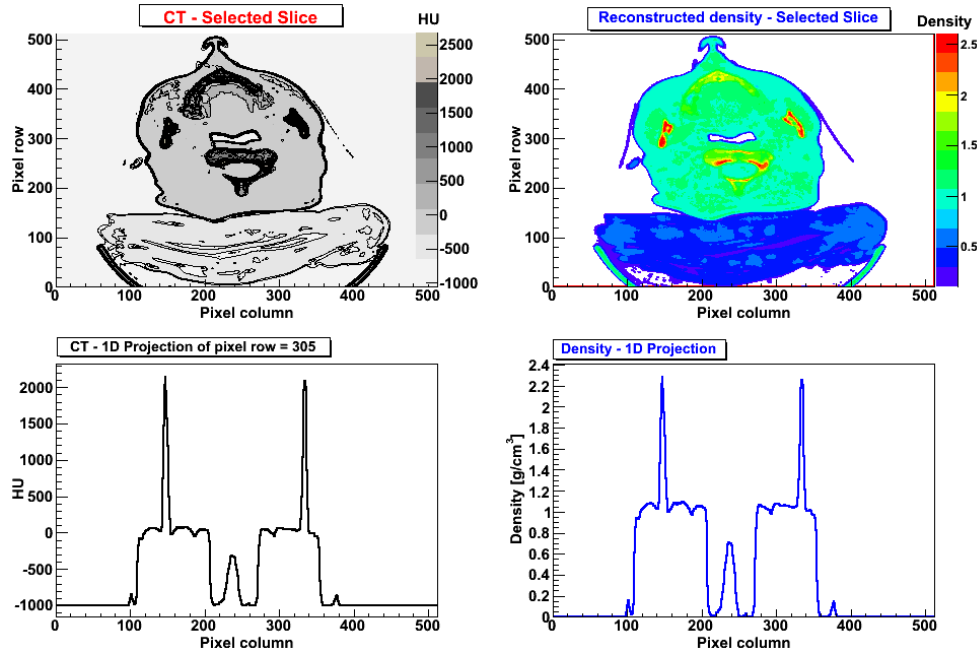


Figure 4.10: A screen-shot of the developed ROOT based software used to visualize and to analyze CT images. Upper-left panel: a selected slice of a DICOM brain CT image; upper-right panel: the selected slice converted into mass density; bottom: one-dimensional projection of the selected pixel row (left panel) and its conversion into mass density (right panel).

format for direct use in the FLUKA input via the ‘ASSIGNMA’ and ‘CORRFAC’ cards. The position of the CT scan respect to the treatment unit isocentre together with its name is transferred to FLUKA via the ‘VOXEL’ card.

In order to visualize and analyze the CT images in different formats (DICOM, TRiP-format, etc.) an interactive ROOT [127] based software using the described conversion procedures has been developed. An example of the obtained results is shown in Figure 4.10 for a slice of a DICOM brain CT image (upper-left panel) converted into density scale (upper-right panel). One-dimensional projections in terms of CT numbers and mass density are shown in bottom panels. In addition the user can also visualize the elemental composition of each CT pixel. Moreover, this tool could be very useful in extreme situations, like in presence of metallic implants, in order to manage pixel overflow problems and their conversion into mass density and elemental composition.

#### 4.3.3 CT-based calculations of dose

This section reports few comparisons between MC and analytical calculations of dose for a patient treated at GSI. The analytical calculations together with the ‘rst-file’ and the patient CT image have been kindly provided by K. Parodi

(HIT) while the programs ('source.f' and 'READPATIENT.f') stressed in the previous sections have been used in order to perform FLUKA simulations.

For optimal performances of the FLUKA simulations, the suite of physics settings recommended for applications to hadron therapy was activated. These include detailed transport of primary carbon ions and secondary particles using the most accurate algorithm for multiple Coulomb scattering of charged particles and restricting the charged hadron transport step size to a corresponding 2% loss of kinetic energy. The latter is determined from continuous-slowing-down-approximation tabulations calculated on a fine mesh (i.e., 1.03 ratio between upper and lower interval limit of  $dp/dx$  momentum loss) and corrected for restricted ionization fluctuations ('HADROTHErapy' default in the FLUKA manual). To reduce computing time without compromising the accuracy of the simulations, differently from the 'HADROTHErapy' default, the continuous-slowing-down-approximation without the production of  $\delta$ -rays has been activated for the charged hadrons. Moreover, for an accurate description of nuclear reactions, in addition to the standard nucleus-nucleus event generator, the new low energy one (not released in the FLUKA distribution) described in Chapter 2, has been activated.

Heavy fragments and nuclear recoils were also transported in detail, i.e., including energy loss, multiple scattering and nuclear interactions. For all hadrons but neutrons, the transport threshold, i.e., the energy below which particles are ranged to rest in only one step and energy is deposited uniformly over the residual path, was set to 100 keV as suggested in FLUKA manual. Neutrons are slowed down to thermal energies.

Accurate algorithms for scoring energy deposition in Cartesian or cylindrical regular meshes, which are geometry-independent (i.e., not constrained by region boundaries and not affecting the transport step size), are available

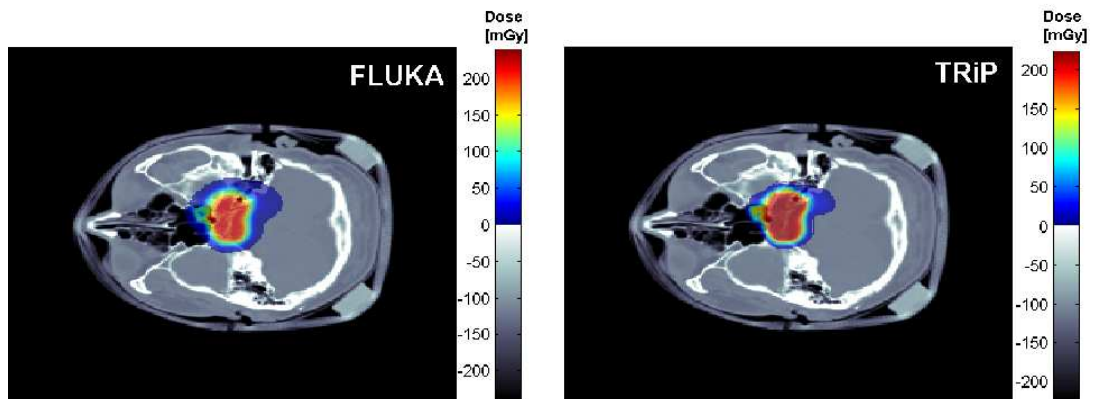


Figure 4.11: MC calculated dose deposition (left) against the planned treatment (right) in a transversal view of a cranial plan. The rainbow colour-bar displays dose values. The black-white colour-bar represents the HU map arbitrary rescaled for display purposes.

### 4.3. Monte Carlo calculations of dose in carbon ion therapy

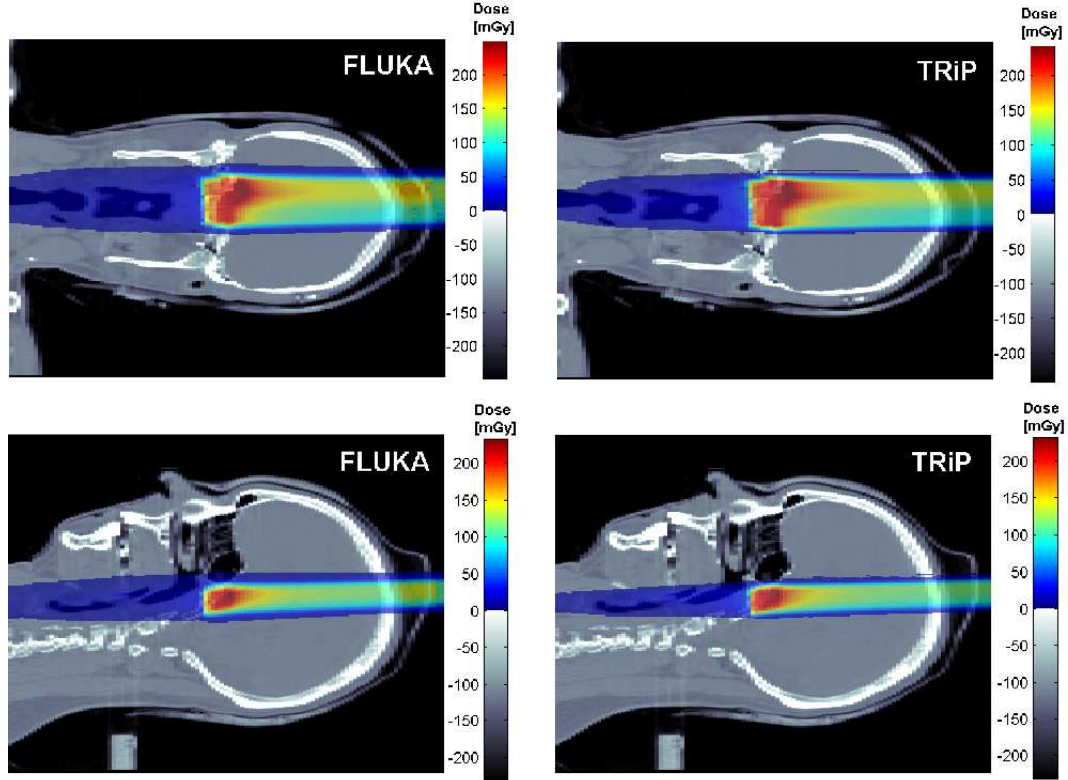


Figure 4.12: MC calculated dose deposition (left) against the planned treatment (right) in different views along the beam axis. The upper panels refer to the coronal plan while the above ones refer to the sagittal plan. In this last view the beam is tilted by the gantry angle. The rainbow colour-bar displays dose values. The black-white colour-bar represents the HU map arbitrary rescaled for display purposes.

in FLUKA via the ‘USRBIN’ input card. A user-routine ‘comscw.f’ can be additionally activated to divide the energy deposition (already normalized per unit volume) by the medium density to obtain the deposited dose. In our implementation, as suggested in [13], this division was activated correcting the ‘nominal’ material density to the ‘real’ value by means of the same factors used to rescale nuclear processes.

The FLUKA particle transport was performed in a CT scan of  $256 \times 256$  transaxial pixels for 106 slices, the pixel dimension is about 1.21 mm and the distance between two consecutive slices is 3 mm. Dose results of TPS are saved with the same spatial resolution of the CT image of the treated patient; the FLUKA grid for dose scoring has been chosen according to the TRiP one. A total number of about 17 million primary particles were sampled from the  $N(E_{beam}, x, y)$  fluence distribution according to the ‘raster-file’ and transported in 10 independent FLUKA runs. The dose results were rescaled to the dose prescription using a factor of 1/10, given by the ratio between the total number of particles used to irradiate the target volume (according to the ‘raster-file’)

and FLUKA simulated primary carbon ions. In general, the shapes of the calculated MC and the TRiP dose distributions are found in good agreement with each others. Nice comparisons between MC and analytical calculation of dose in different views are shown in Figures 4.11 and 4.12. Exceptions occur in the cases more sensitive to the limitations of analytical dose calculations, similar to the findings in proton therapy simulations [11, 13]. These include e.g. regions of low/high density interfaces like air cavities, where dose deposition is however of non clinical significance. A clear example is given by Figure 4.13 which shows an one-dimensional SOBP sampled at about -13 mm from the isocentre of the profiles reported in Figure 4.12-upper panels. In the Bragg peak region the FLUKA (blue line) and the analytical (black line) results agree satisfactorily. On the contrary, in the entrance region there is an evident discrepancy due to low/high density interface. In fact this region corresponds to a large variation in the CT profile (red line). Unlike the results obtained in proton therapy [11, 13], there are additional differences in the distal part of the dose distribution due to the secondary fragments produced in nuclear fragmentation. From the lateral dose distribution reported in Figure 4.14 comes evident that the different weighting of the energy deposition slightly changes the absolute values of the dose profiles. In fact, as already mentioned, the treatment planning system calculates dose deposition only by the corresponding adjustment of the penetration depth. On the contrary, the CT-based Monte Carlo calculation accurately models (as described in Section 4.3.2) the electromagnetic and nuclear processes keeping into account the specific tissue elemental composition deduced from the stoichiometric calibration of the CT scan.

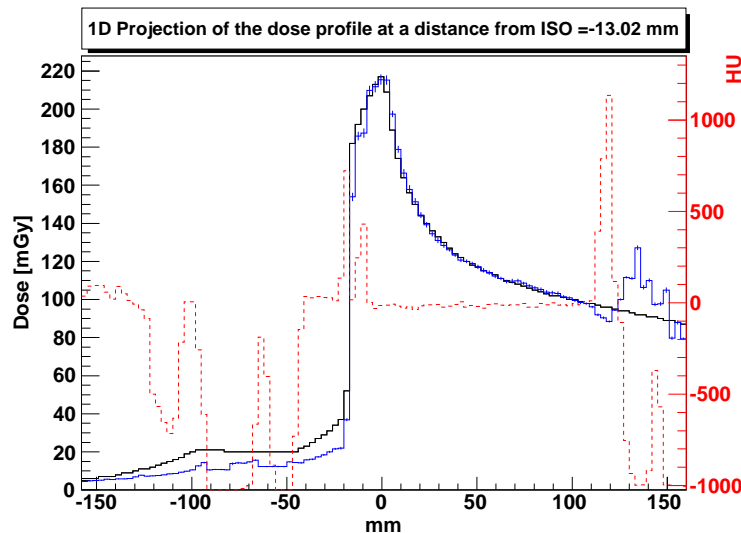


Figure 4.13: Comparison between MC (blue line) and TRiP (black line) calculated depth-dose deposition. The depth dose profile is taken at about -13 mm from the isocentre of the profiles reported in Figure 4.12-upper panels. The corresponding CT profile is shown by the red line.

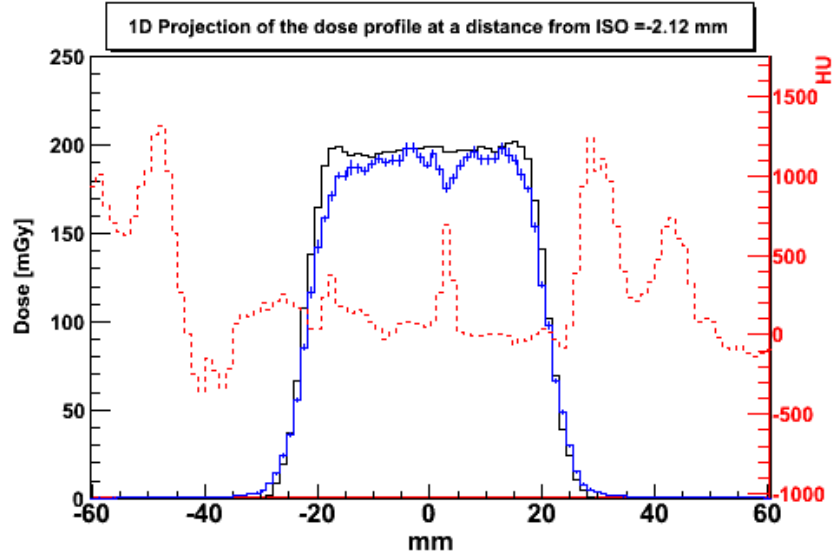


Figure 4.14: Comparison between MC (blue line) and TRiP (black line) lateral dose distribution. The lateral field is taken at about -2 mm from the isocentre of the slices reported in Figure 4.11. The corresponding CT profile is shown by the red line.

To summarize, satisfactory agreement between MC and analytical dose calculations has been found for the studied cranial plan. The deviations are tightly related to the different treatment of the nuclear reactions and to the different managing of the CT scan. Although the long computing time prevents, at the moment, their use in clinical routine, MC tools, and FLUKA in particular, can be very useful for validation of the dose calculations performed by the analytical TPSs. Future comparisons between the FLUKA code and the production and development versions of the TRiP treatment planning system for other patient cases treated at GSI are planned in collaboration with K. Parodi and S. Brons (HIT, Heidelberg).

#### 4. Clinical CT-based calculations of dose in carbon ion therapy using the FLUKA code

---



# Chapter 5

## The Local Effect Model and its interface with FLUKA

### 5.1 Introduction

A major rationale for the application of ion beams in tumor therapy is their increased relative biological effectiveness (RBE) in the Bragg peak region (BPR), especially for carbon and heavier ions (Chapter 1). For dose prescription, the increased effectiveness has to be taken into account in treatment planning.

For protons the RBE is usually assumed to be 1.1 in clinical practice, although there is an evidence for an increased RBE which varies with depth [128, 129]; on the contrary for heavy charged particles like  $^{12}\text{C}$  the scenario is more complex. At the Lawrence Berkeley Laboratory (LBL, Berkely/USA) the RBE was described as a function of dose-averaged LET to estimate the biologically effective dose [130], using a linear quadratic (LQ) model to calculate a uniform biological effect along the spread-out Bragg peak (SOBP). At the Japanese facilities in Chiba (HIMAC) and Hyogo (HIBMC) biological treatment planning is based on cell survival levels which are calculated using a LQ model as well. Starting from mono-energetic beams the dose-averaged coefficients  $\alpha$  and  $\beta$  for a mixed field are calculated. For patient planning, human salivary gland (HSG) tumor cells are used to obtain the RBE distribution as a function of depth. All RBE values are scaled according to the RBE observed in clinical studies with neutrons depending on the position in the SOPB showing the same RBE for cell survival as neutrons [67, 68]. At GSI (Darmstadt) the biophysical LEM (Local Effect Model) approach [2–4, 8, 131, 132] developed by M. Scholz *et al.* is used.

In this chapter we give a brief description of the GSI model and its Monte Carlo implementation in the FLUKA code. The LEM model was successfully applied within treatment planning in the GSI pilot project for carbon ion tumor therapy over almost 10 years since now. This model is based on the knowledge of charged particle track structure in combination with the response of bio-

logical objects to conventional photon radiation. The RBE of charged particle beams depends on several factors like particle type and energy, dose level, the position in treatment field and the cell or tissue type under consideration. These systematic dependencies of the RBE have to be considered in the treatment planning when using charged particle beams for therapy. As a consequence, RBE values are expected to be patient-specific and can not be adequately represented by a single number for the conversion of physical absorbed dose to biological effective dose.

In the next section the LEM model is briefly described. In Section 5.3 the radiobiology in treatment planning is outlined focusing on the fundamental aspects necessary for understanding the interface with the FLUKA code. In Section 5.4 the *problem* of mixed fields is treated and the last section is devoted to a comparison with the experimental data and the analytical calculations kindly provided by M. Scholz (GSI). The FLUKA results presented within this chapter are obtained using a development version of the official release (*fluka2006.3b*) which includes the BME event generator (Chapter 2) in order to better estimate the mixed radiation fields in the BPR.

This chapter reports the results, still unpublished, of the work carried out in common with M. Krämer, A. Ottolenghi, M. Scholz, using a database, analytical calculations and experimental data confidentially provided by M. Scholz, not authorized for circulation and uses in other contexts.

## 5.2 The Local Effect Model

The principal assumption of the LEM is that the local biological effect, i.e. the biological damage in a small subvolume of the cell nucleus, is determined only by the expectation value of the energy deposition in that subvolume and is independent of the particular radiation type leading to that energy deposition. In other words, all the differences in the biological action of charged particle beams should then be attributed to the different spatial energy deposition pattern of charged particles compared to photon radiation, i.e. on track structure. Furthermore, for a given radiation type, differences in the photon dose response curve for different biological objects or tissues should also lead to corresponding differences in the RBE.

The energy deposition pattern of charged particles is essentially determined by the secondary electrons ( $\delta$ -electrons) liberated by the primary particle when penetrating matter. Experimental data [133, 134] as well as model calculations [135, 136] revealed, that the average energy deposition at a distance  $r$  from the trajectory, obeys the  $1/r^2$ -law. According to the kinematics of secondary electron emission, the maximum transversal range of the electrons is limited and the corresponding track radius can be described by a power law of the form [2]:

$$R_{max} = c E^{1.7} \quad (5.1)$$

## 5.2. The Local Effect Model

---

where  $c$  is a constant and  $E$  is the specific energy of the projectile.

The cell nucleus is assumed to be the critical target in LEM. Disregarding changes in size and shape throughout the cell cycle, the geometrical shape of the nucleus is assumed to be cylindrical to a first approximation, with a radius  $R_{nucleus}$ , and the axis parallel to the particle trajectory.

Figure 5.1 illustrates the influence of track structure on the microscopic dose distribution ( $d(x, y, z)$ ) in the typical dimensions of a cell nucleus [5]. The dose distribution is defined as the average energy deposition at a certain location for a given fixed set of impact parameters of the incoming particles, divided by the target mass. For comparison, the distribution expected for photon irradiation is shown as an ideally flat plane; this is based on the fact that photons deposit their energy in a very large number of small energy depositions. Thus, as a first approximation, the average energy deposition is homogeneously distributed throughout the cell nucleus. In contrast, low energy (1 MeV/n) particles show a completely different pattern. Since their track radius is very small, their energy deposition is restricted to very small subvolumes along the particle trajectory, but there is no energy deposition at all in between. With increasing the particle energy, the track radius increases, and the gap between the tracks is closed; in these cases, considerable overlap between individual particle tracks contributes to the dose deposition. With increasing the particle energy, the heterogeneity of the microscopic dose distribution decreases and more and more resembles the photon dose distribution. This figure already qualitatively explains, why high-energy carbon ions tend to act more and more similarly to photons, as the energy increases.

In order to determine the biological effectiveness of these heterogeneous dose distributions, a reference to the photon dose response curve has been made. According to LEM, the cell inactivation is assumed to be the consequence of the induction of *lethal events*: with increasing dose, an increasing number of lethal events is produced in the nucleus. However, a single lethal event is sufficient to inactivate the cell. According to the homogeneous dose distribution as shown in Figure 5.1, it has been assumed a random distribution of lethal events within the cells of a population for a given photon dose. Given the average number of lethal events  $\overline{N_X^{lethal}}$ , the fraction of cells carrying no lethal event is determined by the Poisson distribution:

$$S_X = e^{-\overline{N_X^{lethal}}} . \quad (5.2)$$

For photon radiation, the density of lethal events  $\nu_X(D)$  in the cell nucleus can be defined as follows:

$$\nu_X(D) = \frac{\overline{N_X^{lethal}(D)}}{V_{nucleus}} = \frac{-\ln S_X(D)}{V_{nucleus}} \quad (5.3)$$

where  $V_{nucleus}$  is the volume of the cell nucleus,  $D$  is the dose,  $\overline{N_X^{lethal}(D)}$  represents the average number of the lethal events produced by photon radiation in the nucleus by a dose  $D$  and  $S_X(D)$  denotes the cell survival probability at

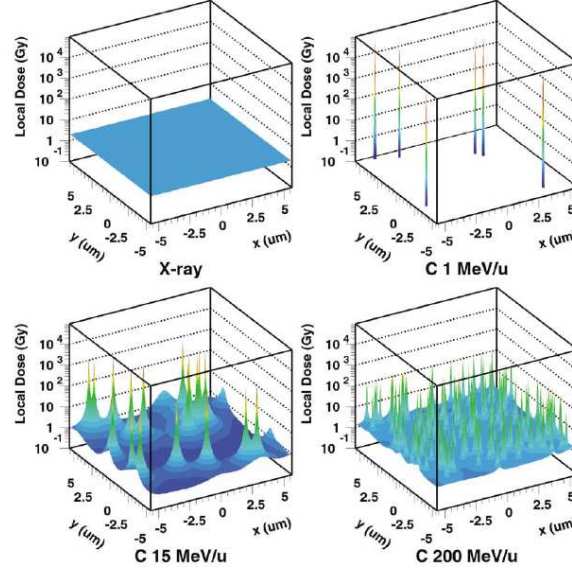


Figure 5.1: Local dose distributions of X-rays and carbon ions at different specific energies. The average dose is 2 Gy in each case. The size of the area is  $10 \times 10 \mu\text{m}^2$  and corresponds to the typical size of mammalian cell nuclei [5].

the dose  $D$ .

The average number of lethal events induced per cell by heavy ion irradiation can be obtained by the integration of the local event density  $\nu_{ion}(d(x, y, z))$

$$\overline{N_{lethal}^{ion}}(D) = \int \nu_{ion}(d(x, y, z)) dV_{nucleus} . \quad (5.4)$$

According to the principles described above, the fundamental assumption of the LEM is that the local biological effect is determined by the local dose, but is independent of the particular radiation type, i.e.  $\nu_{ion}(d) = \nu_X(d)$ .

Thus, equal local doses correspond to equal local biological effects, and Eq. 5.4 can be written as

$$\overline{N_{lethal}^{ion}}(D) = \overline{-\ln(S^{ion}(D))} = \int \frac{-\ln S_X(d(x, y, z))}{V_{nucleus}} dV_{nucleus} . \quad (5.5)$$

This formula clearly demonstrates the theoretical link between the biological effect of photon radiation and ion radiation. The particle effect is *hidden* in the inhomogeneous local dose distribution  $d(x, y, z)$ . The concept of the LEM is schematically illustrated in Figure 5.2.

A modified version of the linear-quadratic approach for the photon dose response curve is used, since for many biological objects a transition from the shouldered to an exponential shape is observed at high doses. This transition is

## 5.2. The Local Effect Model

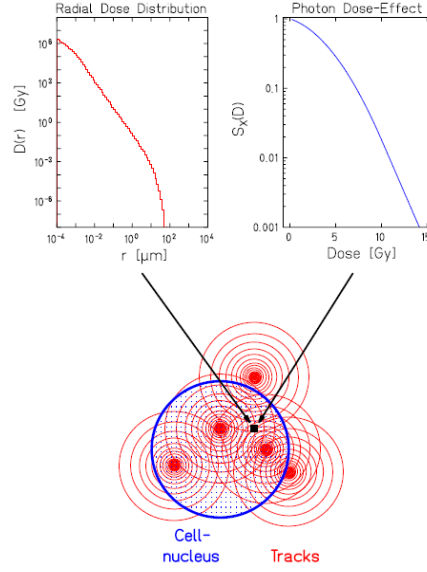


Figure 5.2: Schematic representation of the Local Effect Model [137].

described by a parameter  $D_{cut}$ , representing the transition dose to exponential shape with slope  $s_{max} = \alpha + 2\beta D_{cut}$ , so that the dose response is finally determined by:

$$-\ln S = \begin{cases} \alpha_X D + \beta_X D^2 & D \leq D_{cut} \\ \alpha_X D_{cut} + \beta_X D_{cut}^2 + s_{max}(D - D_{cut}) & D > D_{cut} \end{cases} \quad (5.6)$$

This formulation has been chosen as a convenient parametrization of the X-ray survival curves; it does not imply that the model is principally restricted to a specific form of the survival curve. In general, the transition dose  $D_{cut}$  cannot be directly derived from the experimental data and it represents a semi-free parameter of the model.

The integration in Eq. 5.5 is not trivial, since the spatial distribution of  $d(x, y, z)$  is highly irregular on a submicroscopic level, however one can utilize efficient sampling procedures [138]. Nevertheless, with a mixed particle spectrum (see Section 5.4), it is thus difficult to achieve the computation rapidity that is required in treatment planning for heavy ion therapy. Therefore approximation procedures have been developed, related to the estimation of the  $\beta$ -parameter of the dose response curve. The  $\alpha$ -parameter can be always calculated exactly according to Eq. 5.5, since the initial slope corresponds to the effect at very low doses and fluences. The initial slope  $\alpha_z$  of the ion dose-effect curve is pre-calculated and stored in the input database of TRiP [7, 8] as *initial RBE* =  $\alpha_z \alpha_X$ . On the contrary, for  $\beta_z$  is applied, as suggested by Scholz *et al* in [3],  $\beta_z \approx (s_{max} - \alpha_z)/2D_{cut}$ .

In Figure 5.3, the *initial RBE* as a function of particle energy and particle type for a Chordoma cell line is shown. It has a maximum at low energy and it decreases becoming fairly constant at high energy. So it's very important to have a nucleus-nucleus reaction model able to describe correctly nuclear

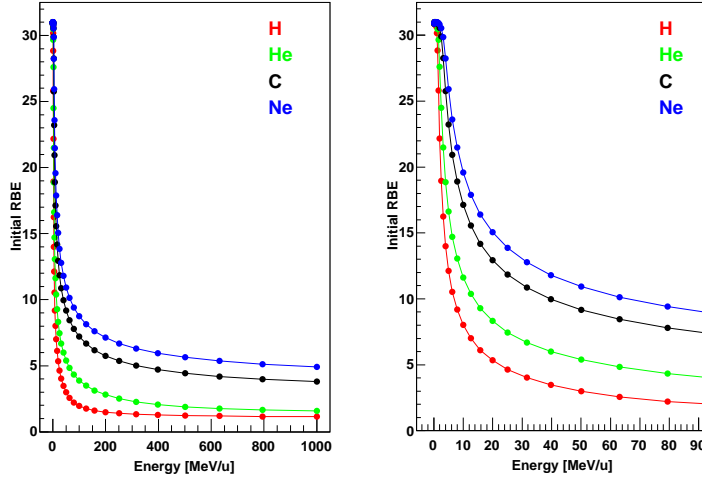


Figure 5.3: Left panel: *initial* RBE as a function of the particle kinetic energy for a Chordoma cell line (*courtesy of M. Scholz (GSI)*): H ions (red line), He ions (green line), C ions (black line) and Ne ions (blue line). Right panel: a zoom in the low energy region.

reactions at low energy, in order to exactly estimate the RBE in the BPR. In FLUKA, as described in Chapter 2, this has been recently done in the framework of the BME theory. At fixed energy per nucleon, the *initial* RBE is larger for heavier ions; heavy fragments, with atomic number higher than those of the interacting ions (typically  $^{12}\text{C}$ , as projectile, and  $^{16}\text{O}$  as target nucleus of the biological tissue), are mostly produced as evaporation residues in complete fusion and break-up-fusion reactions with relatively low energies, as outlined in Chapter 2.

### 5.3 The radiobiology in Treatment Planning: TRiP rapid calculation

The main idea of the LEM model is, that the biological effect,  $-\ln(S)$ , in a cell nucleus can be expressed in terms of traversals of particles of a particular type and energy:

$$-\ln(S(z_{cn})) = \alpha_z z_{cn} + \beta_z z_{cn}^2 \quad (5.7)$$

where  $z_{cn}$  is the specific energy (not the *macroscopic* dose) deposited by the particle in the cell nucleus and  $\alpha_z$  and  $\beta_z$  are the *intrinsic* coefficients already described in the previous section. To calculate the biological effect,  $-\ln(S(D))$ , for a given radiation field in the *classical* approach [8], a two level random sampling procedure must be used: from the given particle fluence and cell nucleus area the average number of ion traversals are calculated and the actual number is sampled from a Poisson distribution. For this number of particles the

### 5.3. The radiobiology in Treatment Planning: TRiP rapid calculation

---

damage is accumulated according to the local particle spectrum (in particle type and energy), in order to account for all, or at least the most important combinations of particles that might traverse a cell nucleus. The whole procedure is repeated several (typically 500 to 1000) times and finally  $-\ln(S(D))$  is obtained as an average over these repetitions. This method has some drawbacks concerning the calculation speed. First, sampling procedures are time consuming. Second, the sampling of the particle distribution for each voxel involves the interpolation of large histograms from the database, which is even more time consuming. Hence M. Scholz and M. Krämer (GSI) in [132] found a method that leads from  $-\ln(S(z))$  to  $-\ln(S(D))$  in a more straightforward fashion.

For a given radiation field with known composition leading to a dose  $D$ , the biological effect in terms of macroscopic dose can be expressed in a linear quadratic *ansatz* [2]

$$-\ln(S(D)) = \alpha_D D + \beta_D D^2 . \quad (5.8)$$

The initial slope  $\alpha_D$  can be determined in the limit of low doses:

$$\alpha_D = \lim_{D \rightarrow 0} \frac{-\ln(S(D))}{D} \quad (5.9)$$

for low doses, hence low fluences, the probability,  $\eta$ , for a cell nucleus to be hit is small and the Poisson probability reduces to a 1-hit probability

$$\eta = 1 - \exp(-AF_\eta) \quad (5.10)$$

where  $A$  is the cell nucleus area and  $F_\eta$  the particle fluence.

The survival can be obtained as

$$-\ln(S(D_\eta)) = -\ln(1 - \eta(1 - S_1)) \quad (5.11)$$

where

$$D_\eta(\text{Gy}) = C F_\eta(\text{mm}^{-2}) \text{LET}\left(\frac{\text{MeV}}{\text{g cm}^{-2}}\right) . \quad (5.12)$$

where  $C = 1.602189 \cdot 10^{-8}$  and  $S_1$  is the surviving fraction for a single particle traversal:

$$S_1 = \exp(-\alpha_z d_1) \quad (5.13)$$

with  $d_1 = C \frac{\text{LET}}{A}$ . Putting things together and following the approach described in [132], it's possible to obtain a simple expression for the initial slope  $\alpha_D$

$$\alpha_D = \frac{(1 - S_1)}{d_1} . \quad (5.14)$$

For the determination of  $\beta_D$ , it has been defined a scaling factor  $f$

$$f = \frac{\alpha_D}{\alpha_z} = \frac{1 - S_1}{\alpha_z d_1} \quad (5.15)$$

$$\beta_D = f^2 \cdot \beta_z . \quad (5.16)$$

This scaling approach for  $\beta_D$  is just an *ansatz*,  $\beta_D$  is associated with the dose squared and hence should also be scaled squared. While the derivation of  $\alpha_D$  can be viewed as *exact*, the estimation of  $\beta_D$  has been verified against the classical method [132]. M. Scholz and M. Krämer (GSI) found that the described approach is valid for therapeutical dose levels up to the order of 10 GyE per fraction, so this new algorithm has been referred as *low-dose* approximation [132].

## 5.4 Mixed radiation fields

*Event-by-event* track structure simulations (i.e., reproducing each energy deposition at nanometre scale) can be very helpful in understanding the action of radiation in biological targets, since they can represent a starting point for the development of *ab initio*, mechanistic models of the process leading from the initial energy depositions at the nanometre level to the induction of observable biological damage at sub-cellular and cellular level. This type of simulations cannot be used for treatment planning in radiotherapy, due to the enormous number of interactions involved and the unsustainable amount of computer time that would be required.

A *condensed history* approach is therefore applied [139], in which continuous processes, for which the mean free paths are much smaller than particles ranges, and discrete processes are treated separately. This method is very efficient and can be very reliable. An obvious consequence is a loss of information that in few instances, such as in the case of hadron therapy, can be particularly important, due to the strong variation of radiation quality (and consequently of radiation effectiveness) along the beam in the irradiated tissues. In this situation, it is evident that the absorbed dose is not sufficient and the spatial characteristics of the different components of the mixed field must be taken into account, in order to estimate the biological effectiveness. A good compromise between condensed-history approaches and event-by event codes can be the integration in condensed history Monte Carlo codes (FLUKA in this work) of results of calculations carried out using event-by-event track structure codes. Condensed history codes, alone, do not allow taking into account in full detail the high stochasticity that characterizes the energy deposition processes and their evolution in the initial biological damage.

A possible solution, as previously mentioned, consists in integrating such codes with radiobiological information obtained from experimental data or starting from event-by-event track structure simulations [140]. This approach was adopted in previous works to characterize therapeutic proton beams from a physical and biophysical point of view [129, 141]. More specifically, it was assumed that the number of *Complex Lesions* (CLs, where a CL is a clustered DNA damage defined as two or more double-strand breaks within 30 DNA base pairs) is proportional to the number of lethal lesions. The integration of



#### 5.4. Mixed radiation fields

---

the CL yields in FLUKA provided a spatial distribution of the yield of CL/cell, a quantity that can be regarded as a *biological dose*; the excellent agreement with cell survival data allowed the authors to validate the method.

However, this method can be reliably applied only at relatively low doses (say below 2 Gy), since the linear increase of CL with dose does not take into account the dose-dependence observed in RBE measurements. An improvement of the above method has been used for the study of chromosome aberration induction in human cells by neutrons [142]. The theory of dual radiation action (TDRA) [143] has been included to describe these cases of non-linear response due to mixed fields.

The authors of the TDRA stated that a biological system exposed to more than one radiation type will show synergism, implying that the total number of lesions is larger than the sum of the lesions produced by each single beam component, due to interactions between sub-lesions produced by different components.

If the yield ( $Y$ ) of lesions follows a linear-quadratic ( $\alpha$ - $\beta$ ) formula, as experimentally investigated in the case of chromosome aberrations [142],

$$Y(D) = \alpha D + \beta D^2 \quad (5.17)$$

the sequential exposure to two doses  $D_1$  and  $D_2$  (with the subscripts referring to two different radiation types), gives the following yield of lesions:

$$Y(D_1, D_2) = \alpha_1 D_1 + \beta_1 D_1^2 + \alpha_2 D_2 + \beta_2 D_2^2 + 2(\beta_1 \beta_2)^{1/2} D_1 D_2 \quad (5.18)$$

where  $\alpha_1, \beta_1$  and  $\alpha_2, \beta_2$  are the parameters of Eq. 5.17 for radiation types 1 and 2. The method can be generalised to  $n$  doses from different radiation types (each characterized by a certain value of the parameters  $\alpha_i$  and  $\beta_i$ ); the expression 5.18 becomes

$$\epsilon(D_1, D_2, \dots, D_n) = \sum_{i=1}^n \alpha_i D_i + \left( \sum_{i=1}^n \sqrt{\beta_i} D_i \right)^2. \quad (5.19)$$

Within this formalism the average parameters for a mixed field can be calculated:

$$\bar{\alpha} = \frac{\sum_{i=1}^n \alpha_i D_i}{\sum_{i=1}^n D_i}, \quad (5.20)$$

$$\bar{\beta} = \left( \frac{\sum_{i=1}^n \sqrt{\beta_i} D_i}{\sum_{i=1}^n D_i} \right)^2. \quad (5.21)$$

In [142] the authors have calculated neutron induced aberration yields starting from published data obtained from in vitro irradiation of human lymphocytes with photons and charged particles. More specifically, the irradiation of a water phantom with neutron beams of different energies was simulated with FLUKA. The code was modified by integration of experimentally derived values for the

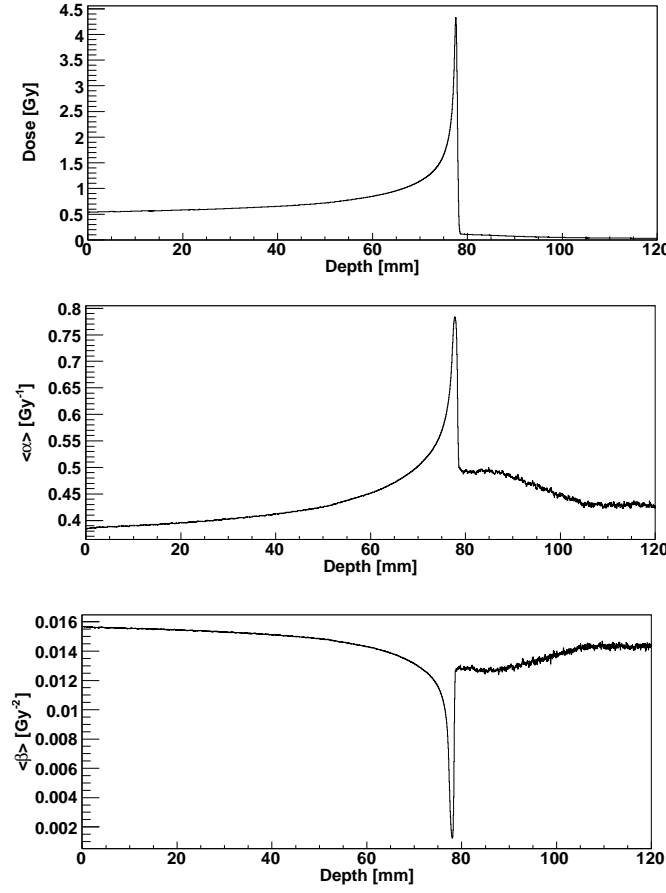


Figure 5.4: Physical dose (upper panel) and linear-quadratic model parameters, average  $\alpha$  (middle panel) and  $\beta$  (low panel) values, obtained with the FLUKA-LEM calculations as a function of depth in water for CHO cells, after irradiation with carbon ions. Entrance energy of the carbon beam: 187 MeV/n.

linear coefficient  $\alpha$  and the quadratic coefficient  $\beta$  characterising dicentric induction by each radiation type (photons, electrons, protons and heavier ions) produced by neutron interaction with water. Whenever an energy  $E$  was deposited in a target voxel by a certain radiation type, the following quantities were added in three different arrays:  $E$  (first array),  $\alpha \cdot E$  (second array) and  $\sqrt{\beta} \cdot E$  (third array), with  $\alpha$  and  $\beta$  taken from published experimental studies and corresponding to the particular radiation (in term of particle type and energy) depositing the energy  $E$ . At the end of the simulation, for each voxel the average parameters have been calculated using Eq. 5.20 and Eq. 5.21. Application of the equation  $Y(D) = \alpha D + \beta D^2$  allowed the calculation of the neutron dicentric yield in each voxel of the target water phantom.

In this work, in order to calculate cell survival and consequently the biological dose and RBE for carbon ion irradiation the same approach proposed

in [132] has been used. Starting from the *initial* RBE tables (in term of particle type,  $1 \leq Z \leq 10$ , and energy per nucleon  $\leq 1$  GeV/n, see an example in Figure 5.3) normally used in TRiP for therapy we determine online, during the Monte Carlo simulation, the  $\alpha_D$  and  $\beta_D$  parameters for each ion following Eq. 5.14 and Eq. 5.16.

At the end of the simulation we calculate for each voxel the dose-weighted averages,  $\bar{\alpha}$  and  $\bar{\beta}$ , for the mixed field using Eq. 5.20 and Eq. 5.21 respectively. An example of the average parameters obtained for a mono-energetic carbon ion pencil beam (187 MeV/n) entering a water phantom used to simulate a target of CHO cells is reported in Figure 5.4. The  $\bar{\alpha}$  and  $\bar{\beta}$  profiles show respectively a maximum and a minimum at the Bragg peak mainly due to the primary carbon ions. On the contrary, the secondary lower-charge fragments, having longer ranges than the primary beam, give rise to the tail beyond the Bragg peak. In the BPR the possibility to interface the FLUKA code with the new BME event generator (Chapter 2) permits to evaluate more reliably the mixed field and consequently the  $\bar{\alpha}$  and  $\bar{\beta}$  parameters.

Finally the biological effect  $-\ln(S)$  and biological dose,  $D_{bio}$ , are calculated using the same formalism introduced by M. Scholz *et al.* in [132]:

$$-\ln(S) = \begin{cases} (\bar{\beta}D_{abs} + \bar{\alpha})D_{abs} & D_{abs} \leq D_{cut} \\ (\bar{\beta}D_{cut} + \bar{\alpha})D_{cut} + (D_{abs} - D_{cut})s_{max} & D_{abs} > D_{cut} \end{cases} \quad (5.22)$$

$$D_{bio} = \begin{cases} \sqrt{-\ln(S)/\beta_X + (\alpha_X/2\beta_X)^2} - (\alpha_X/2\beta_X) & -\ln(S) \leq -\ln(S_{cut}) \\ (-\ln(S) + \ln(S_{cut}))/s_{max} + D_{cut} & -\ln(S) > -\ln(S_{cut}) \end{cases} \quad (5.23)$$

where  $D_{abs}$  is the physical absorbed dose.

## 5.5 Results and discussion

In order to validate the implementation of the FLUKA-LEM interface and to study the role of ion fragmentation in the biological framework, it has been simulated the clonogenic survival, the biological dose and the RBE in water phantoms used to simulate targets of different cells (see for example Table 5.1) after the irradiation with carbon beams at different entrance energies. In this section only a small set of the simulations done to validate the approach is reported, the same conclusions could be obtained also for the other calculations not shown here; the experimental data, the TRiP and TRiPbeam (the

Cell line	$\alpha_X$ (Gy <sup>-1</sup> )	$\beta_X$ (Gy <sup>-2</sup> )	$\alpha/\beta$ (Gy)	$D_{CUT}$ (Gy)	$R_{nucl}$ ( $\mu$ m)
CHO	0.2	0.019	10.5	30	5.5
Chordoma	0.1	0.05	2.0	30	5.0

Table 5.1: Parameters of the LEM model for the dose response of two cell lines [8, 145].

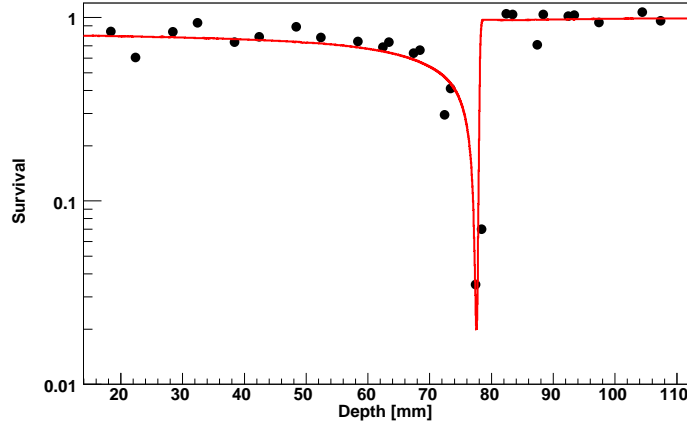


Figure 5.5: Clonogenic survival of CHO cells after irradiation with carbon ions, as a function of depth in water: FLUKA-LEM calculations (red line) and experimental data (full circles [3], *courtesy of M. Scholz*). Entrance energy of the carbon beam: 187 MeV/n as outlined in [144]. The experimental entrance particle fluence of  $2 \cdot 10^7/\text{cm}^2$  is used for the simulations.

development version of TRiP) calculations have been kindly provided by M. Scholz (GSI).

It has been simulated, using the FLUKA-LEM interface, the survival fraction for Chinese hamster ovary (CHO) [3] cells. More specifically, the irradiation of a water phantom with a 187 MeV/n (as outlined in [144], the nominal experimental energy was 195 MeV/n) carbon beam at an entrance particle fluence of  $2 \cdot 10^7/\text{cm}^2$  has been simulated. Following the procedure previously described starting from the  $\bar{\alpha}$  and  $\bar{\beta}$  of Figure 5.4 and using Eq. 5.22 it has been possible to calculate cell survival. Within the first few centimetres of penetration depth, survival remains nearly constant, followed by a sharp decrease in the region of the Bragg peak. These features are reasonably reproduced by the FLUKA-LEM as in the original paper of M. Scholz *et al.* [3] using the TRiP code. In Figure 5.6 the survival curves as a function of entrance particle fluence, calculated at different penetration depths for a 270 MeV/n  $^{12}\text{C}$  beam, are compared with the experimental data. The overall comparison with the experimental data is satisfactory except at 0 mm penetration depth for high entrance fluence values. The same disagreement with the experimental data has been found also in [3] probably due to experimental uncertainties. Figure 5.7 shows the relative effect of the primary particles and of secondary fragments at different penetration depths. The blue lines indicate the reduction in survival that is solely due to the primary particles, whereas the red lines indicate the total biological effect. At 0 mm depth only the primary particles are responsible of the cell survival, moving to high penetration depth the importance of nuclear products increases. In order to validate the FLUKA-LEM interface, it has been simulated the survival, the biological dose and the RBE

## 5.5. Results and discussion

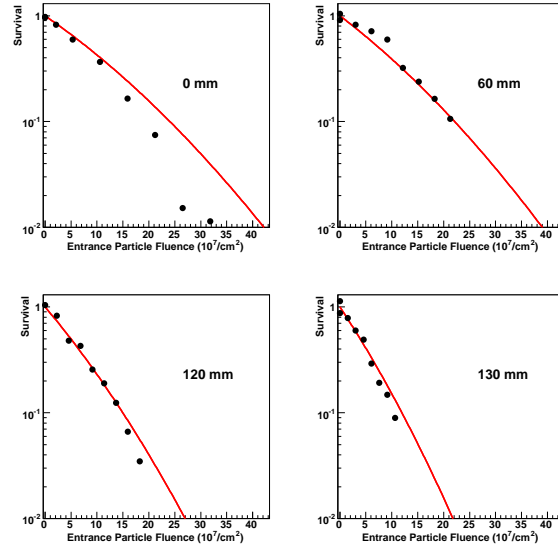


Figure 5.6: Clonogenic survival of CHO cells after irradiation with carbon ions, as a function of particle fluences, at various depths in water: FLUKA-LEM calculations (red line) and experimental data (full circles [3], *courtesy of M. Scholz*). Entrance energy of the carbon beam: 270 MeV/n. All particle fluences refer to zero penetration depth.

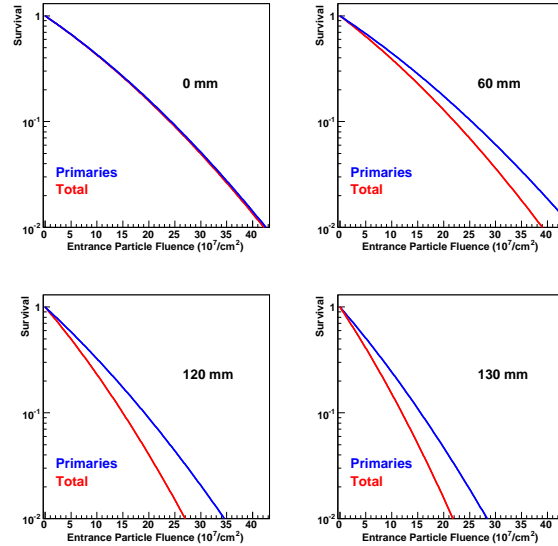


Figure 5.7: Clonogenic survival of CHO cells after irradiation with carbon ions, as a function of particle fluences, at various depths in water computed with FLUKA-LEM for the primary particles alone (blue line) and for the primaries and their secondary fragments (red line). Entrance energy of the carbon beam: 270 MeV/n. All particle fluences refer to zero penetration depth.

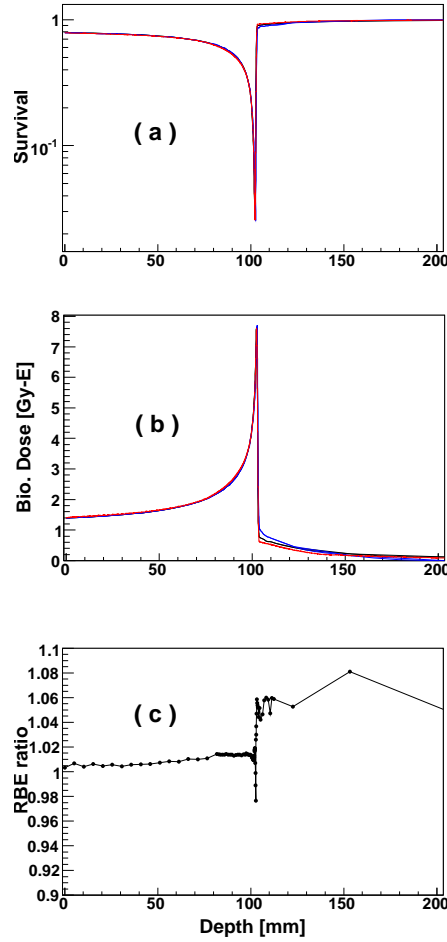


Figure 5.8: Clonogenic survival (panel a), biological dose (panel b) as a function of depth in water: FLUKA-LEM calculations (red line), TRiP (blue line) and TRiPbeam as of August-2006 (black line, *courtesy of M. Krämer and M. Scholz (GSI)*). In panel c the ratios between Monte Carlo calculated and TRiPbeam calculated RBE (as a function of depth in water), are reported. Calculations are relative to a Chordoma cell line,  $\alpha/\beta = 2$  Gy). Entrance energy of the carbon beam: 219.8 MeV/n.

of water phantoms made of different cell lines irradiated by carbon beams at five different energies (149 - 378 MeV/n) and at eight different dose levels (0.1 - 10 Gy). Figure 5.8 shows the comparison between the Monte Carlo (red lines), TRiP (blue lines) and TRiPbeam (black lines) calculations for a Chordoma cell line of clonogenic survival (panel a) and biological dose (panel b). Appreciable differences can be observed for high penetration depths due to different treatment of nuclear fragmentation. Panel c of Figure 5.8 shows the ratio of FLUKA-LEM and TRiPbeam calculated RBEs. The deviation is less than 10% at all penetration depths; the discrepancies after the BPR are due mainly to different mixed fields in terms of particle type and particle energy.

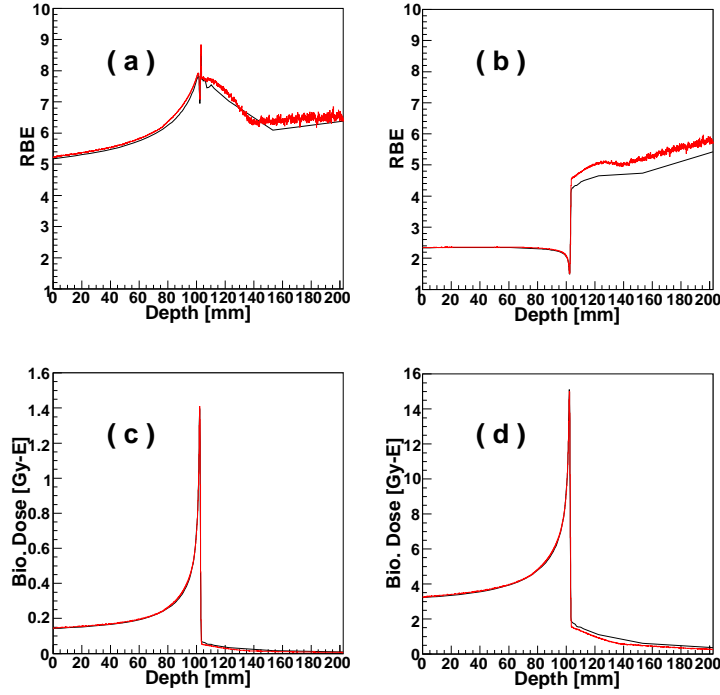


Figure 5.9: RBE (panels a, b) and biological dose (panels c, d) for a Chordoma cell line as a function of depth in water for different carbon fluences. Panels a and c :  $1.14 \cdot 10^6$  carbon ions/cm<sup>2</sup>, peak dose = 0.2 Gy; panels b and d:  $5.7 \cdot 10^7$  carbon ions/cm<sup>2</sup>, peak dose = 10 Gy. The curves represent FLUKA-LEM (red line) and TRiPbeam as of August-2006 (black line, *courtesy of M. Krämer and M. Scholz (GSI)*) calculations.

The last comparison has been performed to study the effect of dose level on the RBE and on the biological dose profiles. At low doses (low fluences) the MC and the analytical calculations agree reasonably. At higher fluences on the contrary, a systematic difference can be observed in the fragmentation tail because the effect of nuclear reactions becoming important at high dose levels.

Different comparisons with experimental data and analytical calculations have showed that the FLUKA-LEM interface reproduces reasonably the biological response of different cell lines in the framework of Local Effect Model. A systematic difference at high penetration depth is mainly due to the description of the nuclear processes, and further future studies on this topic are needed.





# Conclusions and perspectives

Treatment planning systems (TPSs) for ion therapy are essentially analytical codes based on fast performing pencil-beam algorithms. However, Monte Carlo (MC) statistical methods are increasingly considered as powerful tools for accurate calculations of dose deposition, since they are assumed to provide a more realistic representation of the physical interactions undergone by the primary beam and the resulting secondaries. Especially important, as outlined in this work, is the modelling of nucleus-nucleus reactions in the energy range of therapeutic relevance.

Chapter 2 presented the results of an experiment made at the iThemba LABS, South Africa, for measuring the spectra of the intermediate mass fragments (IMFs) produced in the  $^{12}\text{C} + ^{12}\text{C}$  interaction at 200 MeV bombarding energy. The measured spectra are analyzed by a binary fragmentation model and the BME theory as implemented in the transport and interaction MC code FLUKA. Although the agreement between the experimental spectra and the theoretical predictions, in which complete fusion and break-up-fusion reactions were considered, is far from being perfect, nevertheless the overall comparison with the data shows that these reaction mechanisms certainly play an important role in these reactions. Future developments of the BME event generator are planned in order to describe in a comprehensive way the nuclear interactions at energies ranging from the Coulomb barrier up to 100 MeV/n :

- the extension of the pre-equilibrium description to ion pairs not included in the complete fusion database;
- the refinement of the break-up-fusion model, implemented as a 3 bodies process in the FLUKA-BME development version and as a 2 bodies process in the version actually used in this work;
- the inclusion of the IMFs emission in the pre-equilibrium phase.

New experimental campaigns are planned at the iThemba LABS in order to study the same system at higher energies, as well as other systems of therapeutic interest such as  $^{16}\text{O} + ^{12}\text{C}$ .

At higher energies (from 100 MeV/n up to few GeV/n), Quantum Molecular Dynamics (QMD) models represent a suitable way to describe the initial hot stage of heavy ion reactions. The FLUKA code interfaced with a modified version of rQMD-2.4 and with the BME event generator permitted to reliably estimate the mixed field produced by the irradiation of a water phantom with a 400 MeV/n carbon beam. In heavy-particle therapy nuclear reactions may cause a significant alteration of the radiation field. High energy fragmentation reactions occurring along the beam penetration path in tissue lead to the attenuation of the primary beam flux and build-up of secondary lower-charge fragments which give rise to the characteristic dose tail behind the Bragg peak. These features, experimentally measured at GSI for a 400 MeV/n carbon beam, are satisfactorily reproduced by the FLUKA code (Chapter 3). This is one of the most important aspects to achieve trustworthy physical and especially biological dose calculations.

Clinical CT-based calculations of dose in carbon ion therapy stressed in Chapter 4 have shown how a MC approach could be advantageous in situation sensitive to nuclear reactions and in presence of low/high density interface. Moreover, MC methods allow to evaluate the dose for every real situation, taking into account the realistic patient anatomy instead of the water-equivalent approach, and for all the cases in which experimental dosimetric verification is impossible. Satisfactory agreement between MC and analytical dose calculations has been found for the studied cranial plan. The deviations are tightly related to the different treatment of the nuclear reactions and to the different managing of the CT scan. Future comparisons between the FLUKA code and the analytical treatment planning system for other patient cases treated at GSI, are planned. Although the long computing time prevents, at the moment, the use of a MC approach in clinical routine, a hybrid solution (MC calculated physical databases input into TPS) could be a promising way.

One of the major rationales for the application of carbon beams in tumor therapy is their increased biological effectiveness in the tumor volume in comparison to the lower effectiveness in the surrounding healthy tissue. In Chapter 5 the biological aspects of the ion interaction with tissue were described in the framework of the Local Effect Model. The FLUKA code has been interfaced with this model and this has permitted to calculate the cell survival, the biological dose and the RBE after the irradiation of water phantoms simulating targets of different cells with carbon beams at various energies. The nice comparisons against experimental data and TRiP/TRiPbeam analytical calculations, except for the latter ones in the tail behind the Bragg peak due to the different treatment of nuclear reactions, represent the first step in order to study the biological effects in a clinical situation. In fact, the most interesting development that we would like to explore is merging the clinical CT-based calculations of physical dose with the biological effect quantification in order to completely reproduce a clinical patient case also from the biological point of view.

# Bibliography

- [1] J. Sisterson, *Particles* **28** (2001) 12
- [2] M. Scholz, G. Kraft, *Adv. Space Res. Vol.* **18** (1996) 5
- [3] M. Scholz *et al.*, *Radiat. Environ. Biophys.* **36** (1997) 59
- [4] G. Kraft *et al.*, *Radiat. Environ. Biophys.* **38** (1999) 229
- [5] M. Krämer *et al.*, *Technology in Cancer Research & Treatment Vol.* **2**, N. **5**, 427 (2003)
- [6] U. Amaldi, *Nucl. Phys.* **A 751** (2005) 409
- [7] M. Krämer *et al.*, *Phys. Med. Biol.* **45** (2000) 3299
- [8] M. Krämer and M. Scholz, *Phys. Med. Biol.* **45** (2000) 3319
- [9] O. Jäkel *et al.*, *Phys. Med. Biol.* **46** (2001) 1101
- [10] W. Schneider *et al.*, *Phys. Med. Biol.* **49** (2000) 459
- [11] H. Jiang and H. Paganetti, *Med. Phys.* **31 (10)** (2004) 2811
- [12] K. Parodi *et al.*, *Med. Phys.* **34 (2)** (2007) 419
- [13] K. Parodi *et al.*, *Phys. Med. Biol.* **52** (2007) 1
- [14] W. Enghardt *et al.*, *Phys. Med. Biol.* **37** (1992) 2127; *Nucl. Instr. Meth.* **A 525** (2004) 284
- [15] A. Ferrari *et al.*, *CERN 2005-10* (2005)
- [16] A. Fassò *et al.*, *hep-ph/0306267*
- [17] H. Sorge, H. Stöcker, and W. Greiner, *Nucl. Phys.* **A 498** (1989) 567c; H. Sorge, H. Stöcker, and W. Greiner, *Ann. Phys. (N.Y.)* **192** (1989) 266
- [18] E. Haettner, *Master of Sci. Thesis, KTM, Stockholm*, 2006

- [19] E. Haettner *et al.*, Rad. Prot. Dos. **122** (2006) 485
- [20] G. Gademann, Proc. 1<sup>st</sup> Int. Symposium on Hadrontherapy, Como, Italy, October 18 - 21, 1993. In: U. Amaldi, B. Larsson (eds), Hadrontherapy in Oncology, Excerpta Medica, Int. Congr. Series 1077, Elsevier Science 1994, 59
- [21] A. J. M. Vermoken and F. A. J. M. Schermer (eds), Vol. **5** of Biomedical and Health Research, Amsterdam - Oxford - Washington DC - Tokyo, IOS PRESS, 1994
- [22] W. H. Scharf and O. A. Chomiccki, Physica Medica XII (1996) 199
- [23] A. Wambersie, in: P. Chauvel and A. Wambersie, Eulina Workshop on the potential value of light ion beam therapy, Pub. n. EUR 12165, Commission of the European Community, Brussels, 1989
- [24] G. Kraft, Prog. Part. Nucl. Phys. **45** (2000) 473
- [25] C. A. Tobias *et al.* Cancer Res. **18** (1958) 121
- [26] W. T. Chu *et al.* Rev. Sci. Instrum. **64** (1993) 2055
- [27] J. R. Castro, Proc. 1<sup>st</sup> Int. Symposium on Hadrontherapy, Como, Italy, October 18 - 21, 1993. In: U. Amaldi, B. Larsson (eds), Hadrontherapy in Oncology, Excerpta Medica, Int. Congr. Series 1077, Elsevier Science 1994, 208
- [28] G. Coutrakon *et al.*, Proc. 1<sup>st</sup> Int. Symposium on Hadrontherapy, Como, Italy, October 18 - 21, 1993. In: U. Amaldi, B. Larsson (eds), Hadrontherapy in Oncology, Excerpta Medica, Int. Congr. Series 1077, Elsevier Science 1994, 282
- [29] T. Kanai *et al.*, Biol. Phys. **44** (1999) 201
- [30] E. A. Blakely, Proc. 1<sup>st</sup> Int. Symposium on Hadrontherapy, Como, Italy, October 18 - 21, 1993. In: U. Amaldi, B. Larsson (eds), Hadrontherapy in Oncology, Excerpta Medica, Int. Congr. Series 1077, Elsevier Science 1994, 693
- [31] W. Pedroni *et al.*, Med. Phys. **22** (1995) 37
- [32] Th. Haberer *et al.*, Nucl. Instr. Meth. **A 330** (1993) 296
- [33] W. Enghardt *et al.*, Strahlenther. Onkol. **175** (1999) 33
- [34] R. R. Wilson, Radiol. **47** (1946) 487
- [35] W. H. Bragg and R. Kleeman, Phil. Mag. **8** (1904) 726

## BIBLIOGRAPHY

---

- [36] U. Linz, in: U. Linz (ed.), Ion Beams in Tumour Therapy, Chapman & Hall, London - Glasgow - Weinheim - New York - Tokyo - Melbourne - Madras, 1995, 15
- [37] H. A. Bethe, Ann. Phys. **5** (1930) 325
- [38] F. Bloch, Ann. Phys. **16** (1933) 285
- [39] W. H. Barkas, in: Nuclear Research Emulsions, Vol. **I**, Academic Press, New York - London, 1963, 371
- [40] H. D. Betz, Rev. Mod. Phys. **44** (1972) 465
- [41] T. Schwab, Ph.D. Thesis, GSI Report 91-10, 1991
- [42] K. Parodi, Ph.D. Thesis, Dresden University of Technology, 2004
- [43] N. Bohr, Phil. Mag. **30** (1915) 581
- [44] S. P. Ahlen, Rev. Mod. Phys. **52** (1980) 121
- [45] W. R. Leo, *Techniques for nuclear and particle physics experiments*, Springer-Verlag, Berlin, 1987
- [46] G. Z. Molière, *Theorie der Streuung schneller geladener Teilchen. II. Mehrfach- und Vielfachstreuung*, Z. Naturforsch. **3a** (1948) 78
- [47] V. L. Highland, Nucl. Instr. Meth. **129** (1975) 497
- [48] Th. Haberer, Ph.D. Thesis, GSI Report 94-09, 1994
- [49] A. Fleury *et al.* Ann. Rev. Nat. Part. Sci. **24** (1974) 279
- [50] H. Paganetti, Phys. Med. Biol. **47** (2002) 747
- [51] C. P. Karger *et al.*, Z. Med. Phys. **12** (2002) 159
- [52] D. E. Greiner *et al.*, Phys. Rev. Lett. **35** (1975) 152
- [53] F. Pönisch *et al.*, Phys. Med. Biol. **49** (2004) 5217
- [54] J. Pawelke *et al.*, IEE Trans. Nucl. Sci. **44** (1997) 1492
- [55] B. G. Hasch, Ph.D. Thesis, Dresden University of Technology, 1996
- [56] F. Ballarini and A. Ottolenghi, Radiat. Res. **164**(4) (2005) 567
- [57] F. Ballarini *et al.*, Adv. Space Res. **40** (2007) 1392
- [58] A. Ottolenghi *et al.*, Int. J. Radiat. Biol. **72** (1997) 505
- [59] W. K. Weyrather *et al.*, Int. J. Radiat. Biol. **75** (1999) 1357

- [60] M. Belli *et al.*, Int. J. Radiat. Biol. **55** (1989) 93
- [61] M. Belli *et al.*, Int. J. Radiat. Biol. **74** (1998) 501
- [62] G. W. Barendsen *et al.*, Radiat. Res. **18** (1963) 106
- [63] G. Kraft *et al.*, Nucl. Sci. Appl. **3** (1987) 1
- [64] L. G. Gerweck *et al.*, Radiother. Oncol. **50** (1999) 135
- [65] T. Furusawa *et al.*, Radiat. Res. **154** (2000) 485
- [66] W. K. Weyrather, in: Progress in Radio-Oncology VII, 353. Eds. H. D. Kogelnik, P. Lukas, F. Sedlmayr, Moduzzi Editore, 2002
- [67] T. Kanai *et al.*, Radiat. Res. **147** (1997) 78
- [68] T. Kanai *et al.*, Int. J. Radiat. Oncol. Biol. Phys. **44** (1999) 201
- [69] S. V. Förtsch *et al.*, Proceedings of the International Conference on Nuclear Data for Science and Technology, Santa Fe, New Mexico, 26 September - 1 October 2004, R. C. Haight, M. Chadwick, T. Kawano and P. Talou Edts., AIP Conference Proceedings, Volume **769** (2005) 1642
- [70] S. V. Förtsch *et al.*, *Contributions of complete fusion and break-up-fusion to intermediate mass fragment production in the low energy interaction of  $^{12}\text{C}$  and  $^{27}\text{Al}$* , Nucl. Phys. **A** (2007), doi:10.1016/j.nuclphysa.2007.09.007
- [71] E. Gadioli *et al.*, Eur. Phys. J. **A8** (2000) 373; **A11** (2001) 161
- [72] E. Gadioli *et al.*, Nucl. Phys. **A708** (2002) 391
- [73] E. Gadioli *et al.*, Eur. Phys. J. **A17** (2003) 195
- [74] B. Becker *et al.*, Eur. Phys. J. **A18** (2003) 639
- [75] L. J. Mudau *et al.*, Nucl. Phys. **A761** (2005) 190
- [76] Buthelezi *et al.*, Nucl. Phys. **A753** (2005) 29; Eur. Phys. J. **A28** (2006) 193
- [77] L. Sihver *et al.*, Phys. Rev. **C 47** (1993) 1225
- [78] ICRU 2000 *Nuclear Data for Neutron and Proton Radiotherapy and for Radiation Protection*, ICRU Report **63** (2000), International Commission on Radiation Units and Measurements
- [79] R. Barna *et al.*, Nucl. Instr. Meth. **A 519(3)** (2004) 610
- [80] J. Czudek *et al.*, Phys. Rev. **C 43** (1991) 1248

## BIBLIOGRAPHY

---

- [81] E. Gadioli and P. E. Hodgson, *Pre-Equilibrium Nuclear Reactions*, Oxford Science Publications, Clarendon Press, Oxford 1992
- [82] R. Serber, Phys. Rev. **72**, (1947) 1008
- [83] K. W. McVoy and C. Nemes, Z. Phys. **A295** (1980) 177
- [84] M. S. Hussein, K. W. McVoy and D. Saloner, Phys. Lett. **B98** (1981) 182
- [85] S. L. Tabor, L. C. Dennis and K. Abdo, Phys. Rev. **C24** (1981) 2552
- [86] M. Cavinato *et al.*, Nucl. Phys. **A643** (1998) 15 ; Nucl. Phys. **A679** (2001) 753
- [87] C. Brusati *et al.*, Z. Phys. **A353** (1995) 57
- [88] F. Cerutti *et al.*, Proceedings of the 11th International Conference on Nuclear Reaction Mechanisms, Varenna, June 12-16, 2006, E. Gadioli edt., Ricerca Scientifica ed Educazione Permanente, Suppl. **126** (2006) 507
- [89] F. Cerutti, A. Clivio and E. Gadioli, Eur. Phys. J. **A25** (2005) 413
- [90] P. J. Karol, Phys. Rev. **C11** (1975) 1203
- [91] R. R. Betts *et al.*, Phys. Rev. Lett. **39** (1977) 1183
- [92] M. Buenerd *et al.*, Phys. Rev. Lett. **40** (1978) 1482
- [93] E. Gadioli *et al.*, Nucl. Phys. **A 654** (1999) 523
- [94] V. V. Balashov, A. N. Boyarkina and I. Rotter, Nucl. Phys. **59** (1964) 417
- [95] A. Ferrari *et al.*, Nucl. Instr. Meth. **B 71** (1992) 412
- [96] A. Fassò *et al.*, Proc. 3rd Workshop on Simulating Accelerator Radiation Environments, KEK, Tsukuba (Japan) 7-9 May 1997. Ed. H. Hirayama, KEK Proceedings 97-5 (1997) 32
- [97] F. Sommerer *et al.*, Phys. Med. Biol. **51** (2006) 4385
- [98] V. Andersen, F. Ballarini, G. Battistoni *et al.*, Adv. Space Res. **34(6)** (2004) 1302
- [99] H. Aiginger *et al.*, Adv. Space Res. **35** (2005) 214
- [100] S. Roesler, R. Engel and J. Ranft, Proceedings of the Monte Carlo 2000 Conference, Lisbon, October 23-26 2000, A. Kling, F. Barao, M. Nakagawa, L. Tavora, P. Vazeds., Springer-Verlag Berlin, (2001) 1033

- [101] F. Ballarini *et al.*, Proceedings of the 10th International Conference on Nuclear Reaction Mechanisms, Varenna, June 9-13, 2003, E. Gadioli ed., Ricerca Scientifica ed Educazione Permanente, Suppl. **122** (2003) 579
- [102] T. Kurosawa *et al.*, Phys. Rev. **C 62** (2000) 44615
- [103] J. R. Cummings *et al.*, Phys. Rev. **C 42** (1990) 2508
- [104] J. Benlliure, P. Ambruster *et al.*, Eur. Phys. J. **A2** (1998) 193
- [105] A. Ferrari, P. R. Sala, Proc. MC93 Int. Conf. on Monte Carlo Simulation in High Energy and Nuclear Physics, Tallahassee (Florida), 22-26 February 1993. Ed. by P. Dragovitsch, S.L. Linn, M. Burbank, World Scientific, Singapore 1994, 277
- [106] A. Fassò, A. Ferrari, J. Ranft and P. R. Sala, Proc. of an AEN/NEA Specialists' Meeting on Shielding Aspects of Accelerators, Targets and Irradiation
- [107] K. Gunzert-Marx, Ph.D. Thesis, Darmstadt, 2004
- [108] ICRU 1993 *Stopping powers and ranges for protons and alpha particles*, ICRU Report **49** (1993), International Commission on Radiation Units and Measurements
- [109] H. Bichsel *et al.*, Radiat. Res. **153** (2000) 208
- [110] H. Paul, [http://www.icru.org/n\\_07\\_01.htm](http://www.icru.org/n_07_01.htm)
- [111] J. Lindhard *et al.*, Phys. Rev. **A53** (1996) 2443
- [112] C. Scheidenberger *et al.*, Nucl. Instr. Meth. **B 135** (1998) 25
- [113] H. Geissel *et al.*, Nucl. Instr. Meth. **B 195** (2002) 3
- [114] K. Sümmerer *et al.*, Phys. Rev. **C 42** (1990) 2546
- [115] I. Schall *et al.*, Nucl. Instr. Meth. **B 117** (1996) 221
- [116] D. J. Morissey *et al.*, Phys. Rev. **C 39** (1989) 460
- [117] W. Heinrich *et al.*, GSI Preprint (1991) 91-30
- [118] U. Weber and G. Kraft, Phys. Med. Biol. **44** (1999) 2765
- [119] F. Sommerer (CERN), *private communication*
- [120] T. Eichoff *et al.*, GSI Report 96-01, 1996
- [121] B. Voss *et al.*, GSI Report 98-01, 1998



## BIBLIOGRAPHY

---

- [122] <http://www-aix-old.gsi.de/bio/DOCS/TRiP98/DOCS/trip98coord.html>
- [123] C. Jacob, Ph.D. Thesis, University of Heidelberg, 1997
- [124] O. Jäkel *et al.*, Med. Phys. **28** (2001) 701
- [125] E. Rietzel *et al.*, Radiat. Oncol. **2**:14 (2007)
- [126] H. Bichsel, *Passage of charged particles through matter*, American Institute of Physics Handbook (New York: McGraw-Hill) 1972
- [127] <http://root.cern.ch/>
- [128] B. G. Wouters *et al.*, Radiat. Res. **146** (1996) 159
- [129] M. Biaggi *et al.*, Nucl. Instr. Meth. **B 159** (1999) 89
- [130] P. L. Petti *et al.*, Med. Phys. **18** (1991) 516
- [131] W. Dörr *et al.*, Radiat. Environ. Biophys. **39** (1999) 185
- [132] M. Krämer and M. Scholz, Phys. Med. Biol. **51** (2006) 1959
- [133] M. N. Varma *et al.*, Radiat. Res. **70** (1977) 511
- [134] N.F. Metting *et al.*, Radiat. Res. **116** (1988) 183
- [135] J. Kiefer and H. Straaten, Phys. Med. Biol. **31** (1986) 1201
- [136] M. Krämer and G. Kraft, Radiat. Environ. Biophys. **33** (1994) 91
- [137] M. Scholz, Adv. Space Res. doi:10.1016/j.asr.2007.02.066 (2007)
- [138] A. M. Kellerer, The dosimetry of ionization radiation, Vol. **I**. Academic Press, London, 78, edited by K. R. Kase, B. E. Bjärngard and F. H. Attix, 1985
- [139] A. E. Nahum, Radiat. Environ. Biophys. **38** (1999) 163
- [140] A. Ottolenghi *et al.*, Phys. Med. **17/S2** (2001) 3
- [141] M. Biaggi *et al.*, Phys. Med. **17/S3** (2001) 63
- [142] F. Ballarini *et al.*, Radiat. Prot. Dosim. **103** (2003) 19
- [143] A. M. Kellerer and H. H. Rossi, Radiat. Res. **75** (1978) 471
- [144] P. Kundrát, Radiat. Prot. Dosim. **122** (2006) 480
- [145] M. Scholz (GSI), *private communication*



# List of publications

- S. V. Försch, F. Cerutti, P. Colleoni, E. Gadioli, A. Mairani, G. F. Steyn, J. J. Lawrie, F. D. Smit, S. H. Connell, R. Fearick, T. Thovhogi, H. Machner, F. Goldenbaum, K. Pysz, *Projectile and target fragmentation in the interaction of  $^{12}\text{C}$  and  $^{27}\text{Al}$* . Proc. of the International Conference on Nuclear Data for Science and Technology, Santa Fe, New Mexico, 26 September - 1 October 2004, R. C. Haight, M. Chadwick, T. Kawano and P. Talou Edts., AIP Conference Proceedings, Volume **769** (2005) 1642
- F. Cerutti, F. Ballarini, G. Battistoni, P. Colleoni, A. Ferrari, S. V. Försch, E. Gadioli, M. V. Garzelli, A. Mairani, A. Ottolenghi, P. R. Sala, *Intermediate mass fragment production in light ion reaction*. Proc. Rila Conference, Rila (Bulgaria), June 2005, ed. by S. Dimitrova, Heron Press, Sofia, 2005, 50
- A. Mairani, F. Cerutti, E. Gadioli, A. Pepe, *Interaction of  $^{12}\text{C}$  and  $^{16}\text{O}$  with heavy and medium heavy nuclei*. Proc. Rila Conference, Rila (Bulgaria), June 2005, ed. by S. Dimitrova, Heron Press, Sofia, 2005, 162
- L. J. Mudau, F. Cerutti, E. Gadioli, A. Mairani, S. V. Försch, E. Z. Buthelezi, G. F. Steyn, S. H. Connell, J. J. Lawrie, R. Neveling, F. D. Smit, E. Sideras-Haddad, *Production of  $^3\text{He}$  and of  $^6\text{He}$  fragments in the interaction of  $^{12}\text{C}$  with  $^{93}\text{Nb}$  at 400 MeV*. Nucl. Phys. **A 761** (2005) 190
- E. Gadioli, F. Cerutti, A. Mairani, A. Pepe, *Interaction of  $^{12}\text{C}$  and  $^{16}\text{O}$  with medium-heavy nuclei*. Proc. VI Latin American Symposium on Nuclear Physics and Applications, Iguazú, Argentina, Oct 3-7, 2005, eds. O. Civitarese, C. Dorso, G. Garcia Bermudez, A. J. Kreiner, A. J. Pacheco, N. N. Scoccola, AIP Volume **884** (2007) 207
- F. Cerutti, F. Ballarini, G. Battistoni, P. Colleoni, A. Ferrari, S. V. Försch, E. Gadioli, M. V. Garzelli, A. Mairani, A. Ottolenghi, A. Pepe, L. S. Pinsky, P. R. Sala. *LIGHT ION INTERACTIONS OF CONCERN FOR HADRON THERAPY*. Proc. VI Latin American Symposium on

- Nuclear Physics and Applications, Iguazù, Argentina, Oct 3-7, 2005, eds. O. Civitarese, C. Dorso, G. Garcia Bermudez, A. J. Kreiner, A. J. Pacheco, N. N. Scoccola, AIP Volume **884** (2007) 219
- F. Cerutti, F. Ballarini, G. Battistoni, P. Colleoni, A. Ferrari, S. V. Förtsch, E. Gadioli, M. V. Garzelli, A. Mairani, A. Ottolenghi, A. Pepe, L. S. Pinsky, P. R. Sala, D. Scannicchio, G. F. Steyn, *Carbon induced reactions at low incident energies*. IOP Journal of Physics: Conference Series **41** (2006) 212
  - F. Ballarini, D. Alloni, G. Battistoni, F. Cerutti, A. Ferrari, E. Gadioli, M. V. Garzelli, M. Liotta, A. Mairani, A. Ottolenghi, H. G. Paretzke, V. Parini, M. Pelliccioni, L. S. Pinsky, P. R. Sala, D. Scannicchio, S. Trovati, M. Zankl, *Modelling human exposure to space radiation with different shielding: the FLUKA code coupled with anthropomorphic phantoms*. IOP Journal of Physics: Conference Series **41** (2006) 135
  - F. Ballarini, G. Battistoni, M. Campanella, M. Carboni, F. Cerutti, A. Empl, A. Fassò, A. Ferrari, E. Gadioli, M. V. Garzelli, M. Lantz, M. Liotta, A. Mairani, A. Mostacci, S. Muraro, A. Ottolenghi, M. Pelliccioni, L. S. Pinsky, J. Ranft, S. Roesler, P. R. Sala, D. Scannicchio, S. Trovati, R. Villari, T. Wilson, N. Zapp, V. Vlachoudis, *The FLUKA code: an overview*. IOP Journal of Physics: Conference Series **41** (2006) 151
  - F. Ballarini, G. Battistoni, F. Cerutti, A. Ferrari, E. Gadioli, M. V. Garzelli, A. Mairani, A. Ottolenghi, L. S. Pinsky, P. R. Sala, S. Trovati, *Physics to understand biology: Monte Carlo approaches to investigate space radiation doses and their effects on DNA and chromosomes*. Proceedings of the 11th International Conference on Nuclear Reaction Mechanisms, Varenna, June 12-16, 2006, E. Gadioli ed., Ricerca Scientifica ed Educazione Permanente, Suppl. **126** (2006) 591
  - S. V. Förtsch, E. Gadioli, E. Z. Buthelezi, F. Cerutti, S. H. Connell, A. A. Cowley, M. J. Dlamini, H. Fujita, A. Mairani, R. Neveling, F. D. Smit, *Production of intermediate mass fragments in the interaction of  $^{12}\text{C}$  with  $^{12}\text{C}$  at incident energies of 200 MeV and 400 MeV*. Proceedings of the 11th International Conference on Nuclear Reaction Mechanisms, Varenna, June 12-16, 2006, E. Gadioli ed., Ricerca Scientifica ed Educazione Permanente, Suppl. **126** (2006) 251
  - F. Cerutti, G. Battistoni, G. Capezzali, P. Colleoni, A. Ferrari, E. Gadioli, A. Mairani, A. Pepe, *Low energy nucleus-nucleus reactions: the BME approach and its interface with FLUKA*. Proceedings of the 11th International Conference on Nuclear Reaction Mechanisms, Varenna, June 12-16, 2006, E. Gadioli ed., Ricerca Scientifica ed Educazione Permanente, Suppl. **126** (2006) 507

- F. Ballarini, G. Battistoni, F. Cerutti, A. Fassò, A. Ferrari, E. Gadioli, M. V. Garzelli, A. Mairani, A. Ottolenghi, H. G. Paretzke, V. Parini, M. Pelliccioni, L. S. Pinsky, P. R. Sala, D. Scannicchio, S. Trovati, M. Zankl, *GCR and SPE organ doses in deep space with different shielding: Monte Carlo simulations based on the FLUKA, code coupled to anthropomorphic phantoms*. Adv. Space Res. **37** (2006) 1791
- F. Ballarini, D. Alloni, A. Facoetti, A. Mairani, R. Nano, A. Ottolenghi, *Modelling radiation-induced bystander effect and cellular communication*. Radiat. Prot. Dosim. **122** (2006) 244
- S. Trovati, F. Ballarini, G. Battistoni, F. Cerutti, A. Fassò, A. Ferrari, E. Gadioli, M. V. Garzelli, A. Mairani, A. Ottolenghi, H. G. Paretzke, V. Parini, M. Pelliccioni, L. S. Pinsky, P. R. Sala, D. Scannicchio, M. Zankl, *Human exposure to space radiation: Role of primary and secondary particles*. Radiat. Prot. Dosim. **122** (2006) 362
- F. Ballarini, D. Alloni, A. Facoetti, A. Mairani, R. Nano, A. Ottolenghi, *Radiation risk estimation: modelling approaches for targeted and non-targeted effects*. Adv. Space Res. **40** (2007) 1392
- S. V. Försch, F. Cerutti, P. Colleoni, E. Gadioli, E. Gadioli Erba, A. Mairani, G. F. Steyn, J. J. Lawrie, F. D. Smit, S. H. Connell, R. W. Fearick, T. Thovhogi, *Contributions of complete fusion and break-up-fusion to intermediate mass fragment production in the low energy interaction of  $^{12}\text{C}$  and  $^{27}\text{Al}$* , Nucl. Phys. **A** (2007), doi:10.1016/j.nuclphysa.2007.09.007
- F. Cerutti, W. Enghardt, A. Ferrari, E. Gadioli, A. Mairani, K. Parodi, F. Sommerer, *Heavy Ion Interaction Modeling for Hadrontherapy Applications*, Proc. VII Latin American Symposium on Nuclear Physics and Applications, Cusco, Peru, June 11-16, 2007, in press
- F. Cerutti, A. Ferrari, E. Gadioli, A. Mairani, S. V. Försch, J. Dlamini, E. Z. Buthelezi, H. Fujita, R. Neveling, F. D. Smit, A. A. Cowley, S. H. Connell, *Complete Fusion and Break-up Fusion Reactions in Light Ion Interactions at Low Energies*, Proc. VII Latin American Symposium on Nuclear Physics and Applications, Cusco, Peru, June 11-16, 2007, in press



# Acknowledgments

My first acknowledgment is addressed to Prof. Ettore Gadioli who has been an enthusiastic scientific guide since I was undergraduate student at the University of Milan. The second acknowledgment is addressed to Prof. Andrea Ottolenghi for the marvelous first two years of my Ph.D.

A special thank is due to Francesco who has significantly contributed to my scientific growth. Another special thank is due to Katia who I have met just an year and half ago and she has been fundamental to achieve this thesis. She has provided me with confidential material and an incredible encouragement. I thank all the members of the FLUKA collaboration, especially Alfredo, Giuseppe and Paola for their help into understanding FLUKA and for very useful discussions. I thank Stephan and Florian for the interesting research performed together and for the confidential material that they gave me.

Another special thank is addressed to Michael Scholz and his group for the fantastic periods spent at GSI and for having introduced me in the radiobiological research. Another special thank is addressed to the IThemba group and especially to Siegie for having provided me with nice experimental data. A special thank is due to Prof. L. S. Pinsky of the University of Houston and his group for the spectacular period spent at Houston as an International Ph.D. student.

I thank Elio, Francesca, Luca for their help and for the nice time spent together. A special thank is addressed to all the friends who have met at Pavia and especially to Stefania, Silva and Lorenzo.

An affectionate thank is addressed to Enrica because she has come into my life as ray of sunshine into a cloudy day.

Infine voglio ringraziare i miei genitori per il continuo supporto e incoraggiamento, grazie soprattutto a loro sono riuscito a raggiungere questo traguardo.